

**DRIVEN STOKESIAN SUSPENSIONS:
PARTICLE ANISOTROPY, EFFECTIVE INERTIA AND
TRANSIENT GROWTH**

A THESIS

SUBMITTED TO THE
TATA INSTITUTE OF OF FUNDAMENTAL RESEARCH, MUMBAI
FOR THE DEGREE OF

DOCTOR OF PHILOSOPHY
IN PHYSICS

BY

RAHUL CHAJWA

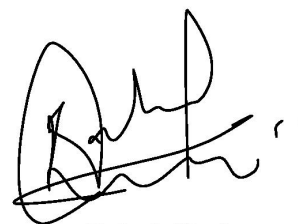
INTERNATIONAL CENTRE FOR THEORETICAL SCIENCES
TATA INSTITUTE OF FUNDAMENTAL RESEARCH
BENGALURU, KARNATAKA
NOVEMBER 2020

©2020– Rahul Chajwa
All rights reserved

Declaration

This thesis is a presentation of my original research work. Wherever contributions of others are involved, every effort is made to indicate this clearly, with due reference to the literature, and acknowledgement of collaborative research and discussions.

The work was done under the guidance of Prof. Rama Govindarajan, Prof. Sriram Ramaswamy and Prof. Narayanan Menon, at International Centre for Theoretical Sciences TIFR, Bengaluru.



Rahul Chajwa

In my capacity as supervisor of the candidate's thesis, I certify that the above statements are true to the best of my knowledge.



Prof. Rama Govindarajan



Prof. Sriram Ramaswamy



Prof. Narayanan Menon

Date: 04/11/2020

To My Dear Nephew

Sheenu

Acknowledgements

I thank ICTS TIFR Bengaluru, TIFR Hyderabad, and UMass Amherst for making every aspect of my Ph.D. tenure smooth. I thank Ganga Prasath, Lee Walsh, Deepak Kumar, and Sumit Birwa for generously offering their help and for being such wonderful lab mates. I thank Jooyoung Chang for teaching me useful techniques on thin films and UV lithography during my visit to UMass. I thank Rayees for the assistance he offered to the lab. I thank Ananyo Maitra, Surajit Dhara, and Anand Yethiraj for the fruitful discussions at TIFR H, and to Jason Picardo, Sunil Bharadwaj, Sebastian Bürger, Divya Jaganathan, and Lokrshi Dadhichi for the same at ICTS and IISc. Tutoring a course with Mustansir Barma was a delightful experience and I thank him for the thrilling discussions. I thank Anusha Gopalan for always being there to bounce ideas with. During my Ph.D., I have had the opportunity to be friends with some amazing students at ICTS, TIFR H, UMass Amherst, and IISc Bengaluru, whom I thank very much for the wide ranging conversations. Here, it is impossible to acknowledge every person who has helped me grow academically and personally during my Ph.D., but I'm sure all those whom I want to thank, already know.

My visit to UMass Amherst was supported by Narayanan Menon's NSF DMR-1507650 grant and Sriram Ramaswamy's J.C. Bose Fellowship of the SERB (India). I acknowledge support from the Infosys ICTS excellence travel grant and ICTS contingency grant. And, I acknowledge the summer research fellowship of the Indian Academy of Sciences Bengaluru for providing me the life-changing opportunity to work with Sriram Ramaswamy during my undergrad.

I want to extend my sincere gratitude to my Ph.D. advisors – Rama Govindarajan, Narayanan Menon, and Sriram Ramaswamy, for introducing me to some stimulating research directions in soft matter physics and fluid dynamics, for offering me their consistent guidance, and most importantly for teaching me how to do research; all of these made my Ph.D. a pleasurable experience. Needless to say, they have played a major role in arriving at the results presented in this thesis.

I owe so much to my mom and dad, for their utter passion for my education, for teaching me the value of hard work, and for being a constant source of encouragement. I sincerely hope that all their efforts in me are being paid off.

Contents

Dedication	i
Acknowledgements	ii
Contents	iii
Publications based on this thesis	vi
1 Introduction	1
1.1 Background	2
1.1.1 Crowley instability and the LR Model	7
1.1.2 Transient growth: a non-normal route to instability	10
1.1.3 Caustics of inertial particles in vortical flows	12
1.2 Organisation of the thesis and our main results	14
2 Settling Disk Pairs: Planetary and Non-Planetary Orbits	18
2.1 Introduction	18
2.2 Experiments	19
2.3 Far-field analysis	21
2.3.1 Planetary orbits	23
2.3.2 Beyond planetary orbits	27
2.3.3 Rocking dynamics	28
2.4 Scaling analysis and Kepler’s third law	30
2.5 A peculiar Hamiltonian for multiple disks	32
2.6 Conclusion	33
3 Experiments on Sedimenting Disk Arrays: Two Dynamical Regimes	34
3.1 Introduction	34
3.1.1 Overview of the setup	36

3.2	Release mechanism	38
3.3	Initial perturbations	42
3.4	Measurements	43
3.4.1	Image processing and analysis	44
3.5	Two regimes of dynamics	47
3.5.1	Waves of orientation coupled with number density fluctuations	48
3.5.2	Clumping instability decorated with orientations	48
3.6	Conclusion	48
4	Theory of Sedimenting Spheroid Lattices: Waves & Algebraic Growth	52
4.1	Introduction	52
4.2	Broken-symmetry hydrodynamics	53
4.3	“Microscopic” ingredients : pair hydrodynamic interactions	56
4.4	A hidden Hamiltonian sector: monoatomic chain of masses-and-springs	57
4.5	Wavelike modes and clumping instability	59
4.5.1	Far-field simulations with periodic boundaries	63
4.6	Non-normality and the transient algebraic growth of wavelike modes	64
4.6.1	Wave solution for spheroids	64
4.6.2	Algebraic growth of vibrational “energy”	67
4.7	Conclusions	69
5	Summary and Future Directions	71
6	Appendix	74
6.1	Details of the supplementary movies	74
6.1.1	Movies for Chapter 2: Duet of the Disks	74
6.1.2	Movies for Chapter 3 & 4: Group Dance	75
6.1.3	Movies for Chapter 5: Swimmers in a Swirl	76
6.2	Error in ellipse fitting	78
6.3	Perpendicular and rocking pair dynamics	78
6.4	Dissimilar disks	80
6.5	Stable orientations around a force monopole	82
6.6	Noiseless AOUP and ABP in a point vortex	84

Publications based on this thesis

1. **Kepler Orbits in Pairs of Disks Settling in a Viscous Fluid**
Rahul Chajwa, Narayanan Menon, Sriram Ramaswamy
Physical Review Letters **122**, 224501 (2019). [arXiv link](#)
2. **Waves Algebraic Growth and Clumping in Sedimenting Disk Arrays**
Rahul Chajwa, Narayanan Menon, Sriram Ramaswamy, Rama Govindarajan
Physical Review X **10**, 041016 (2020). [Open Access](#)
3. **Effective Inertia and Caustics of Active Particles in Vortical flows**
Rahul Chajwa, Sriram Ramaswamy, Rama Govindarajan. (to be submitted)

Under preparation

1. **Stokeslet Objects as a Minimal Model for Marine Snow Aggregates**
Sebastian Bürger, Rahul Chajwa, S. Ganga Prasath, Rama Govindarajan

Chapter 1

Introduction

We all have some practical experience with how flows influence the dynamics of solid objects moving through fluid, from throwing a Frisbee or a paper plane, or from just observing the elegant trajectories of a falling leaf or a card [1, 2]. Our intuition for these phenomena is based on the inertia of the objects and the fluids. However, at microscopic scales, completely different hydrodynamics steers our world, in which inertia is negligible, and viscous forces dominate [4]. For characteristic flow velocity \bar{U} , length scales L , viscosity μ , and density ρ of the fluid, the ratio of inertial to viscous forces is given by the Reynolds number $Re = \rho\bar{U}L/\mu$. An inertialess regime, i.e. $Re \ll 1$ naturally emerges when length scales are microscopic, for typical values of ρ , ν , and \bar{U} . For microscopically small particles of size a moving with velocity v , the thermal Brownian motion is usually important as the Péclet number, $Pe = av/D$ can be smaller than 1, with thermal diffusivity D . In this thesis, we are interested in the dynamics of particles in the regime of $Re \ll 1$ and $Pe \gg 1$, where thermal effects are negligible, and interplay between viscous hydrodynamics and driving forces governs the dynamical behavior [5]. Such non-Brownian Stokesian dynamics is ubiquitous in nature and industry [6], in situations where particles are large enough to render thermal effects unimportant but small enough to be considered non-inertial. In table-top experiments the physics of this regime can be achieved with larger particles like coins in a highly viscous fluid like honey. At $Re \rightarrow 0$, particles obey the constraint of time-reversibility, in that the equations of motion are invariant under changing the sign of driving forces and velocities, which plays a crucial role in the mobility of micro-organisms [7, 8], and also results in some

confounding phenomena like the demixing of ink in a fluid [9], and memory formation in sheared suspensions [10].

The present thesis considers two scenarios – 1) externally driven or sedimenting particles with hydrodynamic interactions and 2) internally driven or active self-propelled particles in an imposed flow. For both these cases, we show how particle shape anisotropy transfigures the collective dynamics, and leads to the emergence of an effective inertia in which the anisotropy axis of the particles behaves like a canonical momentum. We discover some curious analogies with well known inertial systems and open a window into an unusual growth mechanism, namely transient algebraic growth, which is likely consequential in many other non-equilibrium soft matter systems. In the first section 1.1, we give a bird’s-eye view of the literature and present the basic concepts which form the groundwork for this thesis. In the second section 1.2 we lay down the organisation of the thesis and highlight our main findings.

1.1 Background

In the classical world around us gravity is inescapable, and as a consequence collective settling of microscopic particles in an ambient fluid is a ubiquitous phenomenon. For slow viscous flows with velocity \mathbf{U} and pressure p , the steady Stokes equation, $\mu\nabla^2\mathbf{U} = \nabla p$ along with incompressibility $\nabla \cdot \mathbf{U} = 0$, and suitable boundary conditions, governs the dynamics of moving bodies [6, 11]. The linearity of the Stokes equation offers numerical solutions via superposition for a wide range of problems [12, 13]. A force monopole at the origin in an unbounded fluid, called a stokeslet, leads to the viscous hydrodynamic kernel

$$\mathcal{G}_{ij}(x) = \frac{1}{8\pi r} \left(\delta_{ij} + \frac{r_i r_j}{r^2} \right), \quad (1.1)$$

which decays with distance r and $1/r$ [12], similar to that encountered in Newtonian gravity and electrostatics. Thus, a point particle settling at the origin disturbs the fluid out to large distances in all directions, and as a consequence, collective Stokesian sedimentation offers a classical many-body problem with long-ranged hydrodynamic interactions.

For calculating hydrodynamic interactions between settling spheres, the method of reflections is employed to write an approximate solution iteratively as a power series in a/r

[14], where a is the radius of the sphere and \mathbf{r} is the separation vector. In practice, truncating this series with just the first few terms in it, captures hydrodynamic interactions with reasonable accuracy, given that the particles are widely separated [6, 12]. Employing this technique on two spheres settling in arbitrary configuration [6], with \mathbf{r} making an angle ϕ with gravity, gives the vertical velocity $U_{\parallel} = U_0[1 + 3a(1 + \cos^2 \phi)/4r]$, which is greater than the velocity of an isolated settling sphere $U_0 = F/6\pi\mu a$. And, for $\phi \neq 0, \pi/2$, there is a drift perpendicular to gravity, given by $U_{\perp} = 3aU_0 \sin(2\phi)/8r$. These results are consistent with the exact solution of the Stokes equation in bipolar coordinates [15]. There are very limited scenarios in which a Stokesian boundary value problem can be solved analytically, and [15] is the only analytical solution available that we know of for a multi-particle case [6]. The Stokesian time-reversal symmetry [7] prohibits any change in the magnitude and direction of \mathbf{r} , i.e. any configuration of a pair is stationary. This stability is immediately disrupted when a third sphere is introduced [16, 17]. Summing the flow fields of three point forces leads to chaotic dynamics [16], such that at long times a pair leaves the third particle behind. The time of transition into this state, and which two of the three particles form a pair, are both sensitive to the initial condition.

In the system of multiple settling spheres, each sphere sinks in the backdrop of flow created by others [18]. Thus, the flow depends on the precise arrangement of particles (microstructure) and the microstructure evolves due to the flow [11]. This two-way coupling leads to many challenges in the statistical mechanics of Stokesian sedimentation [5, 20, 21], where a simple pair-wise superposition of velocity due to the stokeslet predicts a divergence of both the mean velocity [22] and the fluctuations about this mean [23], as the domain size becomes infinite. However, such system size dependence is not observed in experiments [43, 25]. These central issues have made sedimentation a venue of active research in non-equilibrium statistical mechanics [5, 26, 27].

Particles in most natural and industrial settings are non-spherical, thus the age-old issues in sedimentation need to be considered anew in light of the internal degrees of freedom coming from particle shape [28, 29]. Spheroids offer a simple route to introducing particle shape anisotropy. An isolated settling needle (limit of prolate spheroids), behaves qualitatively like a pair of spheres, thanks to the fore-aft symmetry. The pair falls twice as fast with its long

dimension along the gravity direction, as compared to when it is perpendicular to gravity; demonstrated in beautiful experiments by G.I. Taylor [30]. This can be understood using the slender body theory [31], which is a special case of the singularity solution for spheroids [32]. Spheroidal harmonics offer an analytical solution for a single settling spheroid in an unbounded fluid, but only in specific configurations [6].

As soon as another spheroid is introduced in the flow field of the first, the pair immediately falls into a graceful dance [see Supplementary Video 2.1], due to coupling between the rotational and translational degrees of freedom. Approximate analytical expressions for drag and torques on a pair of settling spheroids in an arbitrary configuration was given by S. Wakiya (1965) [33]. The periodic dance of the settling pair, however, was first noted in prolate spheroids by S. Kim (1985) in a numerical solution using the method of reflections [34], and was observed in experiments by Jung et al. (2006) for disks and rods in specific initial configurations [35], and their numerical simulation using the boundary integral method confirmed the robustness of periodic dynamics in this system. To capture the essential physics of coupling between translations and rotations of a settling pair of shaped objects, Goldfriend et al. (2015) [36] introduced stokeslet objects as a minimal model to calculate pair-mobility to leading order in a/r . In this framework, the pair dynamics of self-aligning spheroids are presented [37], which is distinct from the dynamics of homogeneous axisymmetric objects with fore-aft symmetry (apolar spheroids) relevant to the present thesis. For three apolar spheroids, manifestation of Jánosi’s chaos [16] is expected [see Supplementary Video 1.1]. However, this remains unexplored.

The collective settling of apolar spheroids is more rich and complicated than that of spheres [38, 39, 40, 28], as a tilted oriented particle can drift laterally while settling [30, 32], and its orientation is a dynamical variable that evolves in response to the flow created at its location by other particles [41]. A homogeneous suspension of spheroids has been shown to be linearly unstable to perturbations in number density [39, 40]; wherein the symmetric part of the local velocity gradient aligns the spheroids on average, such that the resultant lateral drift due to orientation enhances the density perturbation, making it unstable [39]. In this argument, the effect of the antisymmetric part of the velocity gradient is, however, much less transparent, as discussed in Appendix 7.3 of this thesis. Stokesian sedimentation

of an initially randomly distributed suspension of fibers has been studied experimentally [28, 42, 43, 44] and numerically [45, 46, 47] in great detail, with a focus on the dependence of velocity fluctuation and structure factor on system size and particle concentration. Both numerical and experimental investigations show large scale inhomogeneities, with patches of dense regions in which mean orientation aligns with gravity. Within these dense regions called streamers [44] there are fast settling clusters of fibers [47]. These clusters spontaneously form and break [28]. The dynamics of such a cloud of fibers are separately studied in experiments and simulations [48], with an observation of torus formation similar to that of swarms of settling spheres [49]. The formation of clusters and streamers from homogeneous suspension occurs in a highly non-linear regime – how this non-linear state is arrived at from linear instability of Koch & Shaqfeh [39] and what sets the typical size of clusters [50] is still unresolved [28]. In particular, an experiment on the linear stability analysis of a spheroid suspension with control on the initial state is missing. Moreover, disk-like particles have not captured much attention [34, 28], despite their frequent occurrence in nature in the form of ice-crystals in the early stages of cloud formation, diatoms in the pelagic algal blooms, clay particles in riverbeds, and red blood cells in plasma.

Although detailed investigations of multiple settling spheroids have been done in the past three decades, the richness of the two-spheroid dynamics presented in this thesis was unexplored [61]. At a multi-particle level, we do not address the unresolved issues in the homogeneous suspension of fibers. We instead present surprises in Stokesian settling of anisotropic objects by turning to a different state of sedimenting matter acquired by initializing particles in lattice configurations. We ask how particle shape anisotropy modifies the inescapable instability of a settling sphere array studied almost fifty years ago by J.M. Crowley (1971) [51, 52]. A coarse-grained description of drifting lattices of isotropic objects has previously emerged in the dynamics of moving crystals [53] and flux lattices in type-II superconductors [55], which has further led to new theoretical directions in non-equilibrium statistical mechanics [54]. Understanding the dynamics of sedimenting arrays of orientable objects helps us connect particle level interactions to long-wavelength collective modes [62].

In our study of spheroid pairs and lattices, we find the emergence of inertia as a result of particle anisotropy and driving [61, 62]. Since a self-propelled particle also has both these

ingredients, with anisotropy set by the direction of self-induced velocity and driving coming from activity, by naïve extrapolation one may expect an effective inertia in its dynamics. When passive inertial particles are suspended in vortical or turbulent flows, they form large scale inhomogeneous structures [99, 102], and are known to display caustics and clustering [101, 103], unseen in inertia-less particles. These may be thought of as the fingerprints of particle inertia [126]. The concept of caustics has its origin in geometrical optics, where they are the envelope of light rays marked by bright filamentous structures [122], and are formally studied in the framework of catastrophe theory [119]. Their manifestation can be easily seen in the bottom of a swimming pool on a sunny day [120] or in the twinkling of stars in a clear night sky [121]. In the present thesis, in the context of Stokesian suspensions, we ask whether caustics can arise in the dynamics of Stokesian active particles in vortical flows, as a result of the effective inertia arising from their persistent self-propelled motion. We define caustics here as regions where two particles may arrive at the same location and the same time but with different velocities. In such regions there is no way to approximate the particle velocities in terms of a field description.

The dynamics of motile particles in imposed flows is a research area with an established history [106], but enormous current interest in this field is sparked by its relevance to phytoplankton in the ocean and thence to global climate change [98, 107, 108]. Formation of inhomogeneous structures and clustering is observed for active particles in vortical flows [109, 111, 112, 113], and turbulence [104, 110]. Effective Hamiltonian dynamics in microswimmers has been reported in wall-bounded flows [67, 68] and in a Lamb-Oseen vortex [114]. However, these observations are not made in light of the effective inertial dynamics, and the ‘active caustics’ remain hitherto unreported to the best of our knowledge. Thus a study of effective inertia and caustics in active suspensions appears worthwhile. In this thesis, we study the similarities and distinctions between active inertialess particles and passive inertial particles in vortical flows and look at the regimes of caustics formation, akin to the passive inertial case [101, 102].

Last year marked the 200th anniversary of George Gabriel Stokes [‘Stoked about Stokes’, *Nat. Rev. Phys.* **1**, 637 (2019)]. Stokesian suspensions continue to astonish us with their richness and complexity and remain a fertile domain of research. In the sections making up

the rest of this chapter, we set the stage for the surprises in driven Stokesian suspensions presented in this thesis. First, we discuss how pair hydrodynamic interactions between sedimenting spheres lead to Crowley’s clumping instability [51], and how symmetries can be used to construct long-wavelength dynamics of drifting lattices in the Lahiri-Ramaswamy (LR) model [53, 54]. Second, we introduce an unusual growth mechanism that takes place when the dynamical matrices are non-normal [81]. Third, we present the formation of caustics in inertial particles [101]. We supplement these sections with a couple of movies, with links provided in the Appendix 6.1.

1.1.1 Crowley instability and the LR Model

An isolated sphere of radius a and buoyant weight F in an unbounded fluid of viscosity μ settles with a speed $U_0 = F/6\pi\mu a$ [3]. Two such identical spheres separated by a distance r , with the separation vector \mathbf{r} making an angle ϕ with respect to the vertical, settle differently from a single one, as a result of their hydrodynamic interaction. This behavior can be decomposed into two parts [see Fig.1.1 (a) & (b)], using the method of reflections [6] – (i) A pair falls faster than an isolated settling sphere due to reduced drag, with the component of velocity along gravity given by

$$U_{\parallel} = U_0 \left[1 + \frac{3a}{4r}(1 + \cos^2 \phi) \right], \quad (1.2)$$

and (ii) component perpendicular to it given by

$$U_{\perp} = U_0 \frac{3a}{8r} \sin(2\phi). \quad (1.3)$$

The dynamics of a linear horizontal array of spheres as shown in Fig. 1.1 (c) with only hydrodynamic interactions due to gravitational settling, can be constructed using the above two ingredients. Consider positional perturbations \mathbf{u} about a reference lattice with spacing d . At any given lattice point, say n , the perturbation has both horizontal u_x^n and vertical u_z^n components. As the lattice freely settles along the $-z$ direction, the n^{th} sphere interacts hydrodynamically with the $(n+l)^{\text{th}}$ and $(n-l)^{\text{th}}$ sphere, where $l = 1, 2, \dots, \infty$, and the lattice extends to infinity. In the mean settling frame, the linearized equation of motion for a small perturbation of the n^{th} sphere about the reference lattice becomes [51]

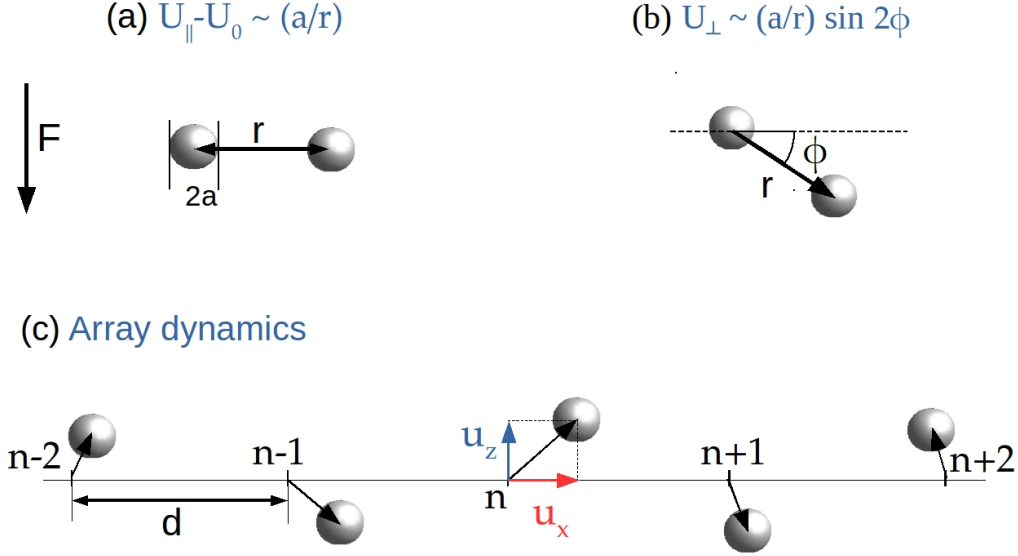


Figure 1.1: **Crowley instability**

$$\frac{du_x^n}{dt} = -\frac{3aU_0}{4d^2} \sum_{l=1}^{\infty} \frac{u_z^{n+l} - u_z^{n-l}}{l^2}, \quad (1.4)$$

$$\frac{du_z^n}{dt} = +\frac{3aU_0}{4d^2} \sum_{l=1}^{\infty} \frac{u_x^{n+l} - u_x^{n-l}}{l^2}. \quad (1.5)$$

In the nearest neighbour approximation in which the n^{th} sphere interacts only with the $(n+1)^{\text{th}}$ and $(n-1)^{\text{th}}$ spheres, the dispersion relation becomes, $\omega_{\pm} = \pm i3aU_0 |\sin(qd)|/2d^2$, where the perturbation wavenumber q lies in the domain $0 \leq q \leq \pi/d$. Thus the frequencies are imaginary at all wavenumbers, and of opposite sign, giving rise to an inescapable instability, which at long times gives rise to the formation of clumps of spheres [Supplementary Video 2.1 demonstrates the basic mechanism]. Surprisingly, despite the long-range nature of hydrodynamic interactions, the nearest-neighbour approximation compares well even with Crowley's [51] experiments on the linear stability of spheres which are carried out in a cubical geometry with walls distant from the particles in all directions. If there is a compression of the lattice at a given location, the local settling speed is increased due to reduced drag, generating a local tilt in the lattice. The direction of the lateral drift due to tilt is such that it further compresses the lattice. In the configuration shown in Fig 1.1 (b) the pair drifts

towards the right. However, the symmetry of the system does not distinguish right from left and therefore from general symmetry arguments, there could be a system in which the tilted pair drifts to the left preventing the clumping instability. Indeed, a drifting flux lattice in a type-II superconductor offers precisely such a pair interaction, leading to kinematic waves [55].

These symmetry arguments in drifting lattices were presented in the LR model [53, 54]. Consider the perturbation shown in Fig. 1.1 (c) in the long wavelength limit, where it can be approximated as a continuous displacement field $\mathbf{u}(x, t)$. The dynamics of the lattice in the comoving frame can be written as, $\dot{\mathbf{u}} = \mathbb{M} \cdot \mathbf{F}$, where \mathbb{M} is the mobility of the lattice, which is a geometrical property independent of the forcing. This particular form of the equation of motion guarantees that the Stokesian time-reversal symmetry is obeyed. The central theme of Lahiri & Ramaswamy (1997) [53] was to construct the most general form of \mathbb{M} using symmetries of the system. First, the translational invariance of the ambient fluid ensures that $\mathbb{M}(\nabla\mathbf{u})$ can only be a function of gradients of the displacement field. Doing the gradient expansion of $\mathbb{M}(\nabla\mathbf{u})$ while retaining only the leading terms in the gradients of the displacement field, gives the continuum equations of motion

$$u_x = \lambda_1 \frac{\partial u_z}{\partial x} + \lambda_2 \frac{\partial u_x}{\partial x}, \quad u_z = \lambda_3 \frac{\partial u_x}{\partial x} + \lambda_4 \frac{\partial u_z}{\partial x}. \quad (1.6)$$

Since gravity sets the only anisotropy direction in the system, the equation of motion must be invariant under $x \rightarrow -x$ and $u_x \rightarrow -u_x$. And thus the terms with λ_2 and λ_4 are not allowed in the above equations, in order to satisfy the specific rotational invariance; giving rise to the equations, $u_x = \lambda_1 \partial u_z / \partial x$ and $u_z = \lambda_3 \partial u_x / \partial x$. These equations say that the local tilt of the lattice $\partial u_z / \partial x$ gives a horizontal drift and the local compression of the lattice $\partial u_x / \partial x$ changes the settling speed. The resulting dispersion relation is $\omega_{\pm} = \pm q \sqrt{\lambda_1 \lambda_3}$. The long wavelength limit $qd \ll 1$ of the Crowley instability comes out as a special case of the LR model, when $\lambda_1 = -\lambda_3 = 3aU_0/2d$. Kinematics waves occur when λ_1 and λ_3 have the same sign [55].

Note that this symmetry-based phenomenological model is for a one-dimensional array in a three-dimensional fluid, but with only local interparticle interactions. Quasi-two-dimensionality is important for the phenomenology in order to assume only local interactions

in form of gradient terms. The term “quasi-2D” refers to a system which is limited to a narrow thickness in one direction by the presence of bounding walls, while being effectively unbounded in the other two, where the walls are a momentum sink. The length of the confinement introduces a cutoff length scale beyond which hydrodynamic interactions decays with inter-particle distance r as $1/r^2$ [56, 57], which is weaker as compared to $1/r$ in an unbounded fluid [12]. Later in this thesis, we will make use of this simplification in our experiments and theory on settling disks.

There are two main takeaways from this analysis – hydrodynamic interactions can be used to construct many-particle dynamics [51, 52], and long-wavelength dynamics can be constructed without knowing the microscopic details of interactions, using general symmetry arguments. However, determining the phenomenological parameters requires solving the fluid dynamics of two-body interactions [53, 55].

1.1.2 Transient growth: a non-normal route to instability

In hydrodynamic stability problems [74], usually, a nonlinear system of equations is linearized and the growth or decay of infinitesimal perturbations about a given steady-state is studied. A standard eigenvalue analysis of linearized dynamics explains the experimental results of certain systems successfully like Taylor-Couette flow and Rayleigh-Benard convection, while it completely fails to explain the instability observed in the experiments of others, like plane Poiseuille, pipe and plane Couette flows [75, 76]. These classical problems date back to the nineteenth century, and it became clear only in the 1980s [77] (although problems with a simple-minded eigenvalue analysis were known since 1960 [78], see also [79]) that the least stable or most unstable eigenvalue in these systems does not dictate the short-time behavior and that such analysis can be misleading when the stability operator is not self-adjoint. And it is now well accepted that in such systems a combination of non-normal modes can grow before decaying [81, 82, 84] and this transient growth can be large enough to perturb the system out of the linear regime, potentially leading to a sub-critical bifurcation behavior [84]. This section presents the basic idea using an example dynamical matrix [83, 81]. Consider the evolution of a state vector $\mathbf{X} \equiv (x_1, x_2)^T$ given by $\partial\mathbf{X}/\partial t = \mathbf{A} \cdot \mathbf{X}$, where the dynamical

matrix

$$\mathbf{A} = \begin{pmatrix} -0.1 & s \\ 0 & -0.2 \end{pmatrix}, \quad (1.7)$$

with a parameter s . The dynamical matrix \mathbf{A} is constructed such that when $s = 0$ we get a pair of orthogonal eigenvectors $(1, 0)^T$ and $(0, 1)^T$ with eigenvalues -0.1 and -0.2 respectively. Let us define the norm $\|\mathbf{X}\|$ as $\sqrt{x_1^2 + x_2^2}$ and ask how $\|\mathbf{X}(t)\|$ evolves in time, especially when $s \neq 0$. If we set $s = 4$, we get the eigenvectors $(1, 0)^T$ and $(-0.9997, 0.025)^T$ with the same eigenvalues as before. The crucial distinction is that when $s \neq 0$, \mathbf{A} is non-normal, i.e. the commutator $[\tilde{\mathbf{A}}(q), \tilde{\mathbf{A}}^\dagger(q)] \neq 0$, giving rise to non-orthonormal eigenvectors. The gain $G(T) \equiv \|\mathbf{X}(T)\| / \|\mathbf{X}(0)\| \leq \|\exp(\mathbf{A} * T)\|$ for any given time T depends on the initial state $\mathbf{X}(0)$. For an arbitrary initial state, say $\mathbf{X}(0) = (\cos \beta, \sin \beta)^T$ for $\beta = \pi/4, \pi/6, \pi/8$, the gain transiently grows as shown by blue curves in Fig.1.2, even when individual modes decay in time. However, for every T there is a special initial state $\mathbf{X}(0)$ that maximizes the gain called $G_{\max}(T)$ which can be found using singular value decomposition $[\mathbf{U}, \mathbf{\Sigma}, \mathbf{V}]$ of $\exp(\mathbf{A} * T)$ [84]. In particular, the first column of the right singular matrix \mathbf{V} gives this optimal initial state, whose evolution is shown by the red curve in Fig.1.2 for $T = 5$. If the nonlinearities in the system depend on $\|\mathbf{X}(t)\|$, as would often be the case, then high values of gain can push the system into the nonlinear regime, even when the initial $\|\mathbf{X}(0)\|$ is small [76]. This growth mechanism holds even with neutrally stable or wavelike modes instead of decaying ones [73], like the case discussed in chapter 14 of [80]. Although the mechanism is well established, a clean comparison of transient growth between experiments and theory is rare even in wall bounded shear flows, even though non-normality was established long ago.

Note that the question of whether the system is normal or non-normal is meaningful only when an appropriate norm is defined, which is preferably physically motivated and experimentally convenient to measure [75]. In fluid mechanical problems, the most common norm is the kinetic energy of the perturbations, but such an obvious energy norm is seldom available in other dissipative dynamical systems. As we will discuss later in the thesis, our choice of energy norm in an array of settling spheroids comes from a curious analogy with a lattice of masses and springs [62]. Lastly, it is important to note that non-normal dynamics

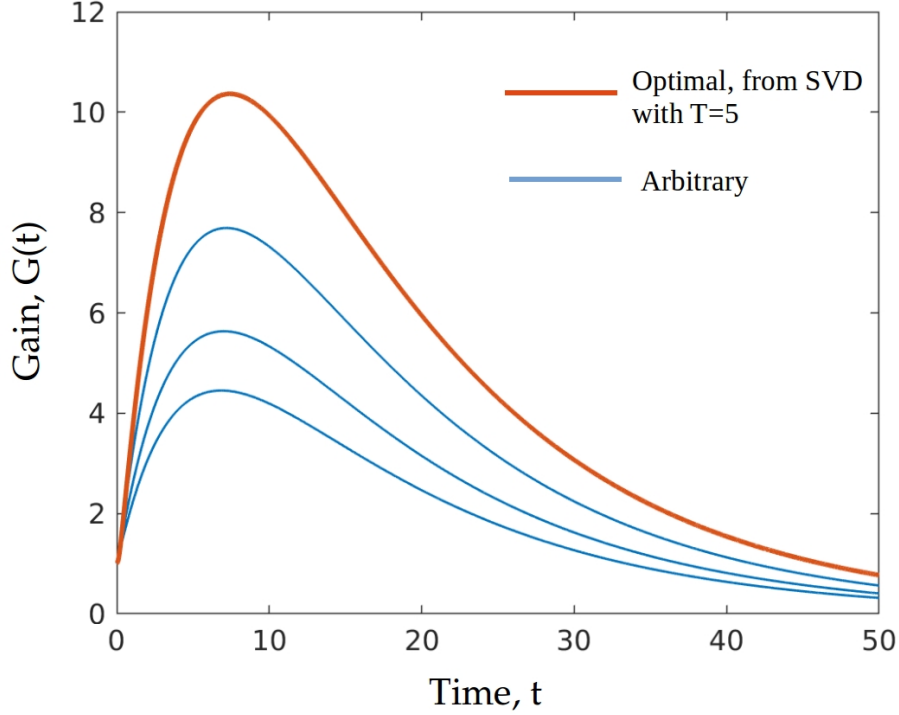


Figure 1.2: **Transient non-modal growth with stable eigenvalues.** Plot of the gain for arbitrary initial conditions $\mathbf{X}(0) = (\cos \beta, \sin \beta)^T$ with $\beta = \pi/8, \pi/6, \pi/4$ (blue curves), compared with the gain for optimal initial condition, i.e. first column of the right singular matrix, with $T=5$ (red curve).

go beyond hydrodynamic stability problems as presented in [80], and are likely to occur in a wide range of nonequilibrium systems. In chapter 4 of this thesis, we demonstrate their relevance to the sedimentation of ordered Stokesian suspensions of spheroids.

1.1.3 Caustics of inertial particles in vortical flows

The dynamics of an inertial particle with position \mathbf{X} and velocity \mathbf{v} in an imposed flow \mathbf{U} is given by the Maxey-Riley equations [100]: $\dot{\mathbf{X}} = \mathbf{v}$ and $\dot{\mathbf{v}} = (\mathbf{U} - \mathbf{v})/\tau$, where τ is the Stokes time which, being proportional to the mass of the particle, quantifies its inertia. Consider a flow field due to a point vortex, $\mathbf{U} = \Gamma \hat{\theta}/2\pi r \equiv \tilde{\Gamma} \hat{\theta}/r$. When lengths are non-dimensionalised by $\sqrt{\tilde{\Gamma}}\tau$ and time by τ the equations of motion in the cylindrical polar coordinates become

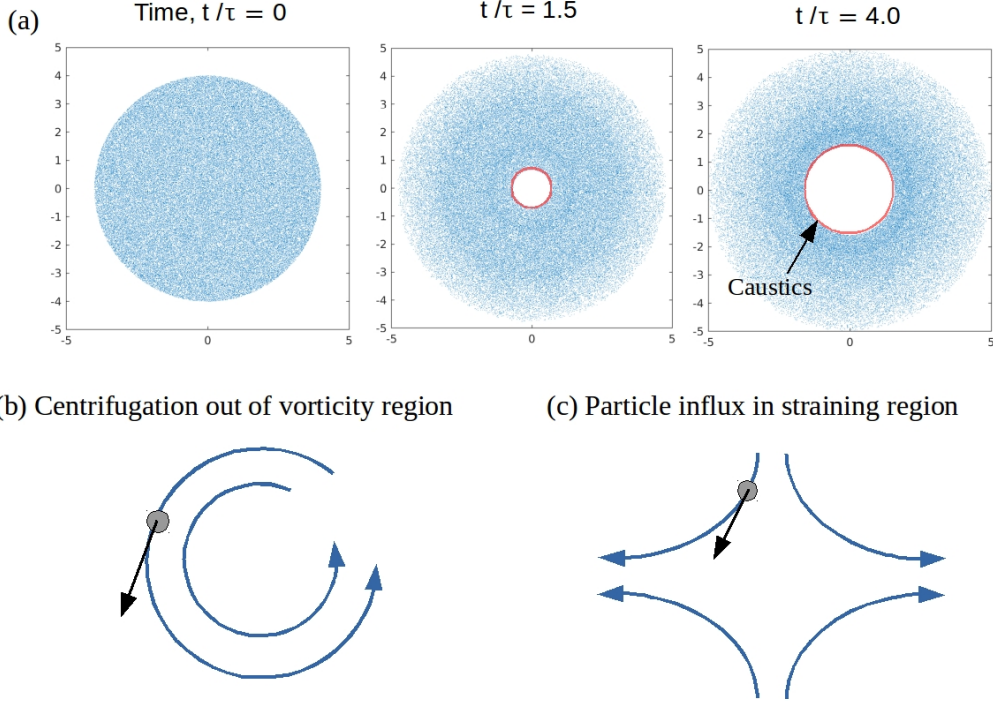


Figure 1.3: **Inertial particles in vortex flows.** (a) Snapshots of 10^5 inertial particles around a point vortex at various times [see Supplementary video 3.1]. The caustics ring (red) is the contour on which the number-density sharply spikes [101]. (b) & (c) schematically show the two mechanisms of preferential sampling in a generic flow.

[101]

$$\ddot{r} + \dot{r} = \frac{L^2}{r^3} \quad (1.8)$$

$$\dot{L} + L = 1 \quad (1.9)$$

where $L \equiv r^2 d\theta/dt$ is the angular momentum of the particle. The asymptotic solution for $r \gg 1$ is $\dot{r} = \text{constant}$ and $L = 1$. Therefore in this limit, if particles start out at different radii separated by Δr with the same initial velocity, the sign of Δr does not change as the particles evolve. The scenario is different and more interesting when $r \ll 1$, where the asymptotic equation for r becomes $\ddot{r} = L_0^2/r^3$, where L_0 is the initial angular momentum of the particle. Thus particles starting closer to the origin are accelerated out more strongly than the particles slightly further away, leading to crossing of trajectories, and caustics. This can be easily seen when we numerically simulate the dynamics of particles around a point

vortex following Maxey-Riley equations as shown in 1.3 (a). We discuss such dynamics for self-propelled particles in detail in this thesis.

In a generic flow it is known that inertial particles preferentially cluster in straining regions [99] by a combination of two mechanisms [96] as shown in Figure 1.3 (b) & (c). How similarly would inertialess active particles behave in vortical flows? Would they display caustics? Answering these questions is the central theme of chapter 5.

1.2 Organisation of the thesis and our main results

The three mechanisms discussed above in the sections 1.1.1, 1.1.2 and 1.1.3 forms the basis of chapter 3 & 4, chapter 4 and chapter 5 respectively.

In **Chapter 2** we investigate the graceful dance of a pair of settling coins, resulting from the viscous hydrodynamic interaction. The outcome of this investigation is published in *Phys. Rev. Lett.* **122**, 224501 (2019). We show experimentally that a pair of disks settling at negligible Reynolds number ($\sim 10^{-4}$) display two classes of bound periodic orbits, each with transitions to scattering states. We account for these dynamics at leading far-field order through an effective Hamiltonian in which gravitational driving endows orientation with the properties of momentum. This treatment is successfully compared to the measured properties of orbits and critical parameters of transitions between types of orbits. We demonstrate a precise correspondence with the Kepler problem of planetary motion for a wide range of initial conditions, find and account for a family of orbits with no Keplerian analog, and highlight the role of orientation as momentum in the many-disk problem. Our main results are:

- Addition of an orientational degree of freedom leads to rich dynamics even at the level of two-body hydrodynamic interactions.
- An asymptotic far-field theory explains the various dynamical behaviors.
- Our dynamical equations take an effective Hamiltonian form with translational and orientational degrees of freedom becoming conjugate variables and orientation behaving like momentum.

- A class of orbits maps precisely to Kepler orbits of planetary motion within this far-field description. All three laws of Kepler are seen in theory and experiments.
- We find a wide range of orbits with no Kepler analog.

Chapter 3 & **Chapter 4** share a common theme of how an array of anisotropic objects with fore-aft symmetry sediments in the Stokesian regime, and how particle shape anisotropy transmutes the Crowley’s clumping instability [51]. The outcome of this investigation is published in *Phys. Rev. X* **10**, 041016 (2020). In **Chapter 3**, we present experiments on an array of disks. The experiment is conceptually simple, but technically challenging due to the difficulty in accurately releasing multiple oriented objects in a highly viscous fluid. Thus our experiments are the first to carefully control the initial positions and orientations of an array of particles, and we highlight how we do it in this chapter. Note that, even for homogeneous suspensions, the experimental study of linear stability has been elusive due to the difficulty in creating an initial homogeneous steady state. In **Chapter 4**, we theoretically understand this system by both constructing the discrete dynamical framework, like that of Crowley’s but with spheroids, and writing down the broken symmetry hydrodynamics of displacement and orientation field of one-dimensional lattices of sedimenting spheroids. Our experimental and theoretical findings agree remarkably well with each other, without any fitting parameter. The key findings in our study of the spheroid lattice dynamics are:

- Two distinct dynamical regimes in the plane of wavenumber q and lattice spacing d : (1) wavelike excitations in orientations and number density fluctuations, and (2) Crowley-instability-like clumping decorated with orientations. Thus showing that anisotropic particle shape, ubiquitous in the natural world, leads to dynamics that competes with, and can eliminate, Crowley’s classic clumping instability.
- Our theory based on pairwise hydrodynamic interaction predicts a phase boundary with the form $\tilde{d} = \cos^2 q/2$, universal across all apolar oriented shapes, and in which the Crowley instability becomes a limiting case. Here, \tilde{d} denotes the lattice spacing scaled by an appropriate function of shape.
- Wavelike excitations map to the dynamics of a mass-and-spring lattice. The underlying

mechanism involves effective inertial dynamics with tilt as momentum as argued in our earlier work, and an emergent elasticity through the viscous hydrodynamic interaction.

- We show the unexpected emergence of a purely Hamiltonian sector of the dynamics, offering a natural inner product which forms our norm, or “energy” of disturbances, driving our subsequent analysis of transient growth through a non-normal dynamical matrix. The physics of transient growth is by no means dependent on a hidden Hamiltonian, but such an approach likely has a wider utility.
- We offer an experimental demonstration of transient algebraic growth of perturbations in a linearly stable regime, and close correspondence with our theory based on a non-normal dynamical matrix, showing that the mere absence of eigenvalues with a positive real part is no guarantee of long-term survival of the state. Such an experimental demonstration is rare, even in shear flows where this phenomenon is well known.

In **Chapter 5**, we investigate the deterministic dynamics of self-propelled particles in vortical flows, and study the consequences of effective inertia in this system, in particular, the emergence of ‘active caustics’. This work is *to be submitted* for publication. We study numerically two distinct models of active dimers in a single vortex, as well as in unsteady vortical flows; these dimers are noise-less manifestations of the so-called active Ornstein-Uhlenbeck particles (AOUPs) and active Brownian particles (ABPs). We loosely use the same nomenclature in this chapter, despite the absence of stochasticity. We consider a one-way coupling between the particle’s orientation \mathbf{w} and flow \mathbf{U} , in which \mathbf{w} responds to the local flow gradients. In the small r and large r limits, respectively, we present the inner and outer solutions of a singular perturbation analysis of the dimers in the point vortex, which compares qualitatively well with the numerical results. For studying the behavior in unsteady vortical flows, we simulate the flow in the vorticity stream-function formulation, in two dimensions using the pseudo-spectral method. Our main findings are

- The dynamical equations of both AOUP and ABP in an ambient flow display features of the Maxey-Riley equations, but with a strain-dependent relaxation term. The distinction from inertial dynamics lies in an additional $\mathbf{v} \cdot \nabla \mathbf{U}$ term that makes the

dynamics richer than that of passive inertial particles, where \mathbf{v} is the velocity of the particle, which is the sum of self-induced velocity $\beta\mathbf{w}$ and ambient flow velocity \mathbf{U} at the location of the particle.

- In a point vortex, caustics form in both AOUP and ABP, within a critical initial radial distance $r_0/\sqrt{\tilde{\Gamma}\tau}$ from the vortex origin. This distance depends on the orientation-flow coupling parameter α for AOUP and (α, β) for ABP; resulting in a phase boundary for caustics formation in the (r_0, α, β) space.
- ABP in unsteady vortical flows preferentially samples straining regions, which we quantify using the Okubo-Weiss parameter. For intermediate values of the non-dimensional motility $\beta' \equiv \beta/U$, clustering and caustics are more pronounced, similar to the dynamics of inertial particles as the Stokes number St is varied; suggesting that β' plays the same role as St .

In **Chapter 6** we conclude with some future directions.

Note that the contents of chapters 2, 3, 4 and 5 are supplemented with numerous videos, the links and details of which are provided in the **Appendix 6.1**. The videos are organized in three subsections containing – (1) periodic dynamics of pair of disks in experiments, (2) array dynamics of disks in experiments and numerics, and (3) dynamics of active dimers in vortical flows in numerical simulations.

Chapter 2

Settling Disk Pairs: Planetary and Non-Planetary Orbits

This chapter largely reproduces material presented in the text and supplement of [Phys. Rev. Lett. 122 224501 \(2019\)](#) “*Kepler Orbits in Pairs of Disks Settling in a Viscous Fluid*” by R Chajwa, N Menon and S Ramaswamy. (©2019 American Physical Society)

2.1 Introduction

Collective gravitational settling in a viscous fluid is a notoriously challenging problem in the physics of driven systems with long-range interactions. In the Stokesian limit of Reynolds number $Re \rightarrow 0$, sedimenting particles, which are monopoles of force density, manifest the hydrodynamic interaction [3, 6, 12, 4] in its strongest form [19, 5]. Among the consequences of this strong coupling are chaos in three-particle settling [16, 17], and the resulting statistical character of many-particle sedimentation [5, 28, 29, 27]. Interestingly, however, the collective settling of identical spheres can be built up from two-particle processes [15, 51, 53]: a pair of spheres, in quiescent fluid extending to infinity, falls faster than an isolated sphere, with a horizontal drift when the initial separation vector between the particles is oblique to gravity. The reversibility of Stokes flow [6] ensures that the separation vector stays constant. By the same token, a single apolar axisymmetric particle falls without rotating, drifting horizontally at a rate proportional to its constant tilt. However, for two sedimenting disks a rich phase-

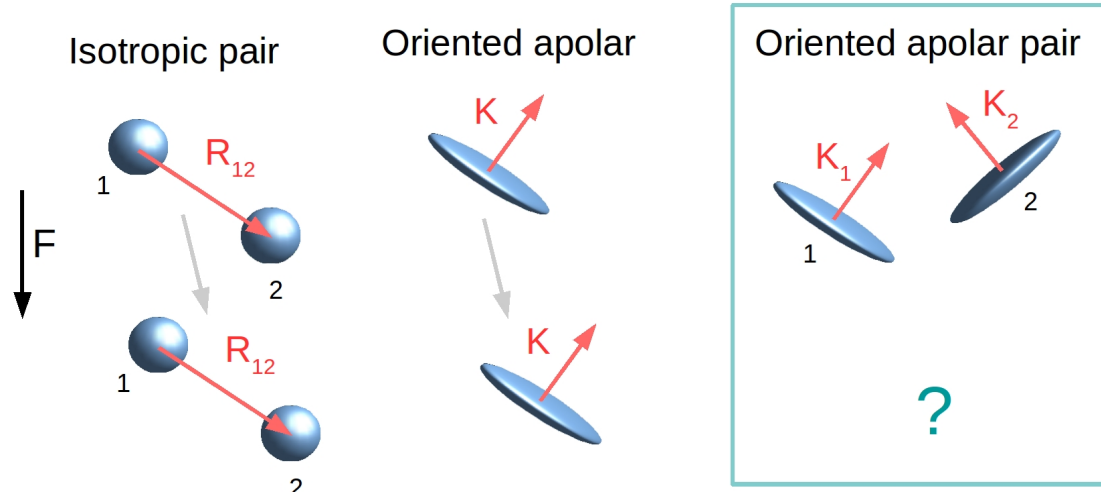


Figure 2.1: Stokesian time-reversal symmetry forbids two spheres or one disk to tumble, but allows nontrivial motion for a pair of disks.

space dynamics emerges, via mutual rotation due to a coupling between orientational and translational degrees of freedom [41, 36, 35, 33].

In this chapter, we present experiments that classify the possible dynamical behaviours of a settling pair of disks. We show that a symmetry-based far-field theory, without a detailed calculation of the mutual rotation coupling, accounts for the dynamics through the emergence of an effective Hamiltonian for this wholly dissipative system. Horizontal position and tilt in the presence of gravity thus precisely mimic coordinate and momentum, with an inherited time-reversal invariance. This emergent canonical dynamics persists in the many-disk problem, where it competes with the well-known velocity-fluctuations problem [23, 26, 21, 27, 5] in the sedimentation of isotropic particles.

2.2 Experiments

Our experiments are conducted on pairs of identical disks, with radius $a = 0.65$ cm, falling in viscous fluid ($\text{Re} \sim 10^{-4}$) in a quasi-two-dimensional container with dimensions of 30 cm x 50 cm x 5 cm (Width x Height x Depth). The fluid was transparent polydimethylsiloxane (silicone oil) of viscosity 60000 cSt and density 0.96 g cm^{-3} . The disks are of radius $a = 0.6$ cm, and 1 mm thickness; they are made of aluminium of density 2.7 g cm^{-3} . They were

made smooth using sandpaper and were spray painted black. As the disks fall under gravity, their dynamics are captured every 5 seconds with a NikonD700 DLSR camera. The images were converted to 8-bit, and thresholded after subtracting the background. The tracking was done by fitting an ellipse to the disks, with the centroid of the ellipse giving the positions (x_i, y_i) with an error of $\pm 0.02 a$ and orientation of the major axis giving θ_i of the disks with an error of $\pm 0.06^\circ$ [see Appendix 6.2]. In the next chapter we will discuss in detail the image processing and analysis, in the context of multiple settling disks.

As shown in Figure 2.2 the trajectory of the centres of the disks lie in a plane. Assuming translational symmetry in the $x - y$ plane, and taking advantage of the observation that there are no rotations due to torques about the x - and y -axes, the six coupled degrees of freedom can be reduced to two separation and two orientation degrees of freedom. Our observations suggest two qualitatively distinct trajectory types: scattering, in which the separation increases monotonically, and bound, in which separation and orientations oscillate with a characteristic amplitude and wavelength. The oscillatory behaviour further falls into two classes, to be discussed later.

We ask: (i) Is there a well-defined boundary in the space of initial conditions that separates periodic and scattering (i.e. infinite-wavelength) behaviour, or do our “scattering” states simply have a wavelength longer than the container height? (ii) What determines the emergent time period and wavelength of the periodic orbits?

Within the four-dimensional space of initial separations and orientations it is convenient to work with $x \equiv x_2 - x_1$, $y \equiv y_2 - y_1$, $\theta^- \equiv \theta_2 - \theta_1$ and $\theta^+ \equiv \theta_1 + \theta_2$. Here θ_i is measured with respect to the y -axis, defined to be $-ve$ in the first and fourth quadrant and $+ve$ in the second and third quadrant [Fig. 2.2]. We begin with the symmetric case with initial $\theta_1 = -\theta_2$ and $y = 0$. The resulting trajectories are symmetric, i.e. $\theta^+ = 0$ at all times [Fig. 2.3(a)]. For a small initial value x_o of the horizontal separation x , θ_i undergoes a full rotation and x oscillates periodically, as observed in experiments and simulations by Jung *et al.* [35]. As x_o is increased, the wavelength and amplitude of the oscillations increase sharply [Fig. 2.3(d)], until the terminal motion seems to approach the linear trajectories of isolated Stokesian disks [see Supplementary Video 1.1]. Finite container height makes it impossible to establish experimentally the existence of a threshold value of x_o at which the wavelength

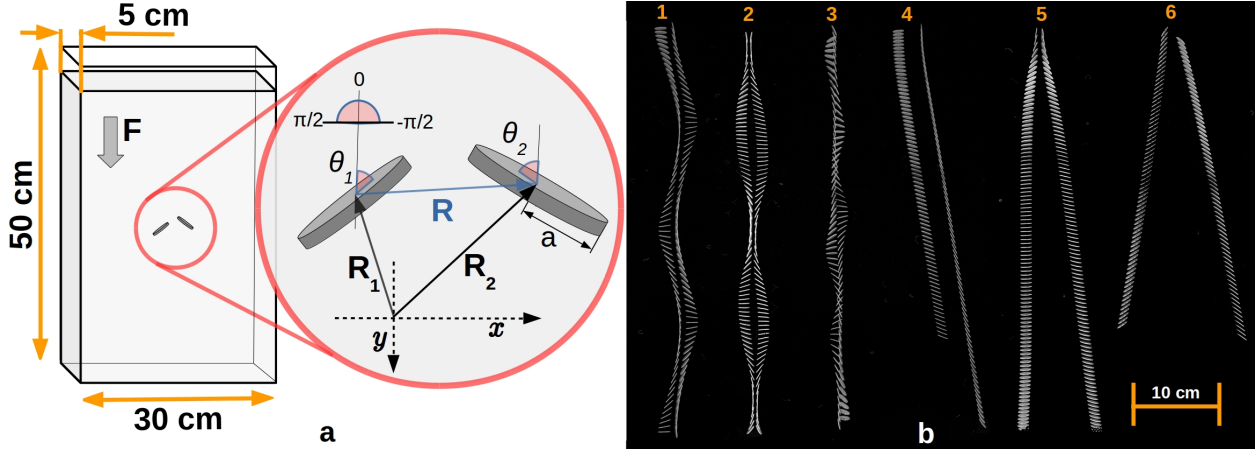


Figure 2.2: **Bound and scattering behaviour:** (a) A quasi-two-dimensional setup with disks released such that the vector normal to the disk and the separation vector $\vec{R} = \vec{R}_2 - \vec{R}_1$ lies in the plane of the settling geometry, (x,y) . The orientation of individual disks is quantified by angles θ_1 and θ_2 measured with respect to gravity, which is pointing along the \hat{y} direction. (b) Overlapped time frames showing pair dynamics observed in experiments. The numbers (1-6) denote dynamics generated by varying the initial separation (x_o, y_o) between the disks and their individual orientations $(\theta_i; i = 1, 2)$. These complex trajectories can be grouped into two broad classes: periodic bound (1-3) and scattering (4-6).

and amplitude actually diverge. A similar limitation applies to the numerical evidence for scattering orbits [34] using an expansion in a/R and the method of reflections [6, 12].

2.3 Far-field analysis

Working at leading order in a/R , we construct an effective Hamiltonian approach to the disk-settling problem and map the symmetric case to the gravitational Kepler problem, thus establishing the transition between periodic and scattering orbits. We then go on to explain the behaviours seen in asymmetric settling. We begin with an isolated settling disk. The leading order translational response of a spheroid to an external force \mathbf{F} is $\mathbf{U}_1 = [X_A^{-1}\mathbf{K}\mathbf{K} + Y_A^{-1}(\delta - \mathbf{K}\mathbf{K})] \cdot \mathbf{F} / 6\pi\eta a$. Here \mathbf{K} is the orientation vector, X^A and Y^A are resistance functions for spheroids [34]. Using the angle convention from Fig.2.2a, the horizontal velocity of an isolated settling disk is $\dot{x}_1 = F\alpha \sin 2\theta_1$, where F is its buoyant weight and the mobility

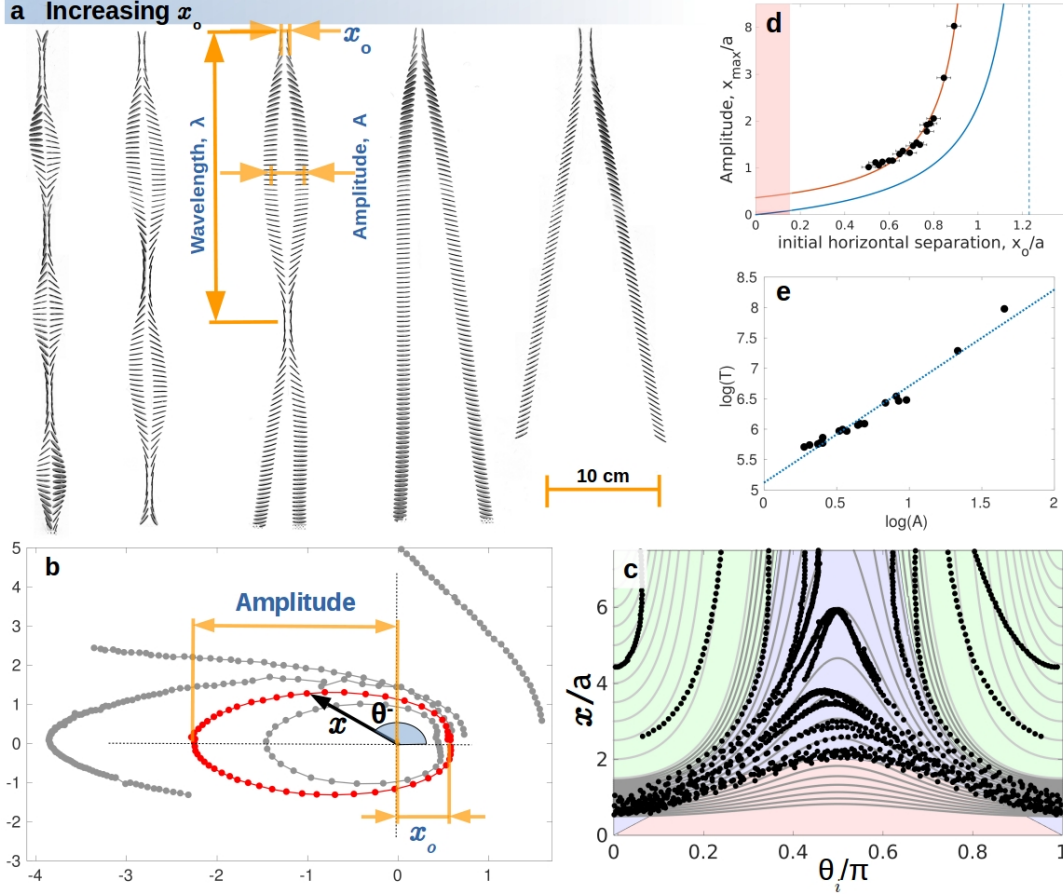


Figure 2.3: **Symmetric settling**: (a) Time-lapse images from the experiment, exhibiting a transition from periodic orbits to scattering trajectories with increasing initial horizontal separation x_o . Wavelength λ and amplitude A appear to diverge as x_o approaches a critical value. (b) Elliptical Kepler orbits for the bound states are clearly seen when the measured x and θ^- are displayed as radial and azimuthal coordinates respectively. (c) Trajectories in the $x-\theta_i$ plane, $i = 1, 2$, showing regions of bound and scattering trajectories. The grey curves are predicted by the far-field analysis: $1/x = 1/x_o + \frac{\pi}{8a}(\cos 2\theta_i - \cos 2\theta_{io})$, where θ_{io} , x_o are the initial values. Red, blue and green represent restricted, bound and scattering regions respectively. (d) Amplitude vs minimum separation fits $1/(x_o^{-1} - x_c^{-1}) + c$ with $x_c = 1.02a$ and $c = 0.725a$ (red curve), qualitatively consistent with the asymptotic far-field prediction (blue) $1/(x_o^{-1} - \pi/4a)$. Alternatively, x_c can be determined from the log-log plots of wavelength and amplitude vs $x_c - x_o$, giving $x_c = (1 \pm 0.032)a$. (e) Scaling of period T with amplitude A , $T \sim A^\nu$, with $\nu \simeq 1.588 \pm 0.11$ consistent with the $3/2$ of Kepler's third Law.

α is defined below. The tilt angle θ_1 remains constant due to Stokesian time-reversibility. We can thus view the trivial evolution of x_1 and θ_1 as the Hamiltonian dynamics of a free particle with momentum θ_1 and kinetic energy proportional to $\cos 2\theta_1$. This approach also applies to the two-disk case, where θ_1, θ_2 do not remain constant.

The second spheroid generates a velocity field which is calculated using the distribution of singularities at \mathbf{r}_2 . For the prolate case, it is a line distribution between the focal points:

$$\mathbf{v}_2(\mathbf{r}) = \mathbf{F}_2 \cdot \int_{-k_2}^{k_2} \left\{ 1 + (k_2^2 - r_2^2) \frac{(1 - e_2^2)^2}{4e_2^2} \nabla^2 \right\} \frac{\mathcal{G}(\mathbf{r} - \mathbf{r}_2)}{8\pi\eta} d\mathbf{r}_2 \quad (2.1)$$

Here $\mathcal{G}(r)_{ij}/8\pi\eta$ is the Green's function for Stokes flow and $k = ae$ with semi-major axis a and eccentricity e . For the case of oblate spheroid, the line integral is carried along a complex focal length ($k \rightarrow ik$), which is equivalent to a distribution of singularities on a disk of radius k in the perpendicular real subspace [59]. Vorticity of \mathbf{v}_2 evaluated at the singularity distribution of the first particle, placed at \mathbf{r}_1 , gives the leading contribution to the rotation of the first particle [34]:

$$\omega_1 = \frac{1}{8\pi\eta} \int_{-k_1}^{k_1} \frac{3}{4k_1^3} dr_1 \int_{-k_2}^{k_2} \frac{dr_2}{2k_2} (k_1^2 - r_1^2) \frac{\mathbf{F}_2 \times \mathbf{r}_{12}}{|\mathbf{r}_{12}|^3}, \quad (2.2)$$

here, $\mathbf{r}_{12} = \mathbf{r}_1 - \mathbf{r}_2$. The far-field approximation yields $\omega_1 = \mathbf{F}_2 \times \mathbf{R}/8\pi\eta R^3$, where \mathbf{R} is pointing from the centroid of particle 2 to the centroid of 1.

2.3.1 Planetary orbits

For symmetric settling, retaining the lowest non-vanishing contribution in an expansion in a/x , $\dot{x} = 2F\alpha \sin \theta^-$ and $\dot{\theta}^- = 2F\gamma/x^2$. The proportionality constants α and γ are determined by the solution for an isolated settling spheroid [32]. The mobility $\alpha = -(X_A^{-1} - Y_A^{-1})/12\pi\eta a$ and $\gamma = 1/8\pi\eta$, where the resistance functions $X_A = 8/3\pi$ and $Y_A = 16/9\pi$ [12] in the limiting case of $e = \sqrt{1 - b^2/a^2} \rightarrow 1$ for radius a and thickness b of the disk. The above far-field equations can be recast as Hamiltonian dynamics $\dot{x} = \partial_{\theta^-} \mathcal{H}$, $\dot{\theta}^- = -\partial_x \mathcal{H}$ with

$$\mathcal{H} \equiv 4F\alpha \sin^2 \frac{\theta^-}{2} + 2F\gamma/x \quad (2.3)$$

where $4F\alpha \sin^2 \frac{\theta^-}{2}$ and $2F\gamma/x$ play the roles of kinetic and potential energy respectively, with the $1/x$ coming from the viscous hydrodynamic kernel, not gravity. This is precisely

the reduced Hamiltonian for the Kepler problem [58] when expressed in terms of azimuthal angle θ^- and radial coordinate x [Fig. 2.3 (b)]. The solution

$$\frac{1}{x} - \frac{1}{x_o} = \frac{\alpha}{\gamma} (\cos \theta^- - \cos \theta_o^-) \quad (2.4)$$

to the equations of motion, obtained earlier by Kim [34] for far-field scattering trajectories, is simply the conservation of \mathcal{H} , describing both bound and scattering orbits [see Fig. 2.3(c)], with a transition as $x_o \rightarrow x_c = 4a/\pi$. Note that the observed amplitude diverges at $x_c = 1.02a$ which is smaller than $4a/\pi$ [see Fig. 2.3 d]. A circular Kepler orbit arises only for $\alpha = 0$, which is the case of a pair of identical spheres. Given the very close approach of the disks in a bound state, the far-field mapping to the Kepler problem bears up surprisingly well against experimental observations, as detailed in Fig. 2.3. There are two points to note apropos the discrepancy between theory and experiments in Fig. 2.3, when the disks are too close and too far apart, respectively – 1) In our analysis, the shape of the disk is lumped into just one parameter α , and disks can penetrate each other without hindrance. 2) When the disks are much far apart, the strength of hydrodynamic interaction between disks and the walls become of comparable magnitude to the inter-particle interactions. Addressing both these points in theory would require solving the full time-dependent boundary-value problem, which we do not pursue in this thesis.

Laplace-Runge-Lenz vector

The fact that a Hamiltonian description emerges as a Kepler problem tells us that a Laplace-Runge-Lenz vector has to exist. The trajectory for symmetric settling leads to Kepler orbits

$$\frac{l}{R} = 1 + e \cos \theta^- \quad (2.5)$$

where the *latus rectum* $2l$ and eccentricity of the orbit e are

$$l = \frac{\gamma/\alpha}{\gamma/\alpha R_o - \cos \theta_o^-}; \quad e = \frac{1}{\gamma/\alpha R_o - \cos \theta_o^-}; \quad (2.6)$$

The eccentricity vector for a gravitational Kepler orbit is

$$\vec{e} = \frac{\vec{v} \times (\vec{R} \times \vec{v})}{\Gamma} - \frac{\vec{R}}{|R|}, \quad (2.7)$$

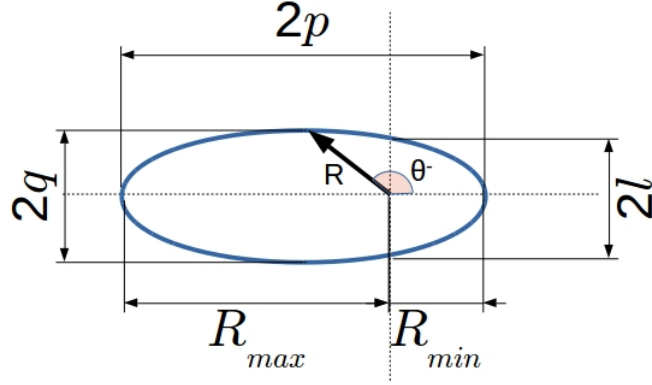


Figure 2.4: Bound orbit for symmetric case where R and θ^- play the role of radial and azimuthal coordinates, respectively.

Γ being the gravitational parameter [which would be $(m_1 + m_2)G$ for a pair of masses m_1 , m_2 , where G is the gravitational constant]. In our system of sedimenting disks, the velocity in the above analysis corresponds to that in Fig. 2.3 b: $\vec{v} = \alpha \sin \theta^- \hat{r} + \frac{\gamma}{R} \hat{\theta}$. This gives the specific angular momentum $\vec{R} \times \vec{v} = \gamma \hat{z}$, which, from (2.7), implies

$$\vec{e} = \left(\frac{\gamma^2}{\Gamma R} - 1 \right) \hat{r} - \frac{\gamma \alpha}{\Gamma} \sin \theta^- \hat{\theta} \quad (2.8)$$

From (2.4) we know $1/R = 1/R_o + \alpha(\cos \theta^- - \cos \theta^-_o)/\gamma$. Rewriting (2.8) in terms of θ^- and transforming to cartesian vectors, $\hat{r} = \cos \theta^- \hat{x} + \sin \theta^- \hat{y}$, $\hat{\theta} = -\sin \theta^- \hat{x} + \cos \theta^- \hat{y}$ gives

$$\vec{e} = \left[\frac{\gamma^2}{\Gamma} \left(\frac{1}{R_o} - \frac{\alpha}{\gamma} \cos \theta^-_o \right) - 1 \right] (\cos \theta^- \hat{x} + \sin \theta^- \hat{y}) + \frac{\alpha \gamma}{\Gamma} \hat{x} \quad (2.9)$$

We define the gravitational parameter $\Gamma \equiv \gamma^2 \left(\frac{1}{R_o} - \frac{\alpha}{\gamma} \cos \theta^-_o \right)$, ensuring that the resulting magnitude of eccentricity is the same as (2.6). This implies that $\vec{e} = \hat{x}/(\gamma/\alpha R_o - \cos \theta^-_o)$. Thus \vec{e} is a conserved quantity, pointing along the \hat{x} axis with a constant magnitude depending on initial θ^-_o and separation R_o . The Laplace-Runge-Lenz vector is

$$\vec{A} = \Gamma \vec{e} = \alpha \gamma \hat{x} \quad (2.10)$$

which is therefore also constant. Note: \hat{x} is an abstract direction defined using the separation of the disks as the radial coordinate and the tilt angle θ^- as the azimuthal coordinate. Note also that both angular momentum $\vec{R} \times \vec{v}$ and the Laplace-Runge-Lenz vector \vec{A} are completely

independent of initial conditions.

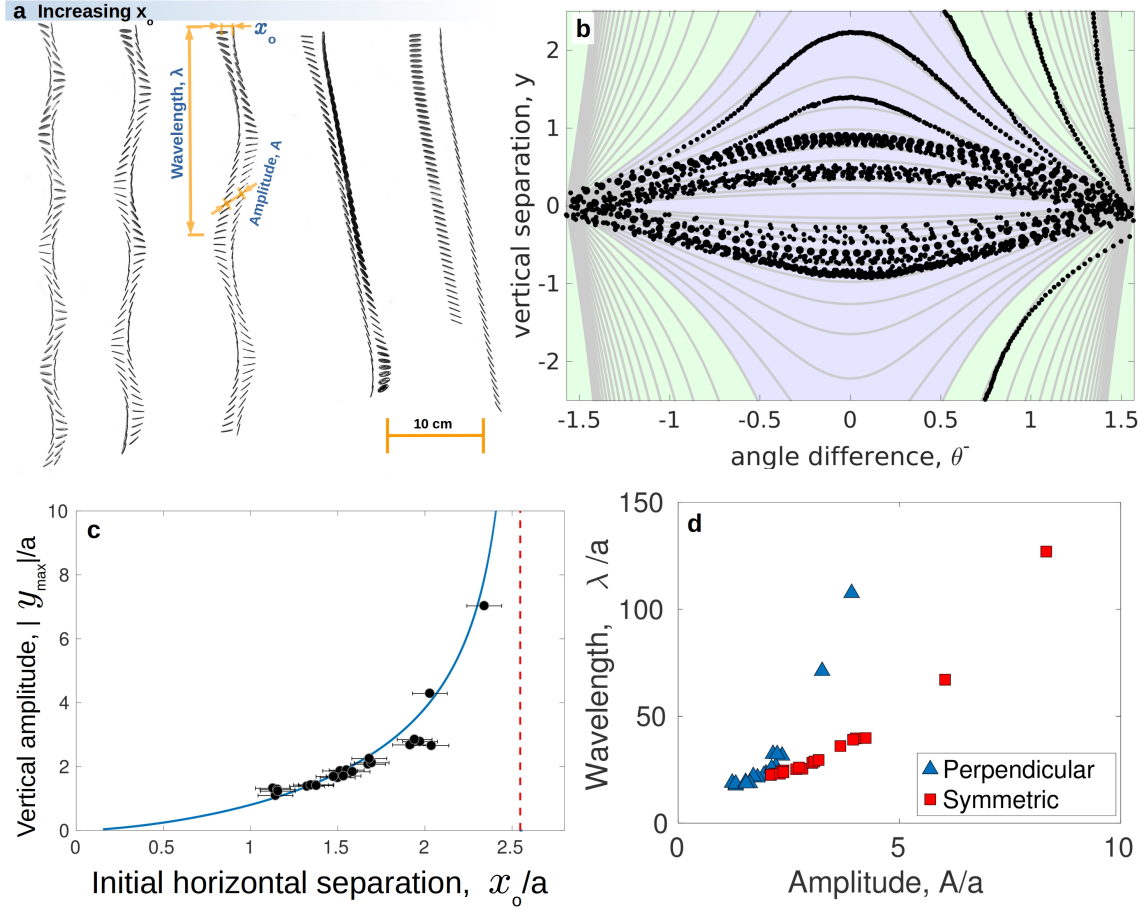


Figure 2.5: **Perpendicular initial condition:** (a) Time-lapse images from the experiment, when the disks are released with perpendicular initial orientations. From left to right, the initial horizontal separation x_o is increased, leading to a divergence in vertical separation y . (b) Experimental trajectories in the θ^- - y plane represented by points, compared with the far field result plotted in grey solid lines: $y = \pm x_o \cos \theta^- / \sqrt{(8a/\pi x_o)^2 - \cos^2 \theta^-}$. Blue and green regions in the phase diagram represent bound and scattering regions respectively as predicted by far-field analysis. (c) Divergence of the amplitude of y oscillations is captured by plotting the maximum value of y/a as a function of initial horizontal separation x_o/a . The solid curve is the far-field prediction of amplitude: $A(x_o) = x_o / \sqrt{(8a/\pi x_o)^2 - 1}$, with the red dotted line representing the critical $x_o = 8a/\pi$. (d) The observed wavelength λ/a increases more strongly as a function of amplitude A/a for the perpendicular case (blue) as compared to the symmetric case (red).

2.3.2 Beyond planetary orbits

A simple case of asymmetric initial conditions consists of releasing the disks at the same height with their normal vectors perpendicular to each other, $\theta^+ = \pi/2$ [Figure 2.5 a-c]. Once again, periodic dynamics in the orientation is observed, with the added complexity of y oscillating between positive and negative values, and an apparent transition to unbounded orbits with increasing x_o .

The effective Hamiltonian description above provides a useful framework for understanding the dynamics resulting from a more general set of initial conditions $(x_o, y_o, \theta^+, \theta^-_o)$. A reduction to effective two-dimensional dynamics can be achieved for asymmetric initial conditions $\theta^+_o \neq 0$ as well, and periodic behaviour is preserved but more complex [Figs. 2.5 and 2.7]. The resulting non-Keplerian behaviour can be understood by extending equation 2.3 to incorporate the dependence of the angular velocity of the disks on the angle between the separation vector \mathbf{R} and the external force \mathbf{F} . To leading order in a/R , the angular velocities of disks are equal and opposite, $\dot{\theta}_1 = -\dot{\theta}_2 = \gamma \mathbf{F} \times \mathbf{R}/R^3$. With this additional ingredient, we get the general equations of motion

$$\dot{x} = 2F\alpha \sin \theta^- \cos \theta^+, \quad \dot{y} = -2F\alpha \sin \theta^- \sin \theta^+ \quad (2.11)$$

$$\dot{\theta}^- = 2F\gamma \frac{x}{R^3}, \quad \dot{\theta}^+ = 0. \quad (2.12)$$

Here α and γ are the same as before (2.3). From equation (2.11) we get the relation between x and y

$$\frac{dx}{dy} = -\frac{2\alpha}{\beta} \cot \theta^+ = -\cot \theta^+; \quad x - x_o = -\cot \theta^+(y - y_o). \quad (2.13)$$

Here, x_o and y_o are the initial x and y respectively. The conservation of θ^+ in (2.12) constrains the dynamics of x and y to a line with slope $-\tan \theta^+$, reducing the number of variables to two, thus allowing phase plane analysis. Rewriting equations (2.11) and (2.12) in terms of the arc length $S = |\vec{R} - \vec{R}_o| = \sqrt{(x - x_o)^2 + (y - y_o)^2} = (x - x_o) \sec \theta^+$ (see figure 2.6) and θ^- gives

$$\frac{dS}{dt} = \frac{\partial}{\partial \theta^-} (-2F\alpha \cos \theta^-); \quad \frac{d\theta^-}{dt} = -\frac{d}{dS} \frac{2F\gamma(y_o - S \sin \theta^+)}{(y_o \cos \theta^+ + x_o \sin \theta^+) |\vec{S} + \vec{R}_o|}. \quad (2.14)$$

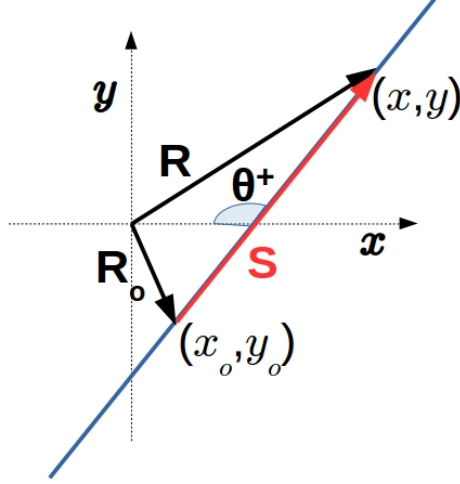


Figure 2.6: Trajectory in $x - y$ plane is used to define the canonical variable S for the construction of an effective Hamiltonian.

Thus the dynamics of S and θ^- is given by $\dot{S} = \partial_{\theta^-} \mathcal{H}$, $\dot{\theta}^- = -\partial_S \mathcal{H}$, with effective Hamiltonian

$$\mathcal{H} \equiv 4F\alpha \sin^2 \frac{\theta^-}{2} + 2F \frac{\bar{\gamma}(S)}{R(S)} \quad (2.15)$$

where $\bar{\gamma}(S) \equiv \gamma(y_o - S \sin \theta^+) / (y_o \cos \theta^+ + x_o \sin \theta^+)$ and $R(S) = (S^2 + R_o^2 + 2Sx_o \cos \theta^+ + 2Sy_o \sin \theta^+)^{1/2}$. Note that, in the limit $\theta^+ \rightarrow 0$, Kepler orbits are realised for more general initial separations with $y_o \neq 0$.

The Hamiltonian (2.15) for $\theta^+ = \pi/2$ implies a dynamics with y oscillating between positive and negative values given by $y = \pm x_o \cos \theta^- / \sqrt{(8a/\pi x_o)^2 - \cos^2 \theta^-}$, constant x , and, with increasing x_o , a transition from periodic to unbound orbits at $x_c = 8a/\pi$ [see Appendix 6.3]. These are in accord with observations [see Figure 2.5 and Supplementary Video 1.2], though the experiments additionally show small oscillations in x possibly arising from near-field effects and small imprecision in initial release angles.

2.3.3 Rocking dynamics

Rocking – a qualitatively distinct periodic behaviour analogous to libration in a pendulum, in which θ^- oscillates in a limited range – emerges for $\pi/2 < \theta^+ < \pi$ [see Supplementary Video 1.3]. Releasing the disks with $\theta_1 = \pi/2$ and decreasing $-\theta_2$ from $\pi/2$ (symmetric

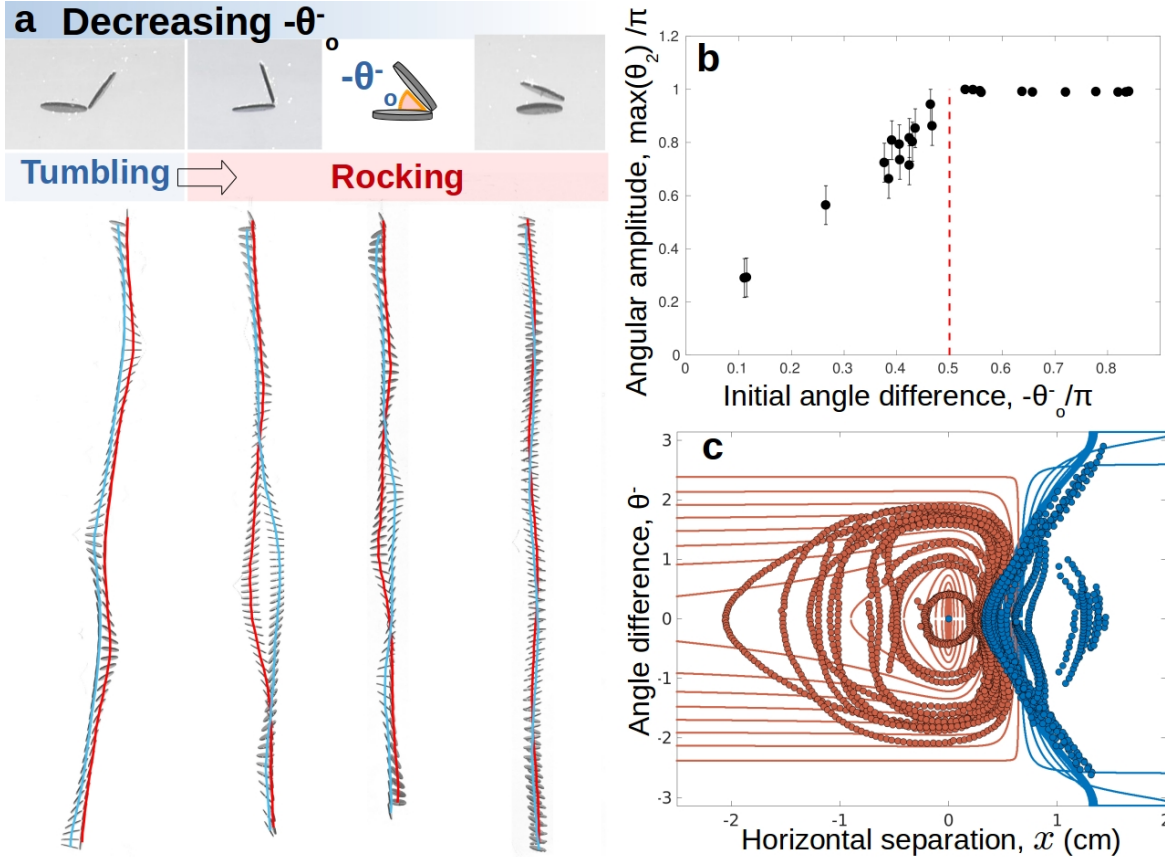


Figure 2.7: **Tumbling to rocking transition:** (a) As initial θ_o^- decreases there is a crossover from tumbling to rocking dynamics. Trajectory of the disk on the right (red) exchanges the relative x position with the trajectory of the disk on the left (blue) except for the first trajectory where $-\theta_o^- > \pi/2$. (b) To capture the transition from rocking to tumbling, the maximum angle of the disk on the right is plotted as a function of initial $-\theta_o^-$. We observe a transition from rocking to tumbling at initial $-\theta_o^- = \pi/2$ (dotted red line), consistent with the far-field calculation. (c) The trajectories are plotted in the $x - \theta^-$ plane, red symbols represent rocking motion and blue symbols represent tumbling. The corresponding red and blue solid curves represent the far-field prediction of rocking and tumbling dynamics, respectively [see Appendix 6.3].

case) towards zero we experimentally capture the tumbling-rocking transition at $\theta_o^- = -\pi/2$ [see Figure 2.7 (a) and (b)]. Unlike in tumbling, in rocking orbits the sign of x and hence, from (2.12), of $\dot{\theta}^-$, alternates as the particles interchange their relative horizontal positions. Except for the special cases of parallel and perpendicular release, rocking dynamics is best viewed in the x, y and θ^- space albeit with proportional x and y displacements. Figure

2.7(c) shows the trajectories projected on the $x-\theta^-$ plane. The tumbling-rocking transition can once again be understood in terms of the effective Hamiltonian (2.15). The extension to the case of dissimilar disks is discussed in the last chapter of the thesis.

2.4 Scaling analysis and Kepler's third law

For both symmetric and perpendicular initial conditions, the time period diverges at the boundary between bound and scattering orbits. Assuming that the ratio of thickness to radius of the disks is negligibly small, we have two length scales in the problem: the radius a of the disk and the separation R between the particles. One expects the period $T = (a^2\mu/F)f(R/a, \text{Re}, \text{Fr}, \theta^+_o, \theta^-_o)$, where the scaling function f depends on the initial conditions, as well as on the Reynolds number $\text{Re} = \rho U a / \mu \simeq 10^{-4}$ and Froude number $\text{Fr} = U / \sqrt{g a} \simeq 10^{-3}$ both of which are negligibly small. Here, we calculate the scaling functions for the symmetric and perpendicular initial conditions, and arrive at the Kepler's third law and deviations from it in these two cases.

(i) Symmetric, $\theta^+ \rightarrow 0$

For $\theta^+ \rightarrow 0$ with arbitrary initial separation $R_o = \sqrt{x_o^2 + y_o^2}$ and initial angle θ^-_o , the resulting trajectory becomes elliptical if separation R and angle difference θ^- is mapped to the radial coordinate and azimuthal angle respectively. The semi-major axis p and semi-minor axis q of this ellipse [see Fig.2.4] are

$$p = R_{max} R_{min} \left(\frac{1}{R_o} - \frac{\pi \cos \theta^-_o}{8a} \right); \quad q = (R_{max} R_{min})^{1/2} \quad (2.16)$$

respectively, with $R_{max} = \frac{8a/\pi}{8a/\pi R_o - \cos \theta^-_o - 1}$ as the maximum separation and $R_{min} = \frac{8a/\pi}{8a/\pi R_o - \cos \theta^-_o + 1}$ as the minimum separation for a given initial configuration (R_o, θ^-_o) . The trajectories become mirror symmetric when $y_o = 0$, making $R = x$ at all times. Using the conservation of orbital angular momentum $R^2 \dot{\theta}^- = 2F\gamma$ from (2.3), which is a consequence of the shape apolarity of the disks, we find the time period T of the orbit by calculating the area of the ellipse $\pi p q$,

$$T = \frac{8\pi^2\mu}{F} R_{max}^{3/2} R_{min}^{3/2} \left(\frac{\pi}{8a} + \frac{1}{x_o} - \frac{1}{x_c} \right). \quad (2.17)$$

Here $x_c = 8a/\pi(\cos\theta^-_o + 1)$ is the critical value of initial x_o at which the amplitude R_{max} diverges. Time period can be written as $T = \frac{a^2\mu}{F} f(x_o/a, \theta^-_o)$ with the scaling function,

$$f\left(\frac{x_o}{a}, \theta^-_o\right) = \frac{8^3 \left(\frac{8a}{\pi x_o} - \cos\theta^-_o\right)}{\left(\frac{8a}{\pi x_o} - \cos\theta^-_o - 1\right)^{3/2} \left(\frac{8a}{\pi x_o} - \cos\theta^-_o + 1\right)^{3/2}}. \quad (2.18)$$

When x_o approaches x_c the time period diverges with amplitude as $T \sim A^{3/2}$. Since the wavelength λ scales as $\lambda \sim TF/a\mu$ it diverges the same way as T .

(ii) Perpendicular, $\theta^+ \rightarrow \pi/2$

The solution of (2.14) in the limit $\theta^+ \rightarrow \pi/2$ is

$$\frac{y_o - y}{R} = \frac{\pi x_o}{8a} (\cos\theta^- - \cos\theta^-_o) \quad (2.19)$$

When the initial angle $\theta^-_o = \pi/2$ and initial $y_o = 0$, the trajectories take the form of an ellipse: $l/r = 1 + e \cos\phi$, if we map the square of separation R^2 to the radial coordinate r and $2\theta^- - \pi$ to the azimuthal angle ϕ . Here the *latus rectum* $2l$, eccentricity of the orbit e , semi-major axis p and semi-minor axis q are

$$\begin{aligned} l &= \frac{2a^2}{2a^2/x_o^2 - (\pi/8)^2}; & e &= \frac{(\pi/8)^2}{2a^2/x_o^2 - (\pi/8)^2}; \\ p &= \frac{R_{max}^2}{2} \left(2(8a/\pi x_o)^2 - 1\right); & q &= \frac{8a}{\pi} R_{max}. \end{aligned} \quad (2.20)$$

here $R_{max} = x_o/\sqrt{(8a/\pi x_o)^2 - 1}$ is the maximum separation or amplitude of the oscillation. From equation (2.14) we have $R^3\dot{\theta}^- = 2F\gamma x_o$, which can be written in terms of r and ϕ as

$$\frac{1}{2\sqrt{r}} r^2 d\theta^- = 2F\gamma x_o dt \quad (2.21)$$

Integrating by parts, while noting that $r^2 d\phi/2$ is the area $p q \phi/2$ of an elliptical sector, and using (2.19), gives

$$2F\gamma x_o T = \frac{\pi p q}{x_o} - \frac{\pi p q}{32a} \int_0^{2\pi} d\phi \sqrt{\left(\frac{8a}{\pi x_o}\right)^2 - \frac{1}{2} + \frac{\cos\phi}{2}}$$

which has the form of a complete elliptic integral $E[\phi/2, (\pi x_o/8a)^2]$. Inserting the value of p and q from (2.20) gives the scaling form of the time period $T = \frac{32a x_o \mu}{F} f(x_o/a)$, with the

scaling function

$$f(x_o/a) = \frac{2 \left(\frac{x_c}{x_o}\right)^2 - 1}{\left[\left(\frac{x_c}{x_o}\right)^2 - 1\right]^{3/2}} \left(\pi - \left(\frac{x_o}{x_c}\right)^2 E \left[(x_o/x_c)^2 \right] \right) \quad (2.22)$$

The critical value of x_o at which $f(x_o/a)$ diverges is $x_c = 8a/\pi$. As $x_o \rightarrow x_c$ the time period T diverges as

$$T = \frac{256 a^2 \mu}{F \left[\left(\frac{x_c}{x_o}\right)^2 - 1 \right]^{3/2}} \quad (2.23)$$

in terms of amplitude A , time period goes as $T \sim A^3$ as $x_o \rightarrow x_c$. We thus find that the wavelength $\lambda \sim TF/a\mu$ diverges more strongly ($\sim A^3$) for the perpendicular case than for the symmetric case ($\sim A^{3/2}$ Kepler's 3rd Law), a trend consistent with our observations (see Figure 2.4 d).

2.5 A peculiar Hamiltonian for multiple disks

The two-particle processes discussed above can be used as a building block to study the coupling of positions and orientations in multiple disks settling in our geometry [see Fig.2.2], within the far-field description [51, 26, 29]. Let (x_m, y_m) be the position of the m^{th} particle. At each location r_m , define $\vec{U}(r_m) \equiv \sum_{n \neq m}^N F \mathbb{G}_{xy}(r_m - r_n) \hat{x} + F \mathbb{G}_{yy}(r_m - r_n) \hat{y} + F \alpha \hat{y}$, where \mathbb{G}_{ij} is the Oseen tensor [6, 12] and m, n are particle labels. Pairwise addition of forces and torques at position r_m due to particles at other locations r_n gives the coupled dynamics of the m^{th} disk:

$$\dot{x}_m = F \alpha \sin 2\theta_m + U_x, \quad \dot{y}_m = F \alpha \cos 2\theta_m + U_y \quad (2.24)$$

and

$$\dot{\theta}_m = -\frac{F\gamma}{2} \frac{\partial}{\partial x_m} \sum_{n \neq m}^N \frac{1}{\sqrt{(x_m - x_n)^2 + (y_m - y_n)^2}}. \quad (2.25)$$

From (2.24) & (2.25) we can show that the dynamics in the (x, θ) space can be viewed as an effective Hamiltonian dynamics riding on the y -averaged background flow, $\dot{x}_m = \partial_{\theta_m} \mathcal{H}^X + \overline{U}_x(x_m)$, $\dot{\theta}_m = -\partial_{x_m} \mathcal{H}^X$ where the effective Hamiltonian takes the form

$$\mathcal{H}^X \equiv \sum_{m=1}^N F \alpha \sin^2 \theta_m - \sum_{n \neq m}^N F \gamma \int L(x_m - x_n) dx_m \quad (2.26)$$

where the expressions for L and $\overline{U_x}$ can be obtained from the steady-state average of (2.24) and (2.25) over the y coordinates. $\overline{U_x}$ contains the giant velocity fluctuations of [23] and possible screening mechanisms à la ref. [26, 21, 27, 5] and the “potential energy” term containing γ in (2.26) incorporates the tilt-induced lateral drift [29]. This formulation in terms of y -averaged dynamics is useful for the purposes of this chapter. However, a more powerful construction of the effective Hamiltonian sector of the dynamics for multiple spheroids will be presented in chapter 4.

2.6 Conclusion

Our experiments have uncovered rich dynamics in the zero-Reynolds-number settling of a pair of identical disks, with a well-defined boundary between bound and scattering orbits and two distinct classes of periodic bound-state motion. Despite limited accuracy in locating the bound-scattering boundary, and excluding extreme situations where a disk is in the hydrodynamic shadow of another [see Supplementary Video 1.4], the far-field hydrodynamic interaction offers a satisfactory and detailed understanding of the dynamics, even close to particle contact. It should be clear that our analysis is applicable to any uniaxial shape with fore-aft symmetry along the symmetry axis. Unexpectedly, the conservative dynamics generated by an effective Hamiltonian governs this viscosity-dominated system, with the tilt of the disks playing the role of momentum. For a large family of initial conditions the problem maps precisely to that of Kepler orbits. We find and account for a distinct family of orbits with no planetary-orbit analogue, where the angle executes oscillations over a limited range. For the many-disk problem, a y -averaged treatment yields Hamiltonian dynamics for (x, θ) as conjugate variables, riding on a background carrying the velocity fluctuations of sedimenting spheres [26, 21, 27, 5].

Chapter 3

Experiments on Sedimenting Disk

Arrays: Two Dynamical Regimes

This chapter is an elaboration of the experimental results presented in R. Chajwa et al., Phys. Rev. X **10**, 041016 (2020). (©2020 American Physical Society) [Open Access link](#)

3.1 Introduction

The statistics of number fluctuations in sedimentation have been studied for collections of apolar [39, 42, 47] and polar [29] anisotropic particles in a steady state with spatially uniform mean concentration. Sedimenting lattices, on the other hand, break translation invariance and thus retain a reference microstructure [65] about which they display rich dynamics [51, 52, 20, 53, 54, 55] distinct from that of the uniform suspension. In addition, the presence of a lattice clarifies the connection between particle-level interactions and long-wavelength collective phenomena as seen in Crowley’s celebrated clumping instability [51, 52] of a regular array of sedimenting Stokesian spheres with purely hydrodynamic interactions. How particle anisotropy transfigures this inescapable instability [64, 5, 63, 42] of sphere arrays is the central theme of this chapter.

Here, we pursue this question experimentally through the simple yet unexplored case of a freely sedimenting linear array of orientable apolar particles. Such a particle in isolation, aligned obliquely and settling under gravity, drifts laterally [see Figure 3.1 (c)] with a velocity

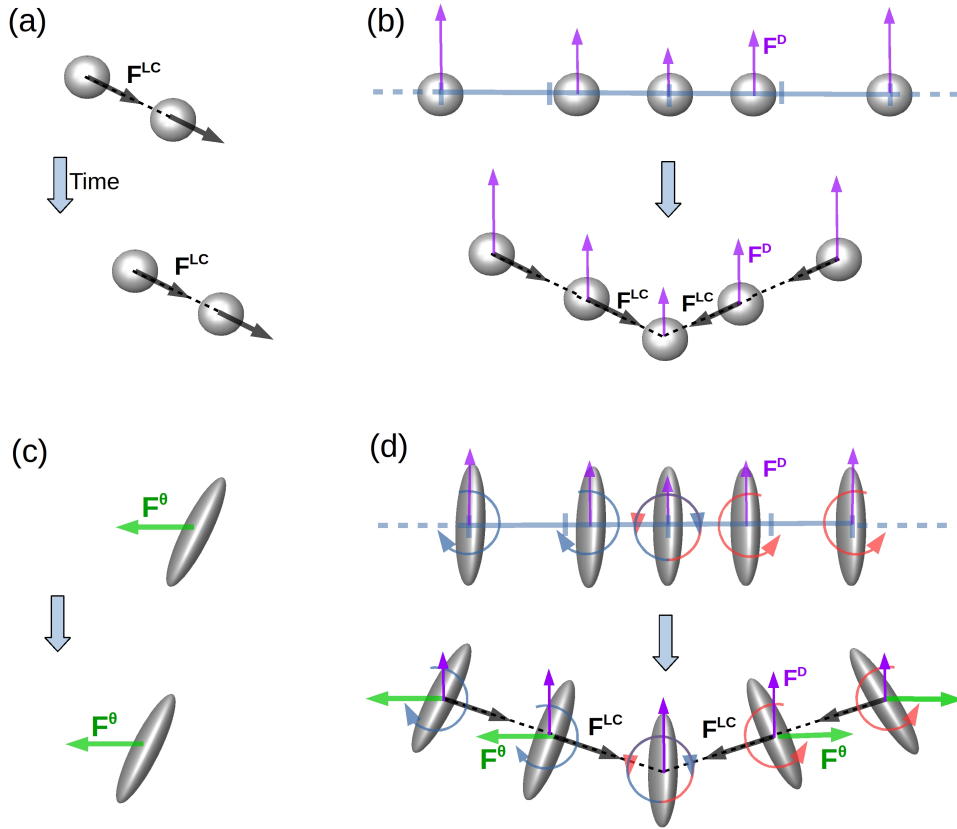


Figure 3.1: **Schematic of competing mechanisms:** (a) F^{LC} acts on the pair along the line joining their centers leading to horizontal drift. (b) Clumping of the array of spheres results from the line of centres force F^{LC} , acting along with reduced drag force F^D . (c) A spheroid drifts laterally as it falls when it is oriented obliquely with respect to gravity (d) Lateral drift F^θ competing with the clumping induced by F^{LC} and F^D .

that depends, for a given orientation, on the particle geometry through a mobility function [6] whose analytical form is known for spheroids [32, 34]. When a collection of such particles settle in an array, the lateral drift \mathbf{F}^θ of an individual particle with tilt angle θ can compete with the line-of-centers force on a pair of particles \mathbf{F}^{LC} , potentially preventing the clumping instability [see Figure 3.1 (d)]. We, therefore, ask: is a sedimenting lattice of oriented objects stable?

We answer this question for a system of disks, that is, oblate spheroids with eccentricity $e \rightarrow 1$, as they display the most pronounced lateral drift [32, 12, 34]. We note further that,

despite their ubiquity in nature, the sedimentation of disk-like objects is much less studied than that of their rod-like counterparts [42, 47].

3.1.1 Overview of the setup

Our experiments were conducted with disks of radius $a=0.4$ cm and thickness 1 mm, 3D printed using resin of density 1.164 g cm^{-3} , settling in Silicone oil of density 0.98 g/cc

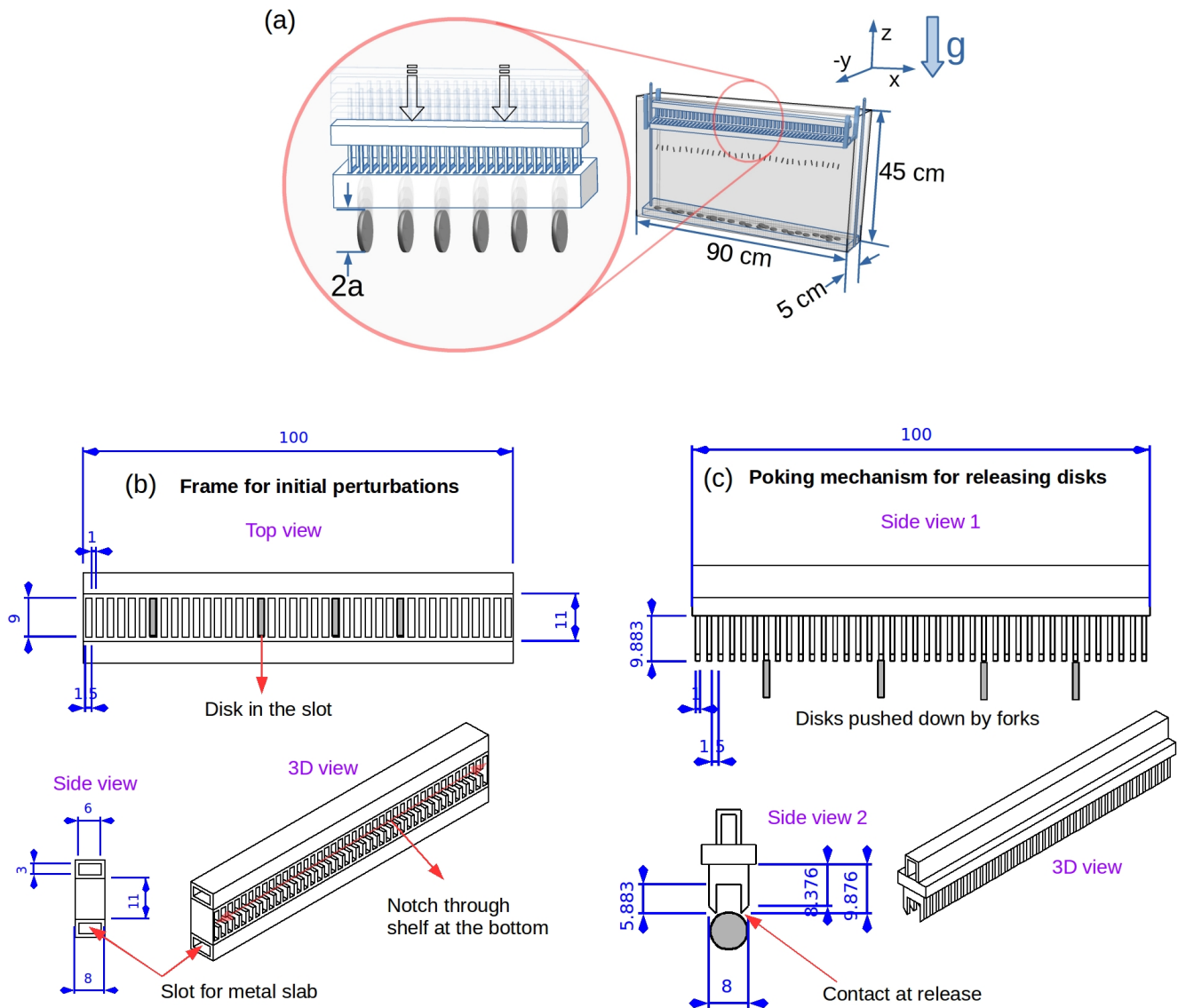


Figure 3.2: (a) Schematic of the experimental setup. (b) & (c) Release mechanism. The measurements of the release mechanism are given in millimeters

and kinematic viscosity 5000 cSt, leading to a typical Reynolds number $Re \sim 10^{-4}$. The particles are released in a one-dimensional array from the top of a quasi-two-dimensional glass container of width (x -direction) = $225 a$, height (z -direction) = $112.5 a$, and depth (y -direction) = $12.5 a$. As shown in Figure 3.11 (a), the disks were initially placed with their surface normals \mathbf{K} perpendicular to gravity and parallel to the line joining the disk centers. This was achieved by placing the disks in slots separated with a center-to-center spacing of $0.625a$ within a frame centered in the midplane of the quasi-two-dimensional container. The clearance of each disk in its slot geometrically sets a precision of $0.0625a$ in the horizontal position, a deviation of up to 1.8° in orientation from the vertical, and negligibly small differences in initial vertical positions. The main source of errors in the orientations and positions at the release comes from physical aspects of the problem, which is discussed later. Both the frame and the disks are already submerged in the fluid to suppress air bubbles that would otherwise affect the sedimentation. The disks are then ejected from the slots at the same time with a comb whose teeth fit the slots in the array. The centers of the discs and their surface normals lie in the central (x, z) plane of the experimental geometry for much of their trajectory.

3D printing

The disks, release mechanism, and holders were designed in FreeCAD and 3D printed using a FormLabs SLA printer with stereolithography. The support material and the printed parts were both made with the same resin of density 1.164 g cm^{-3} . The parts were printed with contact points with the support, and cut carefully and washed in isopropyl alcohol for 15 minutes to remove the debris of the support. The parts were then exposed to UV light for 30 minutes, hardening the resin. The remains of the contact points are then sanded to give smooth surfaces. This cutting and sanding process is somewhat delicate for disks and poking mechanism. We colored the disks using a black permanent marker which adds negligible mass and is not dissolved or degraded significantly in silicone oil.

3.2 Release mechanism

The experiment is conceptually simple, but technically challenging due to the difficulty in accurately releasing multiple oriented objects in a highly viscous fluid. We believe we have achieved considerably greater precision in this regard than other experiments in the field. Even for homogeneous suspensions, the experimental study of linear stability has been elusive due to the difficulty in creating an initial homogeneous steady state. Although the slow viscous dynamics makes small temporal imprecision at the time of release unimportant, it is accompanied by some experimental difficulties which we address here:

(a) *Air bubbles* – entrainment of air parcels along with the disks and the release mechanism forms a source of significant errors in the initial conditions [see Figure 3.3]. One has to wait for hours for bubbles to escape the fluid completely, making the already slow experiments even slower. The bubbles were observed to form a stationary configuration at the contact between the disks and the frame, creating random initial perturbations, and even completely forbidding the release of some disks from the frame. The bubbles were also observed to adhere to the falling disks throughout the trajectory, leading to further errors in the effective buoyancy of the disks. To minimize these errors we keep the release mechanism completely submerged roughly 3 cm below the surface of the fluid throughout, except when taking the particles out of the container. We retrieve the particles from the bottom of the

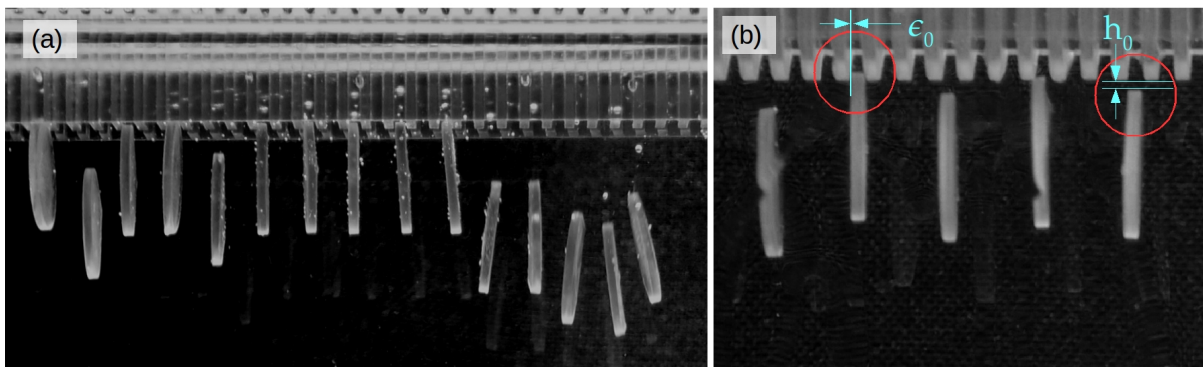


Figure 3.3: (a) Air bubbles interfering with the release. (b) Lubrication interaction between a trial release mechanism and the disks creating a random vertical perturbation.

container using a narrow basket crafted out of plastic mesh. Placing this basket back in the container ends up creating air bubbles. Thus, after taking the particles out, we place the frame back into the fluid and wait overnight for bubbles to escape. We keep the disks in a jar containing the same oil, further reducing the entrainment of air bubbles. While creating the initial configuration, by placing the disks in the frame one-by-one using forceps we move the disk inside the fluid to get rid of any bubbles. The poking mechanism brings in air bubbles but the spacing between the teeth and frame [see Figure 3.2 (b)] allows the bubbles to cleanly escape the fluid over the release mechanism.

(b) *Lubrication interaction* – At the time of release, there are two small ($\ll a$) length scales at play: the vertical distance between the surface of the frame and the disk h_0 , and the horizontal clearance between the disks and the slot ϵ_0 . The hydrodynamic drag in the lubrication approximation scales as h_0^{-1} and $\ln(\epsilon_0^{-1})$, which diverge at small h_0 and ϵ_0 , and thus dominate the process of disk release [see Figure 3.3 (b)]. For an experimentally precise initial configuration in which the disks are all aligned parallel to each other, we require the disks to be aligned with the slots at the time of release, so we keep the clearance as small as possible. At the same time, if we push the disks completely out of the slots to increase h_0 , this alignment is disturbed, creating errors in the orientations. To minimize the effect of lubrication errors, we create notches in every slot at the bottom of the frame [see Figure 3.2 (b)], so there is no contact¹ between the slots and the disks at release. In addition, we design the poking mechanism such that it carefully pushes the disks completely out of the slots with a point contact. However, the minimization of lubrication forces is traded off with small errors in the orientations. We will discuss later the consequences of this error. Note here that the air bubbles and lubrication can work together to spoil the initial configuration as seen in Figure 3.3 (a), and it is our endeavour to reduce this effect.

(c) *Out of plane dynamics* – We choose to confine the disk-array dynamics to two dimensions in order to capture the physics of coupling between an orientational and translational degree in the simplest possible setting. A particular advantage of this quasi-two-dimensional geometry is that the close walls are a momentum sink, effectively truncating the hydrodynamic interactions between disks at the level of nearest neighbours. The confinement of our

¹A thin fluid layer prevents true contact between solid bodies in the Stokesian regime.

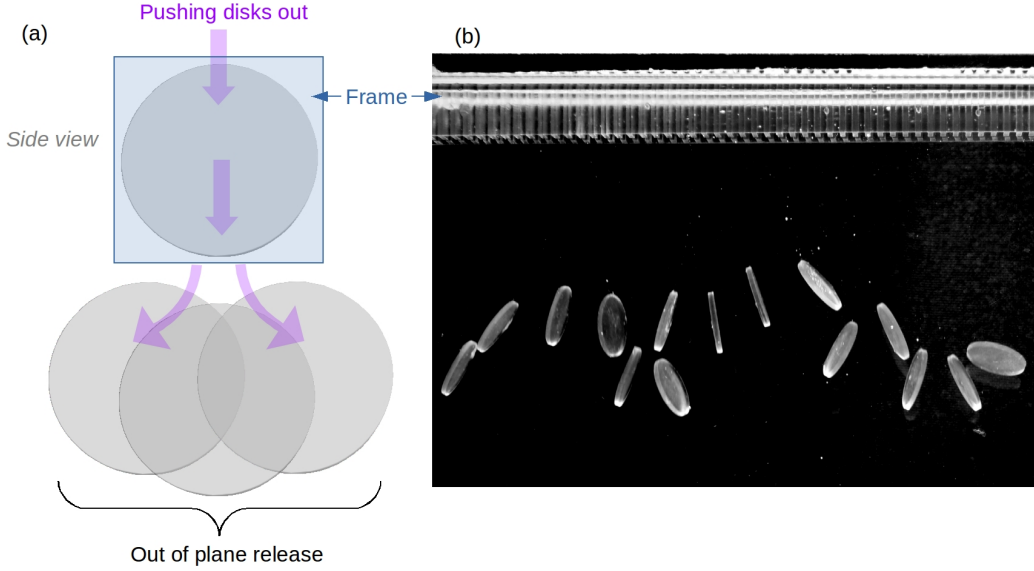


Figure 3.4: (a) Schematic side view of the release, depicting the out-of-plane release. (b) Experimental configuration resulting from out-of-plane initial condition.

experimental geometry in the y direction sets a interaction cutoff length scale of about $12a$ in the (x, z) plane. The lattice spacings d that we experimentally explore are $< 6a$. Thus, pair interactions for our lattice can still be treated locally by the three dimensional hydrodynamic kernel, which we do in the next chapter. That said, the many-disk dynamics is inherently a 3D problem, but we can reduce it to effective 2D dynamics by making sure that the initial positions and the orientation vector of all the disks lie in the mid-plane of the quasi-two-dimensional geometry. Similar considerations arise in the context of pair-dynamics in the previous chapter, but unlike the two-body configuration, it is nearly impossible to manually fine-tune the initial configuration of multiple settling disks using needles. Pushing the disks out of the slots can lead to out-of-plane configurations which quickly destabilizes the array [see Figure 3.4]. We can prevent this by achieving nearly in-plane configurations, using a poking mechanism with a fork for each slot. At the release, each fork sits perfectly in the middle of its respective slot, leaving small clearances for air bubbles and to smoothen the relative motion between the teeth and the slots. The teeth of this poking mechanism are 3D printed using SLA resin and are thus delicate, and therefore it needs to be taken out of the slots gently. Breaking a few teeth can ruin the whole mechanism. We printed 8 separate

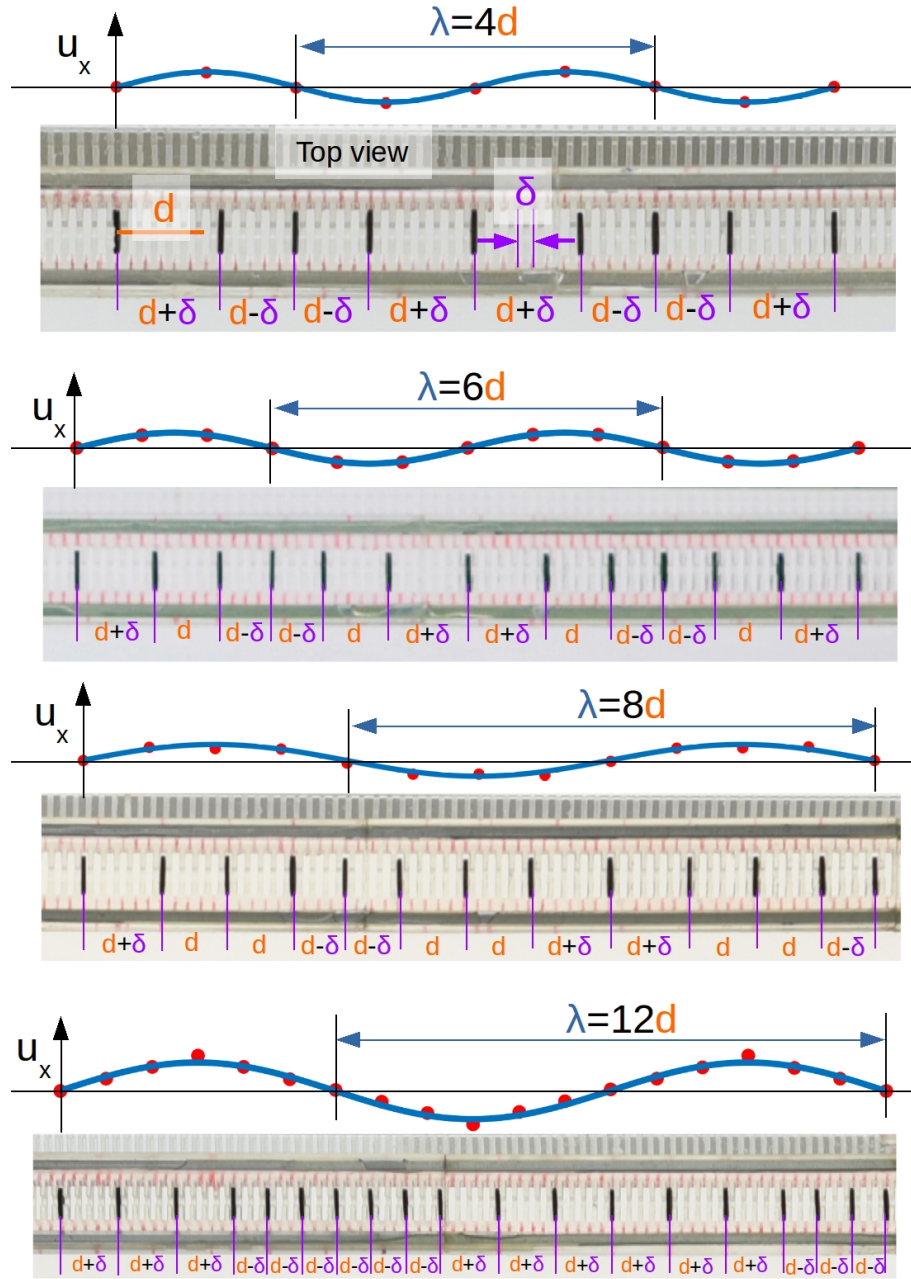


Figure 3.5: **Initial Perturbations:** Top view of the release mechanism shown before release, with the disks loaded in the slots. The centre-to-centre distance between adjacent slots is δ and the lattice spacing of the reference lattice is d . Initial horizontal positional perturbation u_x is shown by fitting a sine function (blue curve) to the measured perturbations (red dots) for the wavelengths $\lambda = 4d, 6d, 8d$ and $12d$.

release mechanisms, each 10 cm long, due to the size constraint of the 3D printer’s platform. The contact points of the printed parts were carefully cut, washed in isopropyl alcohol for 15 mins, UV-exposed for 30 mins, and sanded. The parts were then aligned and glued using Araldite. To prevent bending of the 80 cm long release mechanism under gravity, we machined metal slabs (0.5 cm \times 0.2 cm \times 85 cm) that pass through slots designed in the frame and the poking mechanism. The rigidity this imparts is crucial for the functioning of our mechanism that relies on perfect horizontal alignment of the frame and teeth. In order to prevent any sagging of the frame we additionally supported it with a hook in the middle. The ends of the metal slabs sit perfectly in the holders for the release mechanism, ensuring the mid-plane initial configuration. We take the disks out of the container using a basket crafted to sit nicely at the bottom, with long metal rods for pulling it up.

3.3 Initial perturbations

The reference state about which we perturb is an array of disks with uniform spacing achieved by choosing slots with separation d . On top of this initially uniform lattice, we impose horizontal positional perturbations $u_x(t = 0)$ at a wavenumber q by displacing disks appropriately to the right or left slot [see Figure 3.5].

The control parameters in experiments are the lattice spacing of the reference lattice and wavelength of the initial horizontal positional perturbation around this reference state. This was achieved using 3D-printed stacks of rectangular slots of width 0.125 cm and height 0.90 cm, into which disks of thickness 0.1 cm and diameter 0.8 cm are arranged in a periodic pattern as shown in the figure. We fit a sine wave on the horizontal perturbation u_x as a function of horizontal positions. The initial perturbations were measured to be sinusoidal with good accuracy, despite the discrete nature of the horizontal displacement. After arranging the disks across the total length of the release mechanism of 80 cm, the disks were poked out gently while the whole mechanism was submerged roughly 3 cm below the surface of the fluid, to avoid any bubbles. After the disks were released out of the slots, they were measured to have a random orientation error sitting on the imposed perturbation [see Fig(3.6)], as a result of the clearance of disks in the slots. This angular error corresponds to

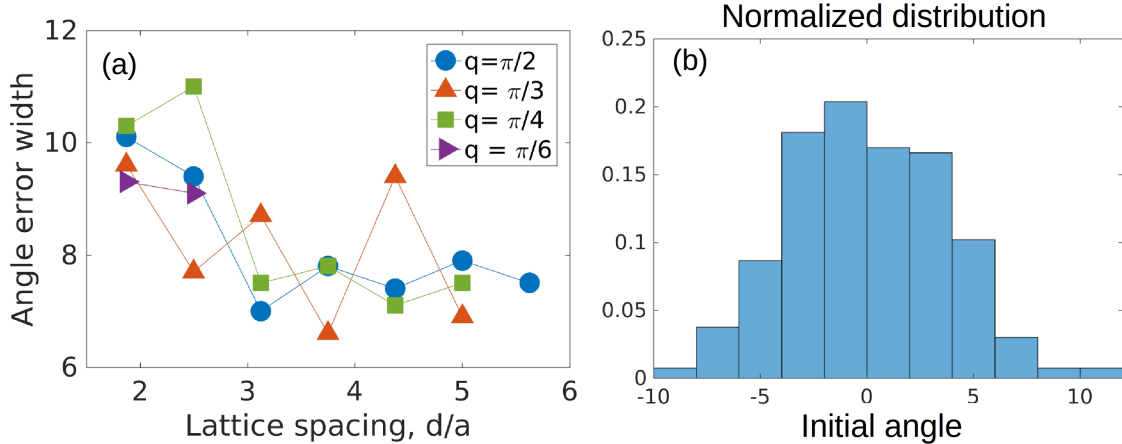


Figure 3.6: **Error in initial orientation:** (a) The error is quantified by $0.5 \times (\text{maximum} - \text{minimum})$ of the initial angles in any given run. This measure of the width in release angle is plotted here as a function of lattice spacing for $qd = \pi/2, \pi/3, \pi/4$ and $\pi/6$. (b) a combined distribution of, initial angles of several experimental runs for a fixed $qd = \pi/2$ and $d = 3.75a$.

an error in horizontal positional perturbation u_x of ± 0.03 cm. This error in release plays a crucial role in disrupting the lattice at late times.

3.4 Measurements

Images were taken at 1/3 frame per second using a Nikon D750 D-SLR camera. The positions and orientations of the disks were tracked by fitting ellipses to every disk for each image frame. The time-dependent amplitude of the positional and orientation perturbation (u_x, u_z, θ) was measured by fitting a sine wave to the measured particle displacements and orientations relative to the reference lattice in the co-moving frame. This choice of measurement is guided by previous theoretical work on drifting lattices, including Crowley’s theory, where the displacement field offers a natural dynamical variable. Also, the focus of the present work is to understand long-wavelength phenomena from local interparticle interactions, and the dynamics of (u_x, u_z, θ) captures the “microscopic” processes and collective behavior at the same time.

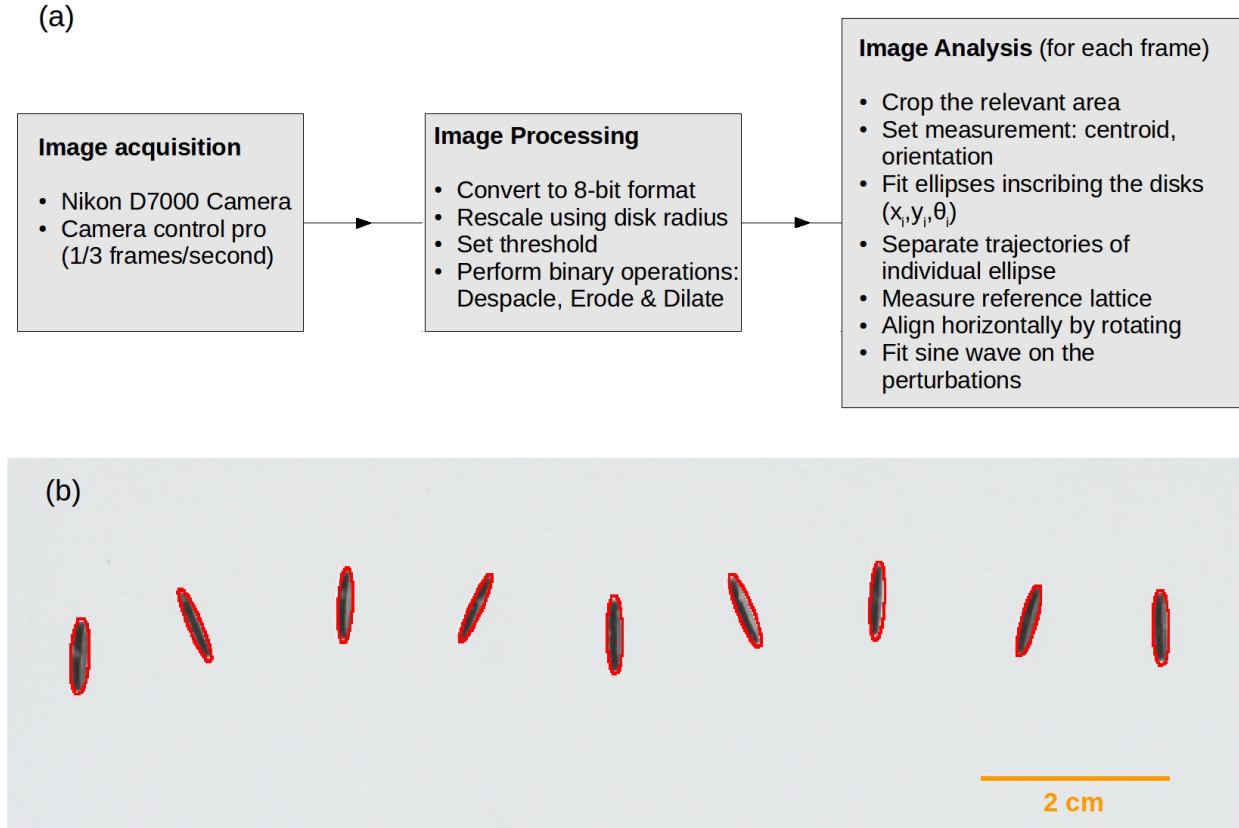


Figure 3.7: (a) Measurement workflow. Each set of processing and analysis is repeated for each frame. (b) Fitted ellipses in red inscribing disks colored black.

3.4.1 Image processing and analysis

The image frames were processed in ImageJ and analyzed in Matlab. The images were converted to 8-bit grayscale. The final image in which all disks had settled was used as a background image to perform background subtraction, and pixel distances were rescaled using the radius of the disks. This was followed by thresholding, giving a binary image. Any noise remaining after the subtraction was eliminated by the despeckle operation. Binary erode and dilate operations were done to smooth the boundaries of the disks. We set the measurements to fit ellipses inscribing the disks [see Figure 3.7 (b)]. The centroid and angle of the ellipse give the center positions and orientations of the disks respectively, with a precision of $0.02a$ and 0.5° . The errors in fitting ellipses were measured in a manner similar to that of the two-disk experiments [see Appendix 6.2]; they are measured by releasing an

isolated settling disk in a vertical orientation, and analysing the residuals of a linear fit on the $y - t$ and $\theta - t$ data. The slope of the $y - t$ data gives us the settling velocity 0.02782 ± 0.0001 cm/s, which is used to non-dimensionalize time while comparing to theory in the next chapter.

We get an array of positions and angles of all the ellipses, frame-by-frame. The ImageJ ellipse fitting does not tag the particles in adjacent frames, and the order of the particles keep changing across frames in the output data file. We write a Matlab code to track each ellipse across frames by using a distance minimization algorithm. To eliminate error due to camera angle – the data is rotated by measuring the tilt of initial lattice configuration by fitting a line in the (x_i, z_i) data, where i is the index for each ellipse [Figure 3.8 (a)].

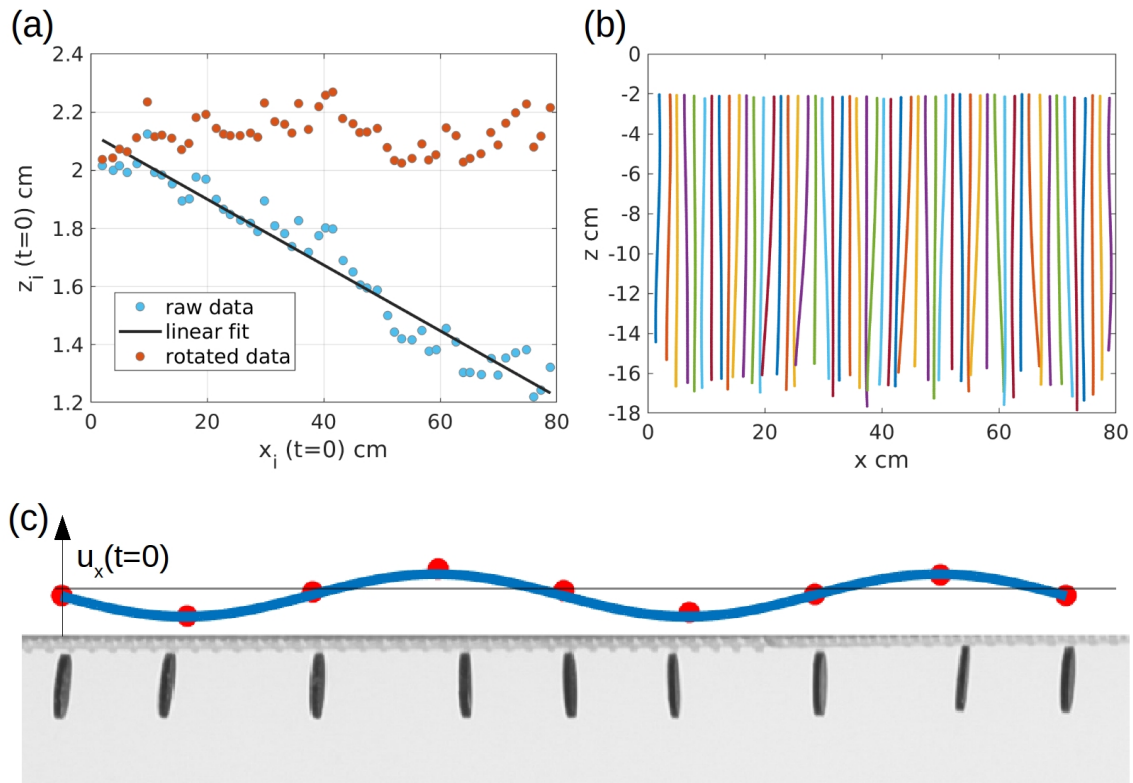


Figure 3.8: (a) Linear fitting on $x - z$ coordinates of all the disks at $t = 0$, to get the tilt error due to camera angle (blue), which is corrected by rotating the trajectories by this angle (red). (b) Separated trajectories of the disks shown in different colors. (c). Fitting a sine wave on the initial horizontal perturbation measured with respect to the reference lattice.

The data with the tracks separated [see Figure 3.8 (b)] are used to analyse the evolution of the perturbations (u_x, u_z, θ) . First, we calculate the lattice spacing of the reference lattice by measuring the largest node-to-node distance at $t = 0$ and dividing by $(N - 1)$, where N is the total number of particles. The reference lattice settles vertically with the mean settling speed of the lattice and the orientation and positional perturbations are measured for each disk with respect to this co-moving lattice. Similarly, orientations are measured as a function of horizontal positions in each frame.

A sine wave of the form $A \sin(q_0 x + \phi)$ is fitted to the $\delta\theta$, u_x and u_z perturbation with a specified initial wavenumber q_0 , giving the amplitudes A_θ , A_x and A_z respectively for each image frame [see Fig(3.9)], with some root mean square error. When modes are linearly stable, we mark a quarter of the time period when the $A_\theta(t)$ peaks, which roughly coincides with when $A_x(t)$ changes sign. The RMSE of fitting gives errors in measurement of the frequency of the wave-like modes.

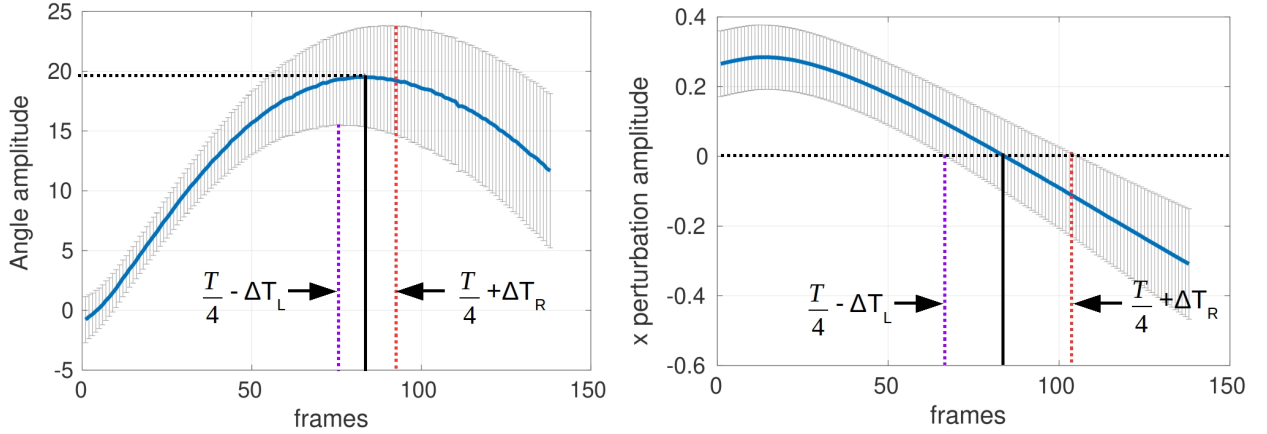


Figure 3.9: **Frequency measurement:** Amplitude of the fitted sine wave plotted for the angle and the horizontal positional perturbations, along with the residual error of the fit shown as vertical error-bars at each frame. At a quarter of the time period of the wave, the amplitude of the angle peaks and the horizontal perturbation crosses the $y = 0$ axis.

3.5 Two regimes of dynamics

As we vary lattice spacing, d , and perturbation wave-vector q , we experimentally observe two distinct regimes of dynamics, as depicted in Figure 3.11(b) and 3.12. The outcome of any given experiment is identified as being wave-like or clumping by considering the early stages of the time-dependence of the density autocorrelation $\langle \rho(t) \delta \rho(t=0) \rangle$, which is normalized such that it is 1 at $t=0$ [see Fig 3.10]. It is measured by taking the inner product of the particle number density $\rho(t) = \sum_{m=1}^N \delta(x - x_m(t))/N$ at time t , with the initial concentration fluctuation $\delta \rho(0, x) = -\partial u_x(t=0)/\partial x$ of the perturbed lattice. Here $x_m(t)$ is the position of the centre of mass of the m^{th} disk at time t , obtained by ellipse fitting. $\delta \rho(0, x)$ is obtained by fitting a sine to the initial horizontal displacement perturbation $u_x(t=0)$ [see Fig.3.8(c)] and shifting in phase by $\pi/2$. This approach of quantifying “screening” [29] is meaningful even in the non-linear regime. Alternatively, measuring the evolution of horizontal perturbations gives qualitatively the same answer, although with large errors in fitting sine waves at long times.

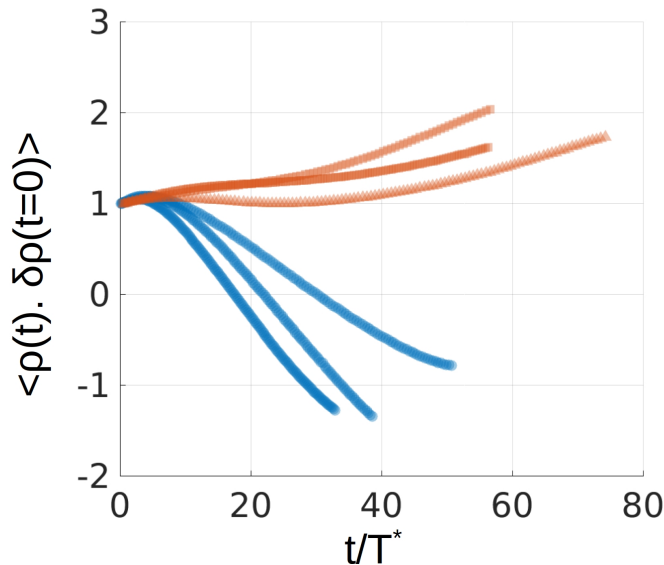


Figure 3.10: Density auto-correlation showing an escape from the Crowley instability for some initial conditions (blue). The time scale $T^* \equiv \mu d^2/F$, where $F = 32\mu a U_z^0/3$ [6], and $U_z^0 = 0.02782$ cm/s, is the experimentally measured velocity of an isolated settling disk in a vertical orientation.

3.5.1 Waves of orientation coupled with number density fluctuations

For the initial condition in Figure 3.11 (b), we see that the disks at the density nodes hardly rotate, while the orientation and position of disks at the antinodes vary sinusoidally with time [see figure 3.11].

Qualitatively, these wave dynamics may be explained by a composition of drag reduction, horizontal glide, and mutual rotation as discussed in Figure 3.1(d). Disks in regions of high number density fall faster than those in less dense regions due to reduced drag. The translational degree of freedom couples with rotations such that the disks in the dense region spread out due to orientational glide, stabilizing the lattice. This mechanism is characterized by a change in sign of the rotation of disks at the antinodal points, which leads to waves [see Supplementary Video 2.2]. These waves are eventually disrupted [see Supplementary video 2.3] due to amplification by the nonmodal growth mechanism of the experimental imprecision in the initial orientation [see Figure 3.6], which will be shown in the next chapter.

3.5.2 Clumping instability decorated with orientations

A different type of dynamics is observed for the initial conditions in Figure 3.12 where the perturbation quickly sharpens at the displacement nodes or the high-density regions. Just as in the Crowley instability of spheres, the dense regions fall faster due to reduced drag, and the vertical perturbation u_z increases. The orientation acts to spread out and rarefy the dense regions, but this effect is suppressed by the line of centers force leading to a clumping instability. The rotation of disks at the antinodes does not change sign, in contrast with the wave-like regime. In Figure 3.12 the horizontal perturbations grow to make the dense region more dense [see Supplementary video 2.4 & 2.5].

3.6 Conclusion

The many-body physics of collective sedimentation holds many challenges and provokes many debates [5, 28], which we must consider anew if we are to understand the role of internal

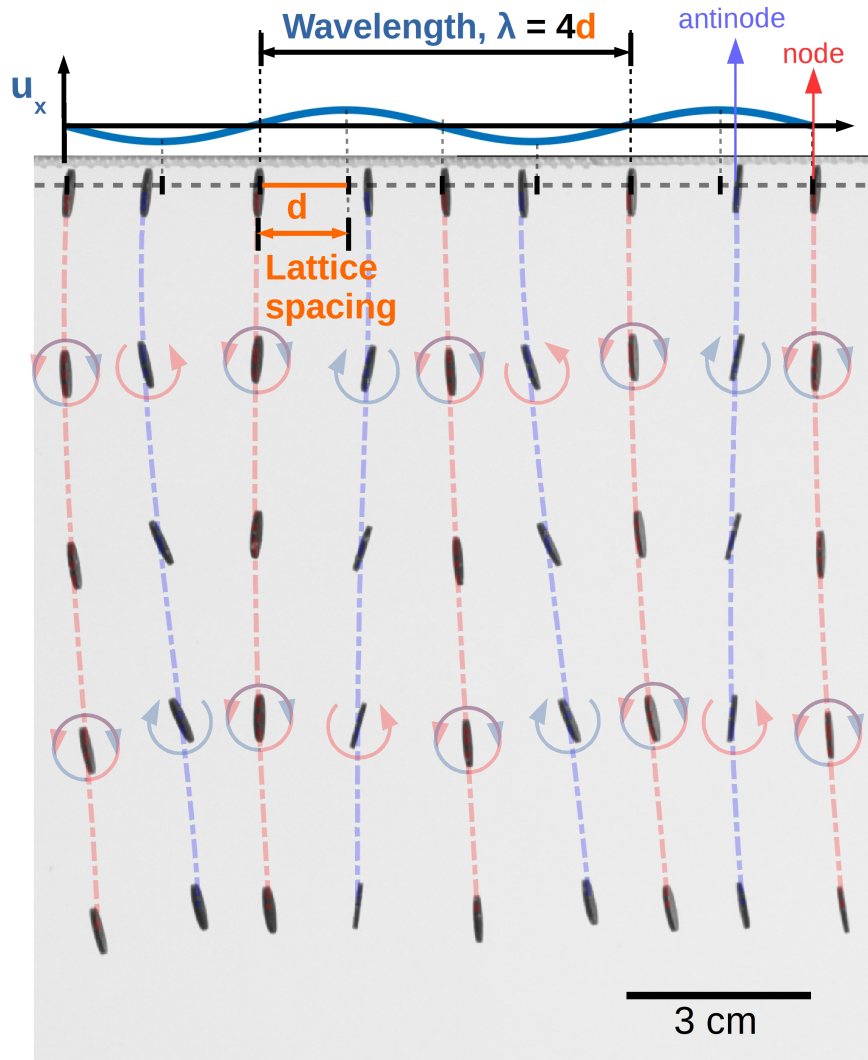


Figure 3.11: **Linearly stable mode:** Overlapped time frames shown for time, $t = 0, 130, 258, 386, 516$ seconds. The unperturbed lattice of initial conditions is shown in gray dashed lines. Horizontal positional perturbation, u_x is sinusoidal with wavelength $\lambda = 4d$ and lattice spacing of unperturbed state $d = 3.75a$ leads to undulations in orientation and vertical positions. The trajectories of disks at nodal and antinodal points are given by red and blue dashed lines respectively. The rotations of disk orientations in clockwise and anti-clockwise directions is given by blue and red circular arrows respectively. The sense of rotation changes along antinodal trajectories [see Supplementary video 2.2].

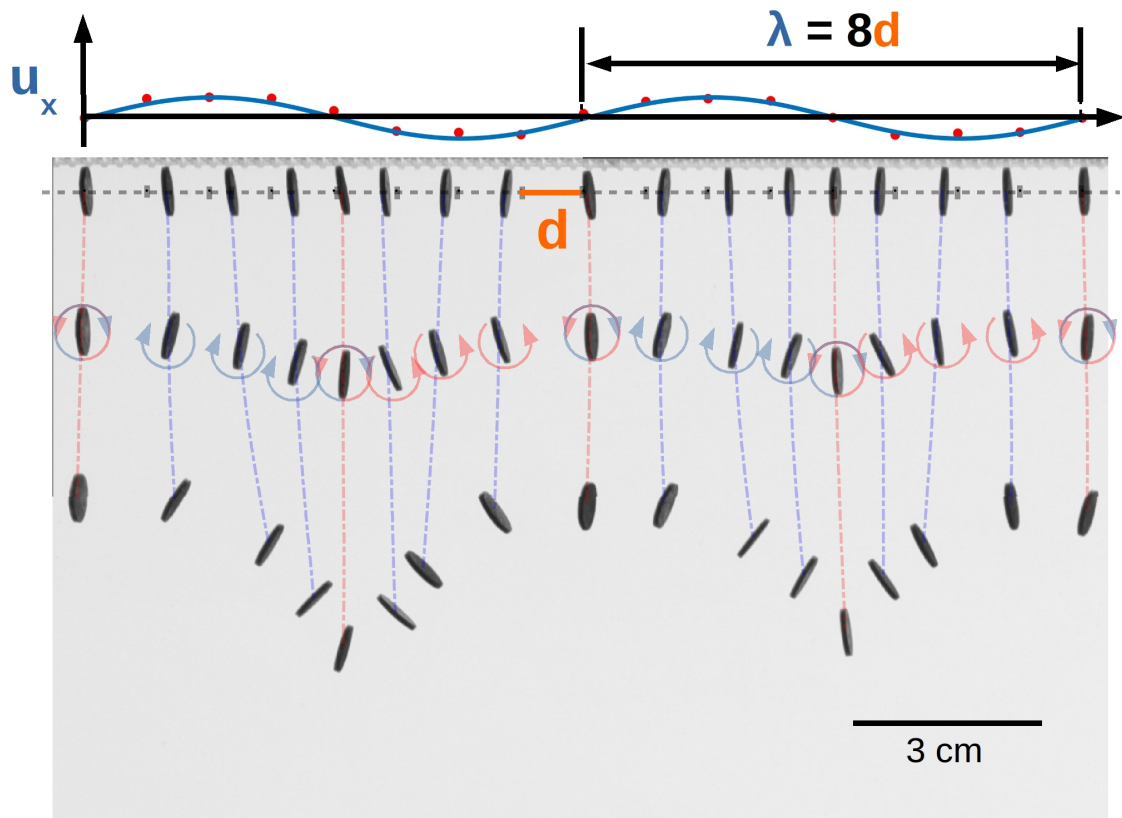


Figure 3.12: **Clumping instability:** Overlapped time frames shown for time, $t = 0, 120, 255$ seconds. For lattice spacing $d = 2.5a$ and initial perturbation wavenumber $qd = \pi/4$, the array exhibits instability, as line of centers force F^{LC} dominates over orientational drift F^θ . This leads to coarsening of the lattice followed by clumping in non-linear regime. The trajectories of disks at nodal points are given by red dashed lines. Clockwise and counterclockwise rotation of disks, depicted as blue and red circular arrows respectively, do not change colour along the trajectory of the disks, in contrast with the wave shown in Fig (3.11b) [see Supplementary videos 2.4 & 2.5].

degrees of freedom arising from particle shape. We study the role of particle orientation in the minimal setting of a one-dimensional lattice of Stokesian settling disks, and show the existence of two regimes of dynamical behavior, as a function of lattice spacing and perturbation wavenumber. One of these is an extension of Crowley’s clumping instability [51] to non-spherical particles. The second is a hitherto unknown state of orientation and displacement waves, where the drift and mutual interaction of the disks overcome the clumping instability. We thus identify an unexpected mechanism to resist instabilities that were iden-

tified for spheres fifty years ago [51], were elaborated into parallel ideas about spheroids in a landmark paper thirty years ago [39], and opened new directions in nonequilibrium statistical mechanics twenty years ago [53]. This competition between orientation and clumping in spheroids is related to an effect predicted for polar (self-aligning) particles [29] but our mechanism is crucially distinct from theirs due to different particle symmetries. In particular, orientation is not a slow variable for polar particles and thus does not enter in the “hydrodynamic” equations. In contrast, our disks rotate dynamically, thanks to apolarity and local inter-particle interactions in the form of a coupling (4.12) which arises from the antisymmetric part of the local fluid velocity gradient. The importance of these ingredients in our collective dynamics suggests a possible new consideration to be included in the statistical theory of Koch and Shaqfeh [39].

We will return to the experimental results in the next chapter, after we lay out the theoretical framework to rationalise our experimental findings.

Chapter 4

Theory of Sedimenting Spheroid Lattices: Waves & Algebraic Growth

This chapter is an elaboration of the theoretical results presented in R. Chajwa et al., Phys. Rev. X **10**, 041016 (2020). (©2020 American Physical Society) [Open Access link](#)

4.1 Introduction

In the previous chapter we experimentally demonstrated two dynamical regimes in settling disk arrays, and rationalised them heuristically. In this chapter we go beyond the qualitative explanation to offer a theoretical understanding at two levels. First, we place our experimental observations in the context of general continuum equations of motion for displacements and orientations of a sedimenting array of orientable particles, based only on symmetries and conservation laws. Second, to determine the phenomenological coefficients in these symmetry-based equations for Stokesian sedimentation, we construct the dynamical equations of the lattice using pairwise addition of forces and torques resulting from the hydrodynamic interactions.

Explicit construction of the dynamical equations of motion for Stokesian sedimenting spheroids, at the level of pair hydrodynamic interactions, determines the values of coefficients in our coarse-grained theory, and accounts for the experimentally observed instability boundary in the q - d plane. In the neutrally stable regime we find an emergent elasticity

which formally resembles that of a mass-and-spring chain, with the orientations of the disks playing the role of a momentum density field which is conserved when summed over the entire lattice.

It will be shown below that the mode structure of the linearised nearest-neighbour theory, in the limit of thin disks, compares remarkably well with the experimentally measured frequency ω of the waves, wherein $\omega \rightarrow 0$ as wavenumber $q \rightarrow 0$. This “hydrodynamic” character of the modes is a dual consequence of translation invariance along x as a result of which only the relative x positions of the disks matter, and the apolar character of the disks, as a result of which there is no restoring torque if all disks are rotated through the same angle, and so the sum of all the angles acts like a conserved total momentum.

We observe transient algebraic growth of perturbations in the linearly stable regime in our experiments, and in the numerical solution of the far-field equations. We term this growth “nonmodal” since it occurs even when all modes of the dynamical matrix are neutral or decaying [73, 75, 79, 81]. The underlying reason is that the dynamical matrix A is non-normal, i.e., $AA^\dagger \neq A^\dagger A$ (where the dagger represents the adjoint). Once the perturbation amplitude due to this nonmodal growth is large enough, nonlinearities can be triggered, disrupting the lattice through an unconventional route to instability at late times. Our calculations further predict the form of the initial perturbation that leads to maximum transient growth at each point in the neutrally stable regime in the q - d plane.

4.2 Broken-symmetry hydrodynamics

We construct the “hydrodynamic” [85] equations of motion of a drifting lattice of orientable objects, in the limit of no inertia, by writing the most general form of the mobility tensor (defined by velocity = mobility \times force) allowed by the symmetries of the system, to leading order in a gradient expansion, extending theories [53, 54] of the statistical dynamics of sedimenting crystals of pointlike objects. We find that the dynamical response of a lattice of orientable particles when perturbed about a suitable reference state contains terms that can compete with the clumping instability of isotropic particles [53, 51]. We discuss the structure of the resulting wavelike modes.

The configurations of a periodic lattice of uniaxial objects are characterized, in a coarse-grained Eulerian description, by the displacement field \mathbf{u} relative to the reference lattice and the orientation field \mathbf{K} defined by the mean local alignment of the particle axes. For our geometry [see Figure 4.1] $\mathbf{K} = (\cos \theta, 0, \sin \theta)$, with θ equivalent to $\theta + \pi$ because the particles are fore-aft symmetric. The equations of motion for \mathbf{u} and \mathbf{K} , in the presence of a gravitational driving force \mathbf{F} , must obey the following symmetries:

- Stokesian time-reversal symmetry under $t \rightarrow -t$ and $\mathbf{F} \rightarrow -\mathbf{F}$ [6]
- Translational invariance
- Rotational invariance in the subspace perpendicular to gravity
- Symmetry under inversion of orientations, $\mathbf{K} \rightarrow -\mathbf{K}$

The mobility cannot depend directly on \mathbf{u} due to translational invariance, but dependence on $\nabla \mathbf{u}$, \mathbf{K} and $\nabla \mathbf{K}$ is allowed:

$$\frac{\partial \mathbf{u}}{\partial t} = \mathbf{M}(\nabla \mathbf{u}, \mathbf{K}, \nabla \mathbf{K}) \cdot \mathbf{F}, \quad (4.1)$$

$$\frac{\partial \mathbf{K}}{\partial t} = \mathbf{P} \cdot \mathbf{N}(\nabla \mathbf{u}, \mathbf{K}, \nabla \mathbf{K}) \cdot \mathbf{F}, \quad (4.2)$$

where \mathbf{M} and \mathbf{N} are the translational and rotational mobilities respectively, and $\mathbf{P} \equiv \mathbf{I} - \mathbf{K}\mathbf{K}$ is the projector transverse to the unit vector \mathbf{K} .

The gradient expansion of the translational mobility $\mathbf{M}(\nabla \mathbf{u}, \mathbf{K}, \nabla \mathbf{K})$ and rotational mobility $\mathbf{N}(\nabla \mathbf{u}, \mathbf{K}, \nabla \mathbf{K})$, to leading orders in gradients gives

$$\mathbf{M} = \mathbf{M}_0 + \mathbf{M}_1 \nabla \mathbf{u} + m_2 \mathbf{K}\mathbf{K} + \mathcal{O}(\nabla \nabla \mathbf{u}) + \mathcal{O}(\nabla \nabla \mathbf{K}) \quad (4.3)$$

$$\begin{aligned} \mathbf{P} \cdot \mathbf{N} = & n_1 \boldsymbol{\epsilon} \cdot \mathbf{K} \cdot (\boldsymbol{\epsilon} \cdot \nabla \nabla \cdot \mathbf{u}) + n_2 \mathbf{P} \cdot \mathbf{K} \nabla \nabla \cdot \mathbf{u} \\ & + n_3 \mathbf{P} \cdot \nabla \mathbf{K} + \mathcal{O}(\nabla \mathbf{u} \nabla \mathbf{u}) + \mathcal{O}(\nabla \nabla \mathbf{K}) \end{aligned} \quad (4.4)$$

In the first term of (4.4), $\boldsymbol{\epsilon}$ is the Levi-Civita tensor. Retaining only those terms that are allowed by the symmetries leads to the ‘‘hydrodynamic’’ equations for the displacement

field \mathbf{u} and orientation field \mathbf{K} in one dimension x by dropping z derivatives (4.5) - (4.7). This leads at lowest order in gradients, in a comoving frame, to

$$\frac{\partial u_x}{\partial t} = \lambda_1 \frac{\partial u_z}{\partial x} + \alpha K_x K_z, \quad (4.5)$$

$$\frac{\partial u_z}{\partial t} = \lambda_2 \frac{\partial u_x}{\partial x} + \beta K_z^2, \quad (4.6)$$

$$\frac{\partial K_z}{\partial t} = \gamma K_x \frac{\partial^2 u_x}{\partial x^2}. \quad (4.7)$$

Here, λ_i , α and γ depend on \mathbf{F} and the parameters governing the mobilities in (4.1) and (4.2). Note: equations (4.5) - (4.7) contain only hydrodynamic couplings proportional to the gravitational driving force, and our gradient expansion incorporates only local interparticle interactions. We have not included interactions arising from interparticle potentials or entropy. These enter at next order in gradients, and break Stokesian time-reversibility [7].

Substituting $\mathbf{K} = (\cos \theta, 0, \sin \theta)$ in (4.5)-(4.7) and linearizing about $\theta = 0$, the state where the particle axes are along x (Fig. 3.11a) leads, for disturbances with frequency ω and wavenumber q , to the dispersion relations

$$\omega_0 = 0, \quad \omega_{\pm} = \pm q_x \sqrt{\lambda_1 \lambda_2 + \alpha \gamma} \quad (4.8)$$

with elasticity contributing to (4.7) and (4.8) at order q^2 . For $\alpha \rightarrow 0$ the linearized equations for the translational degrees of freedom (u_x, u_z) are independent of \mathbf{K} and reduce to those of the Lahiri-Ramaswamy model [53], with wavelike modes or an instability depending on the sign of $\lambda_1 \lambda_2$ [53, 54, 55]. \mathbf{u} affects \mathbf{K} through the one-way coupling governed by γ . For $\alpha \neq 0$, translation and rotation are coupled, and the presence of $\alpha \gamma$ in the dispersion relation opens up the possibility of linearly stable wavelike dynamics even for $\lambda_1 \lambda_2 < 0$. The linearized dynamics about the state where \mathbf{K} is vertical corresponds to changing the sign of α in (4.8). For a system of sedimenting particles this means that the array is stable either with horizontal orientations or vertical orientations, but not both. Similar considerations arise in principle for the stability and dynamics [55] of driven flux lattices in thin slabs of type-II superconductors if the cross-sections of the flux lines are non-circular.

4.3 “Microscopic” ingredients : pair hydrodynamic interactions

We now go beyond symmetry considerations, and explicitly construct the equations of motion for a settling lattice based on single-particle motion and addition of pairwise forces and torques at each particle position. We develop the theory for an array of spheroids, of eccentricity $e = \sqrt{1 - b^2/a^2}$, where a and b are the semi-major and semi-minor axes respectively. In the limit of $e \rightarrow 1$, an oblate spheroid approaches a disk shape, as in our experiments. We consider hydrodynamic interactions to leading order in a/r , where r is the separation between two particles. The ingredients of array dynamics are: (i) Lateral drift of a single particle – An isolated settling spheroid cannot rotate, thanks to Stokesian time-reversal symmetry, but drifts horizontally with velocity

$$U_x^0 = \frac{F\alpha(e)}{12\pi\mu a} \sin 2\theta \quad (4.9)$$

[6, 32] where F is its buoyant weight, μ is the dynamic viscosity of the fluid and the mobility α is a function of eccentricity. Figure 4.1 shows a schematic of a portion of our array, in which the orientation vector K^n of the n^{th} particle is defined as a unit vector along the minor (major) axis for an oblate (prolate) spheroid. The angle θ^n is measured from the vertical as shown. (ii) Mutual drag reduction – Two particles at finite separation fall faster than an isolated one, due to the addition of the flow fields generated by each Stokes monopole [6, 51]. In the far-field approximation, the increased vertical velocity to leading order in a/r is

$$U_z = -\frac{F}{6\pi\mu a} \frac{3a}{4r} \left[1 + \frac{(z_1 - z_2)^2}{r^2} \right]. \quad (4.10)$$

(iii) Horizontal drift – The flow generated by the neighbouring particle gives rise to a force along the line joining the centers of the two particles [6, 51], which leads to a horizontal component of velocity

$$U_x = -\frac{F}{6\pi\mu a} \frac{3a}{4r^3} (x_1 - x_2)(z_1 - z_2) \quad (4.11)$$

to leading order in a/r .

(iv) Mutual rotational coupling – The presence of a neighbouring particle generates a

velocity field of non-zero vorticity, which to leading order in a/r gives a rotation

$$\dot{\theta} = F \frac{x_1 - x_2}{8\pi\mu r^3}. \quad (4.12)$$

We proceed by combining ingredients (i) to (iv) to build the dynamics of the array of spheroids.

4.4 A hidden Hamiltonian sector: monoatomic chain of masses-and-springs

We consider an infinite one-dimensional reference lattice along the x -axis of uniformly spaced lattice points with spacing d and falling in the $-z$ direction. As shown in Figure 4.1, we consider identical spheroids with orientation θ^n , and centroids at a small displacement (u_x^n, u_z^n) measured from each lattice point, where the superscript n stands for the n^{th} particle. In the mean settling frame, pairwise addition of forces and torques on the n^{th} particle due to hydrodynamic interactions with the $(n+l)^{\text{th}}$ and $(n-l)^{\text{th}}$ particles, for $l = 1, 2, 3, \dots, \infty$, gives the equation of motion of the n^{th} particle as

$$\frac{du_x^n}{dt} = -\frac{3a^2}{4d^2} \sum_{l=1}^{\infty} \frac{u_z^{n+l} - u_z^{n-l}}{l^2} + \frac{\alpha(e)}{2} \sin 2\theta^n, \quad (4.13)$$

$$\frac{du_z^n}{dt} = +\frac{3a^2}{4d^2} \sum_{l=1}^{\infty} \frac{u_x^{n+l} - u_x^{n-l}}{l^2} + \alpha(e) \sin^2 \theta^n, \quad (4.14)$$

$$\frac{d\theta^n}{dt} = \frac{3a^3}{2d^3} \sum_{l=1}^{\infty} \frac{u_x^{n+l} + u_x^{n-l} - 2u_x^n}{l^3}. \quad (4.15)$$

We have non-dimensionalised the lengths and times using the semi-major axis a and the timescale $6\pi\mu a^2/F$ respectively, so that velocities are scaled by $F/6\pi\mu a$, the Stokes settling speed in the spherical limit. To understand the dynamics, it is instructive to first artificially set $u_z^n = 0$ for all n in (4.13) and (4.15). Doing this reveals that a sector of the dynamics can be written in terms of the canonically conjugate variables (u_x^n, θ^n) as

$$\dot{u}_x^n = \frac{\partial H}{\partial \theta^n}, \quad \dot{\theta}^n = -\frac{\partial H}{\partial u_x^n} \quad (4.16)$$

with an effective Hamiltonian

$$H = \frac{\alpha(e)}{4} \sum_m (1 - \cos 2\theta^m) + \frac{3a^3}{4d^3} \sum_{l,m} \frac{(u_x^m - u_x^{m+l})^2}{l^3}. \quad (4.17)$$

The reduced dynamics under (4.16) and (4.17) conserves both H and the total “momentum” $\sum_n \theta^n$. This Hamiltonian sector of the dynamics of our system extends the treatment of [61] to an array of disks. Effective Hamiltonians for Stokesian systems have also been presented for a swimmer in channel flow [67, 68], the pair dynamics of bottom-heavy swimmers [69] – formally similar to [61], and, farther afield, driven rotor suspensions [71, 131].

In the quasi two-dimensional geometry of our experiments, bounded by closely spaced walls, truncating the interparticle hydrodynamic interaction at nearest neighbours so that particle n interacts only with particles $n \pm 1$, as in the treatment in [51], should be a good approximation. The Hamiltonian dynamics (4.16), (4.17) of the settling array for $u_z = 0$, for small θ^n , becomes formally identical to that of the displacement and momentum-density fields respectively of a momentum-conserving monatomic mass-and-spring lattice. For fixed F the equations of motion are invariant under $t \rightarrow -t$, $u_x^n \rightarrow u_x^n$, $\theta^n \rightarrow -\theta^n$, $u_z^n \rightarrow -u_z^n$. A term in (4.15) of the form $\theta^{n+1} + \theta^{n-1} - 2\theta^n$, which within our analogy amounts to a momentum-conserving viscous damping, can arise if inter-disk entropic or energetic aligning interactions, which break Stokesian time-reversal invariance, are taken into account. We do not pursue this issue further here except to note that within a linear stability analysis such a term would turn a neutral regime into a stable one.

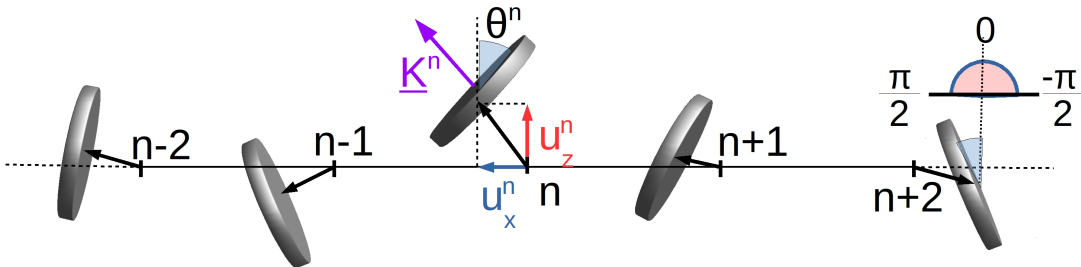


Figure 4.1: **Discrete dynamical picture:** A schematic of the array of disks showing spatial perturbations (u_x^n, u_z^n) and orientation perturbation θ^n of the n^{th} disk which interacts hydrodynamically with the neighbours $n - i$, $i = 1, 2, \dots$. For prolate spheroids the orientation vector \mathbf{K}^n is rotated by $\pi/2$ from the one shown.

4.5 Wavelike modes and clumping instability

Perturbing the angle about zero, $\theta = 0 + \delta\theta$, linearising the equations and Fourier transforming with respect to n gives the equation $\dot{\mathbf{X}}_q = \mathbf{A}(q)\mathbf{X}_q$, where $\mathbf{X}_q = (u_q^x, u_q^z, \delta\theta_q)$ is the spatial fourier transform of the perturbations with wavenumber q along x , with dynamical matrix

$$\mathbf{A}(q) = \begin{pmatrix} 0 & -(3ia^2/2d^2) \sin q & \alpha(e) \\ +(3ia^2/2d^2) \sin q & 0 & 0 \\ -(6a^3/d^3) \sin^2 q/2 & 0 & 0 \end{pmatrix} \quad (4.18)$$

which is singular because in the linear approximation the dynamics of both u_q^z and $\delta\theta_q$ depend only on u_q^x . In section 4.6 we will use the mass-and-spring analogy to define a natural inner product with respect to which we will show that $\mathbf{A}(q)$ is nonnormal, with physical consequences that we will discuss in detail. Our treatment will be in the nearest-neighbour approximation but the feature of non-normality can be seen to hold without this truncation. For now, we substitute the translational mobility function [12, 34, 32] for oblate spheroids: $\alpha(e) = [(9 - 6e^2) \tan^{-1}(e/\sqrt{1 - e^2}) - 9e\sqrt{1 - e^2}]/8e^3$, and for prolate spheroids: $\alpha(e) = \{(9 - 3e^2) \ln[(e + 1)/(1 - e)] - 18e\}/16e^3$, which gives the mode structure with two branches around $\omega = 0$ for each,

Oblate Spheroids:

$$i\omega_{\pm}(q) = \pm \left| \sin \frac{q}{2} \right| \sqrt{\frac{3a^3}{4d^3e^3} (6e^2 - 9) \tan^{-1} \left(\frac{e}{\sqrt{1 - e^2}} \right) + \frac{27a^3}{4d^3e^2} \sqrt{1 - e^2} + \frac{9a^4}{2d^4} (1 + \cos q)}, \quad (4.19)$$

Prolate Spheroids:

$$i\omega_{\pm}(q, e) = \pm \left| \sin \frac{q}{2} \right| \sqrt{\frac{3a^3}{8d^3e^3} (3e^2 - 9) \ln \left(\frac{1 + e}{1 - e} \right) + \frac{27a^3}{4d^3e^2} + \frac{9a^4}{2d^4} (1 + \cos q)}. \quad (4.20)$$

In the limit of $e \rightarrow 0$, the dispersion relations for both oblate (4.19) and prolate (4.20) spheroids converges to $i\omega_{\pm} = \pm(3a^2/2d^2)|\sin(q)|$, which is just the Crowley instability for

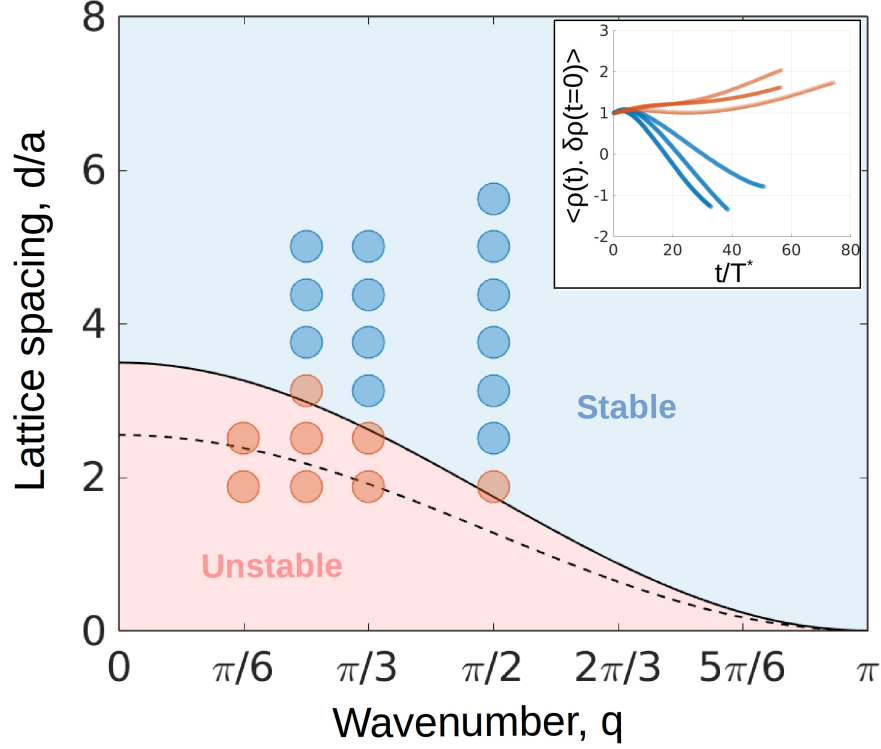


Figure 4.2: **Phase diagram:** The phase diagram with the stable regime shown in blue and unstable regime in red. The experimental data points (circles) are coloured blue or red by measuring whether the density autocorrelation grows or decays, which is shown in the inset on the top right, for some representative stable (blue) and unstable (red) points in the $q - d$ plane, where time scale $T^* = \mu d^2 / F$. The phase boundary predicted by the linear theory with nearest-neighbour interaction is shown for oblate spheroids with eccentricity approximating the experimental thickness, $e = 0.9922$ (solid line) and spheroid of zero thickness $e = 1$ (dashed line).

spheres [51]. For $e \neq 0$, defining the nondimensional quantity $\tilde{d} \equiv 2d\alpha(e)/3a$, gives a universal condition for stability:

$$\tilde{d} \geq \cos^2 \frac{q}{2}, \quad (4.21)$$

so that $\tilde{d} = \cos^2 q/2$ defines the stability boundary in the $\tilde{d}-q$ plane, separating the regime of kinematic waves (blue) from the clumping instability (red) as shown in the phase diagram of Figure 4.2. In general, for a uniaxial apolar shape, α is a constant parameter [6] which can be determined by experimentally measuring the lateral drift of an isolated settling object. From (4.18) it follows that our expression for the stability boundary (4.21) applies to all

axisymmetric apolar shapes, when d is rescaled by $2\alpha/3a$.

This prediction agrees well with our experimental data shown by the red and blue circles, where we have initialised the lattice at those points in the d - q plane. The density auto-correlation is shown in the inset to Figure 4.2, where some curves increase in amplitude, and others decay, as discussed in the previous chapter. At later times, even in the wave-like regime, the perturbation becomes very non-sinusoidal, as nonlinear effects become prominent.

More specifically, the limit of disks with zero thickness ($e \rightarrow 1$ for oblate spheroids), produces the mode structure shown in Figure 4.3(a) :

$$i\omega_{\pm}(q) = \pm \frac{3a^2}{2d^2} \left| \sin \frac{q}{2} \right| \sqrt{\left(-\frac{d\pi}{2a} + 4 \cos^2 \frac{q}{2} \right)}, \quad (4.22)$$

which produces neutrally stable modes when the lattice spacing $d > 8a \cos^2(q/2)/\pi$ and clumping instability otherwise. This prediction is compared with experimental data for the frequency in Figure 4.3(b) for various q and d . We show solutions corresponding both to zero thickness, as well as for the ellipsoid with $2a$ and $2b$ corresponding to the diameter and thickness of our disks. In the long wavelength limit $q \rightarrow 0$, (4.22) reduces to the dispersion relation (4.8) predicted using symmetry arguments in the previous section. The phenomenological coefficients in the equations (4.5)-(4.7) are thus determined for disks to be: $\lambda_1\lambda_2 = -9a^4/4d^4$ and $\alpha\gamma = 9\pi a^3/32d^3$.

The limit for needles of zero thickness (prolate spheroids with $e \rightarrow 1$) is not well defined, but the dispersion relation for rods of small thickness $2b$ and length $2a$, to leading order in $1 - e$ is:

$$i\omega_{\pm}(q) = \pm \frac{3a^2}{2d^2} \left| \sin \frac{q}{2} \right| \sqrt{\left(\frac{3d}{a} - \frac{2d}{a} \ln \left(\frac{2a}{b} \right) + 2 \cos^2 \frac{q}{2} \right)}. \quad (4.23)$$

Note that the gapless feature ($\omega \rightarrow 0$ as $q \rightarrow 0$) of the modes (4.19) - (4.20) is tied to the conservation of total ‘‘momentum’’ $\sum_n \theta^n$ and the breaking of continuous translational symmetry by the lattice. Although the lattice was not formed by a phase transition to an ordered state, our imposition of an array structure on a translation-invariant background means that only the relative positions of disks matter, so the displacement field behaves like a true broken-symmetry mode [85].

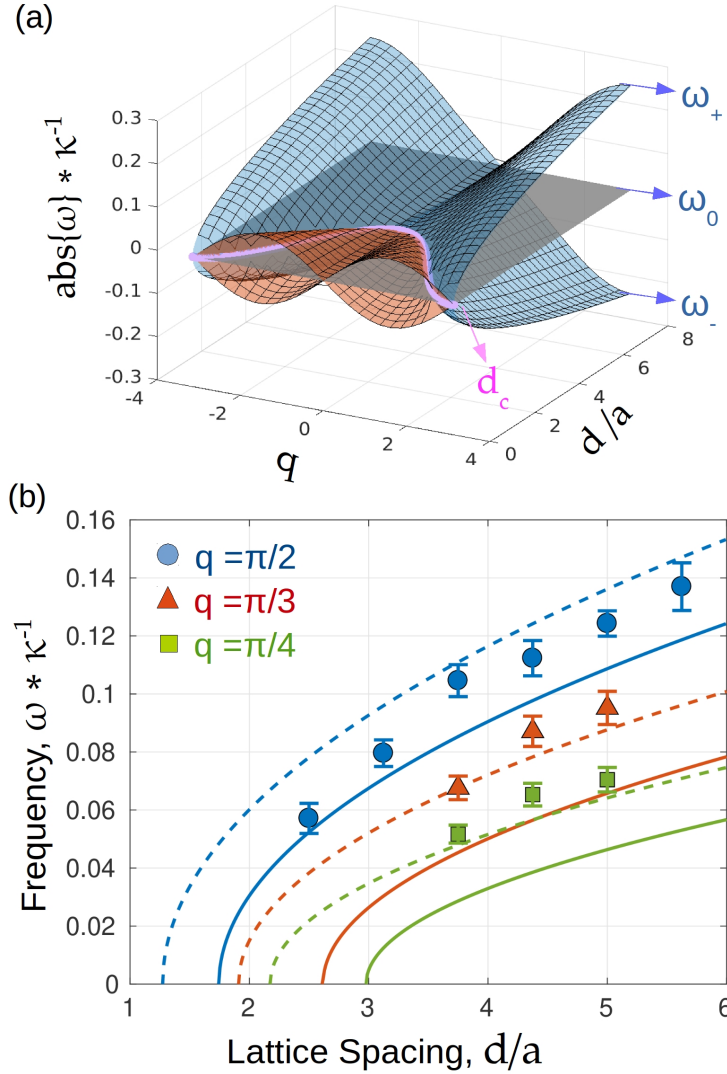


Figure 4.3: **Spectrum:** (a) The branches of the spectrum. The absolute value of the complex frequency scaled by $\kappa = 6\pi a^2/d^2$ is shown as a function of the nondimensional wavenumber q and spacing d . The blue surface is for purely real frequencies (the neutrally stable modes) and the red surface is for purely imaginary frequencies (clumping instability). The boundary between the stable and unstable regimes is shown by the magenta curve d_c . (b) Measured non-dimensional frequency $\omega * \kappa^{-1}$ (symbols) for various wavenumbers q plotted against the lattice spacing d/a . The curves are predicted by our nearest-neighbour theory for oblate spheroids, solid lines for the experimental eccentricity $e = 0.9922$ and dashed lines for the limit of zero thickness $e = 1$.

4.5.1 Far-field simulations with periodic boundaries

To understand the non-linear dynamics of disks in (x, z) plane, we numerically analyse the equations of motion for spheroids in the limiting case of disks $e \rightarrow 1$, to leading order in $\mathcal{O}(a/r)$, by pairwise addition of hydrodynamic interactions using the method of reflections [34]. When lengths are non-dimensionalized by a and time by $6\pi\mu a^2/F$, such that velocities are scaled by the settling speed of an isolated sphere, the far-field equations for the positions (x_n, z_n) and orientations θ_n of the n^{th} spheroid become:

$$\frac{dx_n}{dt} = \frac{3\pi}{32} \sin 2\theta_n - \sum_{m \neq n}^N \frac{3(x_n - x_m)(z_n - z_m)}{4r_{mn}^3} \quad (4.24)$$

$$\frac{dz_n}{dt} = \frac{3\pi}{16} (\sin^2 \theta_n - 3) - \sum_{m \neq n}^N \frac{3}{4} \left[\frac{1}{r_{mn}} + \frac{(z_n - z_m)^2}{r_{mn}^3} \right] \quad (4.25)$$

$$\begin{aligned} \frac{d\theta_n}{dt} = & \sum_{m \neq n}^N \frac{3(x_n - x_m)}{4r_{mn}^3} \\ & - \sum_{m \neq n}^N \frac{9(z_n - z_m)}{4r_{mn}^5} [(x_n - x_m) \cos \theta_n + (z_n - z_m) \sin \theta_n] \times \\ & [(z_n - z_m) \cos \theta_n - (x_n - x_m) \sin \theta_n] \end{aligned} \quad (4.26)$$

We numerically solve the above equations using the fourth order Runge-Kutta method. In the nearest-neighbour approximation, the number of interacting neighbours N truncates the spatial summation over m , making implementation of periodic boundaries straightforward. Equations (4.24)-(4.26) are for initial conditions in which the orientation vector of all the disks lie in the (x, z) plane and hence the resulting trajectories are confined to the same plane $y = 0$. Although we use (4.24)-(4.26) to investigate lattice configurations, these equations can be used to study the in-plane dynamics of any reference structure. Note that, when the interparticle separation r_{mn} between a pair approaches 0, the far-field numerics fails to capture the dynamics. This can be seen to happen in the pair configurations of the form “ \perp ” [see Supplementary video 2.7].

4.6 Non-normality and the transient algebraic growth of wavelike modes

We show below that the dynamical matrix $\mathbf{A}(q)$ of (4.18) is non-normal with respect to a natural inner product. This feature can [75, 81] – and in the present case does – lead to short-time behaviour quite different from what one might expect naïvely from the exponential evolution of the eigenmodes. In particular, even when all the eigenvalues show negative or zero growth rate, disturbances can grow algebraically even in the linear regime for some time [79]. The amount of growth depends both on the operator and on the configuration of the initial perturbation. For small growth, the system will relax at large times to the behaviour expected from the least stable eigenmode. When the transient growth is significant and if the initial perturbation amplitude is large enough, however, the system is ultimately pushed into the nonlinear regime. In hydrodynamic stability problems, especially in shear flows [86], transition to turbulence through the algebraic growth route is quite common. However, experimental quantification of algebraic growth is extremely difficult. The present work offers a rare quantitative comparison of transient growth in theory and experiment.

For disks, the eigenfunctions of the dynamical matrix (4.18) can be used to construct the solution for experimental initial conditions. The eigenvectors corresponding to the eigenvalues $(0, i\omega_-, i\omega_+)$ defined in (4.22), are respectively given by the columns of the matrix

$$\begin{pmatrix} 0 & i\omega\pi \csc^2\left(\frac{q}{2}\right) & -i\omega\pi \csc^2\left(\frac{q}{2}\right) \\ -i\frac{d\pi}{8a} \csc(q) & -\frac{1}{2}i \cot\left(\frac{q}{2}\right) & -\frac{1}{2}i \cot\left(\frac{q}{2}\right) \\ 1 & 1 & 1 \end{pmatrix}. \quad (4.27)$$

4.6.1 Wave solution for spheroids

The eigenfunctions corresponding to the eigenvalues $(\lambda_1, \lambda_2, \lambda_3) = (0, -i\omega, i\omega)$, where $\omega \equiv \omega_+$ is form (4.19)- (4.20), are given by \mathbf{v}_1 , \mathbf{v}_2 and \mathbf{v}_3 respectively

$$\mathbf{v}_1 = \begin{pmatrix} 0 \\ -i\frac{2d\pi\alpha(e)}{3a} \csc(q) \\ 1 \end{pmatrix}, \mathbf{v}_2 = \begin{pmatrix} i\omega\pi \csc^2\left(\frac{q}{2}\right) \\ -\frac{1}{2}i \cot\left(\frac{q}{2}\right) \\ 1 \end{pmatrix}$$

$$\mathbf{v}_3 = \begin{pmatrix} -i\omega\pi \csc^2\left(\frac{q}{2}\right) \\ -\frac{1}{2}i \cot\left(\frac{q}{2}\right) \\ 1 \end{pmatrix} \quad (4.28)$$

giving the solution as a real part

$$\mathbf{X}(t) = \sum_{i=1}^3 \frac{a_i}{2} (\mathbf{v}_i e^{iqn} e^{\lambda_i t} + \mathbf{v}_i^* e^{-iqn} e^{\lambda_i^* t}) \quad (4.29)$$

here $\mathbf{X}^n = (u_x^n, u_z^n, \delta\theta_q^n)^\top$. For $\mathbf{A} \equiv (a_1, a_2, a_3)$, (4.29) becomes $\mathbf{X}^n(t) = \mathbf{B} \cdot \mathbf{A}$, where in the stable regime

$$\mathbf{B} = \begin{pmatrix} 0 & -\omega\pi \csc^2\left(\frac{q}{2}\right) \sin(qn - \omega t) & \omega\pi \csc^2\left(\frac{q}{2}\right) \sin(qn + \omega t) \\ \frac{2d\pi\alpha(e)}{3a} \csc(q) \sin(qn) & \frac{1}{2} \cot\left(\frac{q}{2}\right) \sin(qn - \omega t) & \frac{1}{2} \cot\left(\frac{q}{2}\right) \sin(qn + \omega t) \\ \cos(qn) & \cos(qn - \omega t) & \cos(qn + \omega t) \end{pmatrix} \quad (4.30)$$

The coefficients \mathbf{A} can be determined from the initial condition, $\mathbf{A} = \mathbf{B}^{-1} \cdot \mathbf{X}^n|_{t=0}$. Our experimental initial condition is $\mathbf{X}^n(t=0) = (\epsilon \sin(qn), 0, 0)^\top$, making $\mathbf{A} = \frac{\epsilon \sin^2(q/2)}{2\omega\pi} (0, -1, 1)^\top$, which gives the wave solution in stable regime

$$u_x^n(t) = \epsilon \sin(qn) \cos(\omega t) \quad (4.31)$$

$$u_z^n(t) = \frac{\epsilon \sin(q)}{4\omega\pi} \cos(qn) \sin(\omega t) \quad (4.32)$$

$$\delta\theta^n(t) = -\frac{\epsilon \sin^2(q/2)}{\omega\pi} \sin(qn) \sin(\omega t) \quad (4.33)$$

Note that the dependence on eccentricity of the spheroids enters through ω from (4.19) & (4.20). In the unstable regime the eigenvalues $(0, -\lambda, +\lambda)$ are real, giving hyperbolic functions in the time dependence of the solution

$$u_x^n(t) = \epsilon \sin(qn) \cosh(\lambda t) \quad (4.34)$$

$$u_z^n(t) = \frac{\epsilon \sin(q)}{4\lambda\pi} \cos(qn) \sinh(\lambda t) \quad (4.35)$$

$$\delta\theta^n(t) = -\frac{\epsilon \sin^2(q/2)}{\lambda\pi} \sin(qn) \sinh(\lambda t) \quad (4.36)$$

The time-dependence predicted here is in good agreement with the experimental data shown in Figure 4.4 (a) for $q = \pi/2$ and $d/a = 3.75$. This result is also compared to the numerical

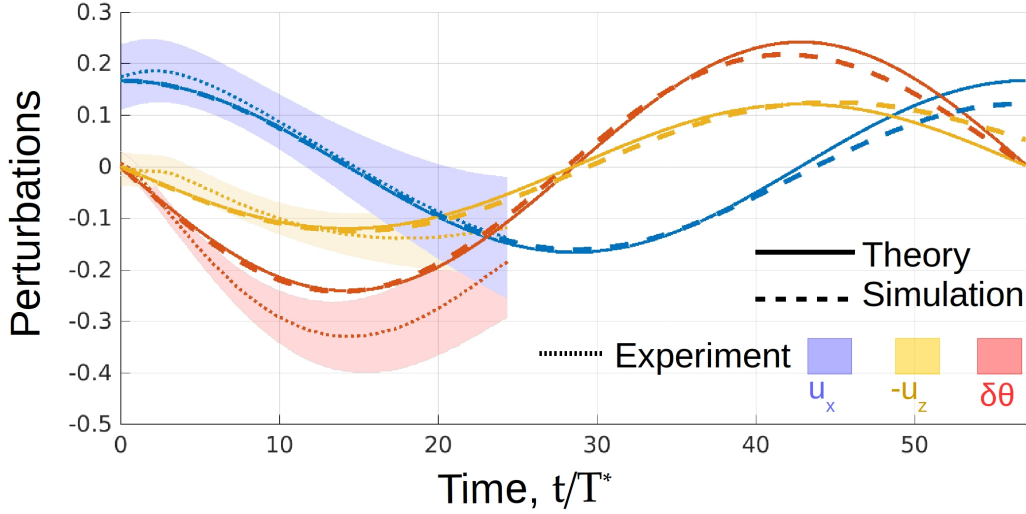


Figure 4.4: **Wavelike mode**: The experimental amplitude for the angle (red patch), horizontal perturbation (blue patch) and vertical perturbation (yellow patch) compared against theory (solid lines) and far-field simulation of oblate spheroids in limit of zero thickness (dashed lines), for the stable case of $q = \pi/2$ and $d/a = 3.75$, with spatial perturbations and time non-dimensionalized by d and $T^* = \mu d^2/F$ respectively. The extent of the shaded region shows the corresponding error in measurement of amplitude.

integration of the far field equations with periodic boundary conditions, remaining in the limit of small a/d but retaining nonlinearities to one further order in u/r than in equations (4.9) - (4.12) [see Supplementary video 2.6].

Wave-like excitations due to Stokesian hydrodynamic interactions also appear in a drifting 1D array of droplets squeezed into a quasi-2D microfluidic channel [66], however, the mode structure is qualitatively distinct from that of the sedimenting disk array due to the absence of internal degrees of freedom, and thus a momentum-like coordinate is missing there. In particular, the wave frequency for droplet arrays goes as $\sin q$ instead of $|\sin q/2|$, and therefore the wave-like excitations of sedimenting disk arrays are more analogous to vibrational modes of a mono-atomic chain. In the next section we make this analogy more precise.

4.6.2 Algebraic growth of vibrational “energy”

The appropriate definition of an inner product is not far to seek. We see from (4.17), that the dynamics in the absence of u_q^z , linearized in θ^n and truncated at nearest neighbours, is precisely that of a chain of particles with mass $1/\alpha(e)$ connected by Hookean springs with stiffness $3a^3/2d^3$. It is convenient to work with rescaled variables $\tilde{\mathbf{X}}_q \equiv [U_q, W_q, \Theta_q]^T = [\sqrt{3a^3/d^3} \sin(q/2)u_q^x, \sqrt{3a^3/d^3} \sin(q/2)u_q^z, \sqrt{\alpha(e)/2} \theta_q]^T$, in terms of which the dynamics reads $d\tilde{\mathbf{X}}_q/dt = \sqrt{6\alpha(e)a^3/d^3} \sin(q/2) \tilde{\mathbf{A}}(q) \tilde{\mathbf{X}}_q$, with

$$\tilde{\mathbf{A}}(q) = \begin{bmatrix} 0 & -i\lambda & 1 \\ i\lambda & 0 & 0 \\ -1 & 0 & 0 \end{bmatrix} = \begin{bmatrix} 0 & -i\lambda & 0 \\ i\lambda & 0 & 0 \\ 0 & 0 & 0 \end{bmatrix} + \begin{bmatrix} 0 & 0 & 1 \\ 0 & 0 & 0 \\ -1 & 0 & 0 \end{bmatrix}, \quad (4.37)$$

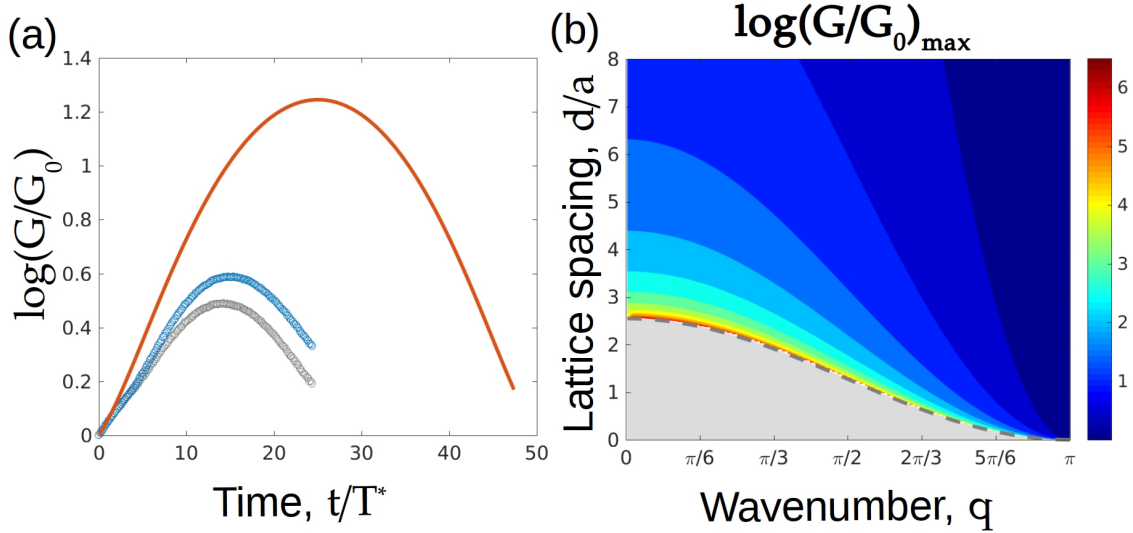


Figure 4.5: **Non-modal growth:** The nonmodal growth plotted for the stable case $q = \pi/2$ and $d/a = 3.75$ (blue) and energy of the analogous mass-and-spring lattice (grey) in experiments, compared with the simulation for the initial condition that gives maximum gain (red) in $t = 14T^*$, where G_0 is the initial amplitude. (c) The log of ratio G/G_0 , of maximum amplitude G of the nonmodal perturbation to the initial amplitude G_0 depicted for the neutrally stable regime in the $q - d/a$ plane.

with $\lambda = \sqrt{3a/2d\alpha(e)} \cos q/2$. For perturbations with $W_q = 0$, the dynamics implied by (4.37) conserves $|U_q|^2 + |\Theta_q|^2$, which is simply the energy for the Hamiltonian part of the dynamics via (4.16) and (4.17). The Euclidean norm $|U_q|^2 + |W_q|^2 + |\Theta_q|^2$ is then a physically reasonable measure of size for vectors with a nonzero W component as well, and the Hermitian conjugate of an operator then takes the familiar form of the complex conjugate of its matrix transpose. From (4.37), $\tilde{\mathbf{A}}(q)$ can be seen to be the sum of a Hermitian operator for the unstable Crowley [51] dynamics of U_q and W_q and a skew-Hermitian (in fact real-antisymmetric) operator for the coupled dynamics of U_q and Θ_q . Each is normal but the two do not commute with each other, and hence $[\tilde{\mathbf{A}}(q), \tilde{\mathbf{A}}^\dagger(q)] \neq 0$, i.e., $\tilde{\mathbf{A}}(q)$ is non-normal.

The equations for $\tilde{\mathbf{X}}_q$ (4.37) imply that the rate of change of the effective energy is

$$\frac{d}{dt} \langle \tilde{\mathbf{X}}_q | \tilde{\mathbf{X}}_q \rangle = 6 \frac{a^2}{d^2} \sin q \operatorname{Im}(U_q^* W_q), \quad (4.38)$$

whence we see that the perturbation can grow for suitable initial choices of U_q and W_q , i.e., u_q^x and u_q^z . The ‘‘vibrational modes’’ contribution $U_q^* U_q + \Theta_q^* \Theta_q$ is precisely half of the total in (4.38). Despite the absence of an eigenvalue with positive real part, non-normality allows the destabilizing coupling between u_q^x and u_q^z to infect the dynamics in the form of transient algebraic growth of perturbations or effective energy even in the ‘stable’ regime of the phase diagram. In Fig 4.5 (a) the grey data is the energy of the harmonic lattice without accounting for the energy of the vertical perturbations, and it thus lies below the full energy given by blue data. The red curve comes from the singular value decomposition of the dynamical matrix, as we discussed below. If the transient amplitude is large enough, nonlinear growth takes over, as in our experiment. In our far-field numerical solution on the other hand, we have the facility to reduce the initial amplitude so much that despite transient growth the system remains linear.

To quantify the nonmodal growth in $q-d$ plane, we calculate the norm of $\exp(\tilde{\mathbf{A}}s)$ for all times s , and calculate the maximum amplitude G_{max} attained by the perturbation over all s , which is finite in the stable regime and depends on wavenumber q and lattice spacing d [see Fig 4.5 (b)]. For each point in (q, d) plane we can predict the initial perturbation which gives the maximum non-modal growth at time s from singular value decomposition of $\exp(\tilde{\mathbf{A}} * s)$ at that point. This initial condition is given by the first column of the right-singular matrix

of $\exp(\tilde{\mathbf{A}} * s)$. The growth of this maximally growing initial lattice configuration is compared against the experimental perturbation using far-field simulation of oblate spheroids in the limit of disk $e \rightarrow 1$ [see red curve Fig 4.5 (a)]. Further, our numerical study of the far-field equations, shows that the observed disruption of the lattice in the stable regime results from amplification of the experimental noise in the initial orientations [see Supplementary videos 2.3 & 2.7].

We see thus that even in the regime where the orientational degree of freedom defeats the Crowley mechanism, and linear stability predicts waves, transient growth ultimately triumphs. An array of sedimenting spheroids is thus disrupted at all q and d . In our numerical study with periodic boundary conditions we are able to observe the waves and delay the onset of nonlinearity by reducing the amplitude of the initial perturbations, unlike in the experiments where there are inevitable imprecisions in the initial conditions.

4.7 Conclusions

In experiment and theory on disks, aligned facing their neighbours in a horizontal one-dimensional lattice and settling at Reynolds number $\sim 10^{-4}$ in a quasi-two-dimensional slab geometry, we find that for large enough lattice spacing, the coupling of disk orientation and translation rescues the array from the clumping instability. Despite the absence of inertia the resulting dynamics displays the wavelike excitations of a mass-and-spring array, with a conserved “momentum” in the form of the collective tilt of the disks and an effective spring stiffness emerging from the viscous hydrodynamic interaction. However, the non-normal character of the dynamical matrix leads to algebraic growth of perturbations even in the linearly stable regime. Stability analysis demarcates a phase boundary in the plane of wavenumber and lattice spacing, separating the regimes of algebraically growing waves and clumping, in quantitative agreement with our experiments.

The wave-like regime that we find is unusual in that we predict, and observe experimentally, large transient growth that ultimately destabilizes the lattice, through nonlinear effects arising from the amplification of initial experimental error in release. Thus, the lattice is nonlinearly unstable over the entire $q - d$ plane, but due to two very different mechanisms.

In our system (4.37) non-normal time evolution originates from non-commutativity between two separately normal parts of the dynamics: that of particle positions alone, and that of orientations coupled to positions. The distinct character of these two contributions is a generic feature of Stokesian hydrodynamic interaction with orientational degrees of freedom. Therefore, algebraic growth is also expected in any future studies of higher dimensional lattices of oriented objects.

Further, we show that the momentum-like character of the particle orientation, seen earlier in pair of settling disks [61], plays a crucial role in the collective dynamics of the disk array. The conservation of total “momentum”, in conjunction with broken continuous translational invariance, yields gapless modes ($\omega \rightarrow 0$ as $q \rightarrow 0$) in this spatially extended driven dissipative system. An important characteristic of the system we have studied is that there is no evolution of the angles when disks are globally rotated. This is related to the orientation-independence of the gravitational energy of *apolar* shapes, but is ultimately a consequence of Stokesian time-reversibility. Objects with *polar* shape will have a preferred orientation in a gravitational field [36, 88, 89], hence a damping of the “momentum” corresponding to $\sum_n \theta^n$, at zero wavenumber in (4.15), and therefore an overdamping of the wavelike modes at small wavenumber.

Chapter 5

Summary and Future Directions

Through the investigations presented in the previous chapters, we find that driven anisotropic particles in the Stokesian regime mimic inertial dynamics, with the anisotropy axis playing the role of momentum.

In a pair of settling disks, effective inertia, that is, the fact that disk orientation plays a role similar to momentum yields Hamiltonian equations whose solution manifests itself as Kepler Orbits of planetary motion, with effective gravitational potential coming from the hydrodynamic interactions. We also find and account for disk-pair orbits with no gravitational analog, within a Hamiltonian framework. The two-body problem is interesting in itself, however, the idea behind studying the two-body problem is the possibility to construct the dynamics of multiple objects using pair-wise hydrodynamic interactions. In the settling pairs, some future investigations could include the study of fully three-dimensional motion, the dynamics of a dissimilar pair of spheroids [see Appendix 6.4], looking for minimal ingredients for János's chaos [16] in pairs of shaped objects, or seeking a Hamiltonian description for settling of other shapes with polarity, chirality [60, 89] and elasticity [127].

In our study of a sedimenting array of disks, we show that particle shape can be used to suppress a classic sedimentation instability. Our investigations uncover an unexpected conservation law and hidden Hamiltonian dynamics which in turn opens a window to the physics of transient growth of linearly stable modes. This unusual growth mechanism should be of relevance in other dissipative dynamical systems, but is not widely known, as not many examples have been identified and studied in the laboratory. We hope our work will draw

the attention of physicists interested in driven nonequilibrium systems, an area of enormous current interest where we expect transient growth to be widespread since non-normality is generically present in these systems [128], and where transient growth has received insufficient attention. An immediate and natural direction in non-equilibrium statistical mechanics is to include random noise in the lattice dynamics of spheroids and study the consequences of particle anisotropy and transient growth in the strong phase separation [54]. Also, it is worth exploring whether the emergence of the Hamiltonian sector leads to equilibrium statistics for particle dynamics projected in the subspace perpendicular to gravity.

The fact that our calculations and the accompanying numerics allow us to capture both the mode-structure and the growth of perturbation amplitude, reassures us that our numerical model can in the future be used to gain a comprehensive understanding of the unstable regime, and other lattice configurations. The effect of walls [129] is not rigorously accounted for in our analysis and numerics, which deserves future attention. Also, our analytical approach fails when particles are almost touching, thus it needs to be refined to include the near-field and excluded-volume interactions.

The dynamics of sedimenting lattices of particles with more complex shapes that are polar or chiral remains open to investigation and are expected to show behaviors distinct from the apolar shapes discussed here. Here, UV-lithography can be used to fabricate various shapes [130] and fully three-dimensional bulk measurements can be done using fluorescent light-sheet imaging. How our screening mechanism of the spheroid array manifests in the formation of clusters and streamers [44, 47] needs an independent investigation. More generally, wavelike excitations have not been observed in the homogeneous sedimenting suspensions of anisotropic objects. Previous experiments on homogeneous suspensions assume, to the best of my knowledge, that randomly stirring and letting the transients die out will generate a perfectly homogeneous initial condition, but this is likely not the case. Whether or not a homogeneous steady state exists, about which perturbations are studied in theory, is not demonstrated in experiments. Thus, if we are to thoroughly understand these systems, we need to achieve precise experimental control on the initial state and perturbations about it, and we hope that the sedimentation community takes up this challenge.

In addition to laboratory experiments, anisotropy-induced drift in Stokesian settling

should enter crucially in the aggregation of tiny ice crystals in early-stage cloud formation, and in the collective motion of non-neutrally-buoyant marine microorganisms in the biological pump. The latter case is particularly exciting due to its “active” nature. Interestingly, the Keplerian dynamics which we present for pairs of disks, with its Hamiltonian structure, also shows up in the pair of settling *Volvox* [69, 70]. Thus our results on arrays could be applicable as is, in the sedimentation of phytoplankton, the detailed investigations of which are warranted, for its relevance to global climate change [98].

Our investigations on active non-inertial particles in vortical flows reveal effective inertial dynamics in the form of centrifugation and caustics. In the caustics regions, the velocity streamlines of the particles can intersect, thus forbidding a velocity field description. This is expected to lead to new directions in the physics of active Stokesian suspensions [35], relevant to biofilm formation in micro-fluidic channels [113], and micro-swimmers in the oceans where small scale vortices are known to generate patchiness [104]. Most previous studies, and our own, have relied on the one-way coupling between particles and flows. It is important to study the effect of two-way coupling on caustics and how it affects preferential aggregation in straining regions. Future investigations will extend our study to a fully three-dimensional scenario, and turbulent flows, akin to the inertial counterpart [102]. Demonstration of active caustics in experiments, even with a single vortex, is still missing and we hope to study it in brine-shrimps. Also, the universality class of both active and inertial caustics remains to be identified. In particular, it will be interesting to know if they are the same. Furthermore, the implications of caustics formation in the coarse-grained description of active suspensions [131] needs further study.

Stokesian suspensions have been intriguing the scientific community for more than a century. The present thesis is thus just a minute addition to the immense literature on the topic. We hope the surprising and beautiful phenomena we have presented and analysed will open fruitful new directions in this evergreen field of research.

Chapter 6

Appendix

6.1 Details of the supplementary movies

[Link to the Supplementary Videos](#)

6.1.1 Movies for Chapter 2: Duet of the Disks

Video 1.1: Symmetric Bound to Scattering transition

The trajectory on the left with $x_o = 0.67 a$ is in a bound orbit and the trajectory on right with $x_o = 1.54 a$ executes scattering orbit. The critical x_o given by the far-field analysis is $x_c = 4a/\pi$.

Video 1.2: Perpendicular Bound to Scattering transition

The trajectory on the left shows bound orbit with $x_o = 2.01 a$ and the trajectory on right executes scattering orbit with $x_o = 4.06 a$. The critical x_o given by the far-field analysis is $x_c = 8a/\pi$.

Video 1.3: Rocking orbit

The discs were released with $\theta_o^- = 0.41 \pi < \pi/2$. The resulting trajectory shows both the discs executing angular oscillations in a range of angles. The rocking to tumbling transition occurs at $\theta_o^- = \pi/2$.

Video 1.4: Hydrodynamic Screening

This video depicts a rare scenario where the far-field results clearly break down. Here, one of the discs finds itself in a hydrodynamic shadow of the other, finding a stable equilibrium state.

6.1.2 Movies for Chapter 3 & 4: Group Dance

Video 2.1: Crowley's Mechanism

Five spheres of diameter 0.6 cm prepared in an array perturbed around an equally spaced configuration with an interparticle spacing 1.5 ± 0.1 cm. The initial perturbation is like that of Fig.3.1 (b) with amplitude 0.25 ± 0.05 cm. Trajectories of the nodes of this perturbation is shown in red. The three-sphere dynamics at later times is expected to be chaotic [16].

Video 2.2: Linearly stable wavelike mode

Initial sinusoidal perturbation with $d = 3.75a$, $qd = \pi/2$, and amplitude $0.625a$; and with trajectory of nodes shown by the dashed red lines. We zoom in on a region where initial errors in release were small, which shows a half cycle of the wavelike oscillation in orientations and positions. More details are in Fig.3.11(b).

Video 2.3: Disruption of waves at late times

This video shows the late-time dynamics for the same q and d as in Video 2. Transient algebraic growth of the perturbations leads to nonlinear effects that disrupt the array.

Video 2.4: Linearly unstable mode

Initial sinusoidal perturbation with $d = 2.5a$, $qd = \pi/4$ and amplitude $0.625a$. More details given in Fig.3.12(b).

Video 2.5: Clumping dynamics at late times.

Late time clumping behaviour of the perturbation with $d = 1.875a$, $qd = \pi/6$ and amplitude $0.625a$. Trajectories of nodes are shown in red color.

Video 2.6: Numerical study of wave-like regime

Numerical integration of the non-dimensionalised far-field equations with initial sinusoidal perturbation of $q = \pi/2$. The interaction is cut-off beyond $1.5d$, such that only nearest neighbours interact hydrodynamically. The region shown here is the same size as the experimental container, scaled by lattice spacing. The initial conditions is the same as in the experiment of Video 2, albeit with periodic boundary condition and no experimental error in initial condition [see Fig 4.4].

Video 2.7: Numerical study of wave-like regime with noisy initial conditions

The initial condition is the same as in Video 6, but we add a random error in the initial orientations uniformly randomly distributed between ± 8 deg, to reflect the measured experimental initial conditions of Video 3 [see Fig 3.6].

6.1.3 Movies for Chapter 5: Swimmers in a Swirl

Video 3.1: Inertial particles in a point vortex.

The video is for number of particles $N = 10^5$ following Maxey-Riley equations around a point vortex, initialized with uniformly random positions on a disk of radius $4\sqrt{\Gamma\tau}$, and with velocities of unit magnitude and uniformly random directions.

Video 3.2: AOUP in a point vortex.

The video is for number of particles $N = 10^5$ noiseless AOUP around a point vortex, initialized with uniformly random positions on a disk of radius $4\sqrt{\Gamma\tau}$, and with orientations \mathbf{w} of unit magnitude and uniformly random directions; for $\beta = 1.0$ and $\alpha = 1$.

Video 3.3: ABP in a point vortex.

The video is for number of particles $N= 10^5$ noiseless ABP around a point vortex, initialized with uniformly random positions on a disk of radius $4\sqrt{\Gamma\tau}$, and with orientations \mathbf{w} of unit magnitude and uniformly random directions; for $\beta = 1.0$ and $\alpha = 1$.

Video 3.4: ABP in unsteady vortical flows.

The video is for number of particles $N= 10^4$ noiseless ABP in an unsteady vortical flow, initialized with uniformly random positions in a 2π periodic domain, and with orientations \mathbf{w} of unit magnitude and uniformly random directions; for an intermediate value of non-dimensional motility $\beta/\bar{U} = 0.24$ with a flow response parameter $\alpha = 1$ and relaxation time $\tau = 1.0$.

6.2 Error in ellipse fitting

To find the error associated with fitting an ellipse in ImageJ, we track a single settling disc in the scattered state, where it follows a straight line path as shown in Figure 1 (a) and (b) . In Figure 1(c) residual with respect to linear fitting gives a measure of error. The measured root mean squared error is $0.019a$ in terms of the radius a of disc. Similarly Figure 1(d) shows the linear fit of angle of the major axis of the fitted ellipse with time giving a slope of -0.0006 and its residual in Figure 1(e) gives the root mean squared error of 0.06 degrees.

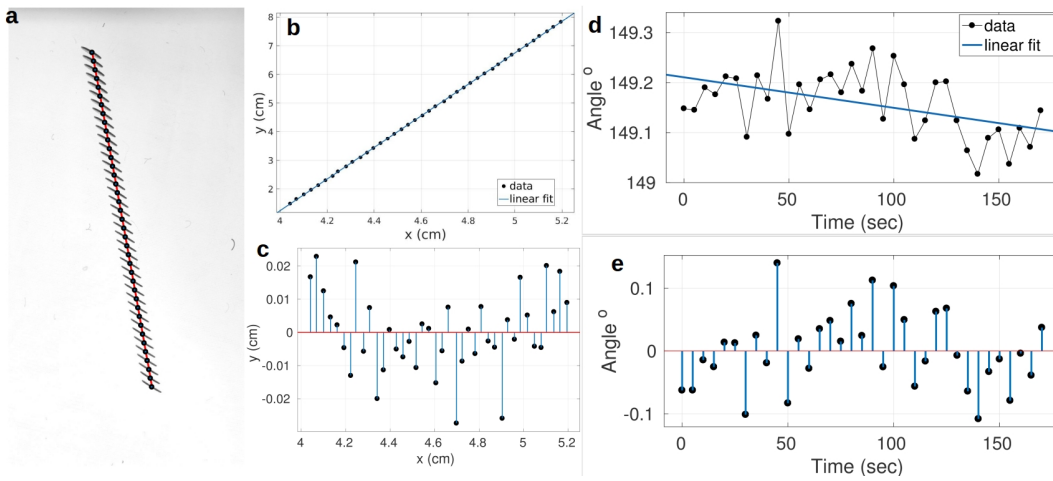


Figure 6.1: Systematic error. (a) the experimental z-stacks of a single disc superimposed with trajectory of the fitted ellipse (b) Linear fit of spatial trajectory of the centroid of fitted ellipse. (c) Residual plot of position (d) angle of the major axis of the fitted ellipse plotted against time. (e) Residual plot of the angle.

6.3 Perpendicular and rocking pair dynamics

Perpendicular release

Substituting the initial horizontal separation $y_o = 0$ and $\theta^+ = \pi/2$ in equations (2.14) - (2.15) and solving for x and y in terms of θ^- gives $x = x_o$, and

$$\frac{\gamma x_o dy}{(x_o^2 + y^2)^{3/2}} = -\alpha \sin \theta^- d\theta^-$$

which upon integration and substituting the value $\alpha/\gamma = \pi/8a$ for disc [34], gives

$$y = \pm \frac{\cos \theta^- x_o}{\sqrt{\left(\frac{8a}{\pi x_o}\right)^2 - \cos^2 \theta^-}}. \quad (6.1)$$

This simplification when $\theta^+ = \pi/2$ can be made for a wide range of initial conditions.

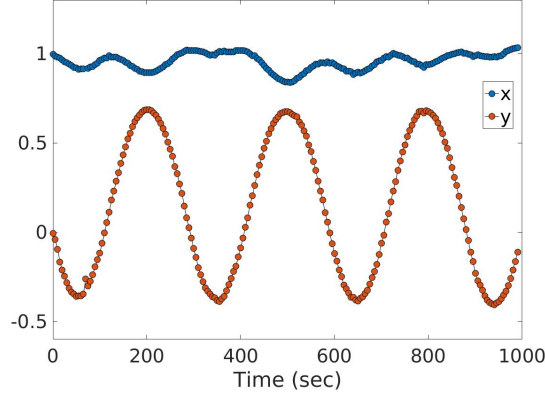


Figure 6.2: Observed vertical separation y (red) and horizontal separation x (blue) plotted against time, shows that y oscillates between positive and negative values and x is nearly constant.

Rocking trajectories

For initial $\theta_o^- < \pi/2$ both the discs rotate in a range of angles which defines the amplitude of angular oscillation. Figure 6.3 shows the experimental trajectories of one of the disc which exhibits both oscillation in a range of angles (red) as well as complete rotations in tumbling orbits, with a transition at $\theta_o^- = \pi/2$. Using equation (2.14) and (2.15) we construct the dynamics in $x - \theta^-$ plane:

$$\frac{xdx}{(x^2 + y^2)^{3/2}} = \frac{\pi \cos \theta^+}{8a} \sin \theta^- d\theta^-$$

using the constraint of equation (2.13)

$$\frac{xdx}{(x^2 + \{y_o - \tan \theta^+ (x - x_o)\}^2)^{3/2}} = \frac{\pi \cos \theta^+}{8a} \sin \theta^- d\theta^- \quad (6.2)$$

defining $I \equiv x_o \tan \theta^+ + y_o$ we rewrite equation (6.2):

$$\frac{xdx}{(x^2 \sec^2 \theta^+ - 2I \tan \theta^+ x + I^2)^{3/2}} = \frac{\pi \cos \theta^+}{8a} \sin \theta^- d\theta^- \quad (6.3)$$

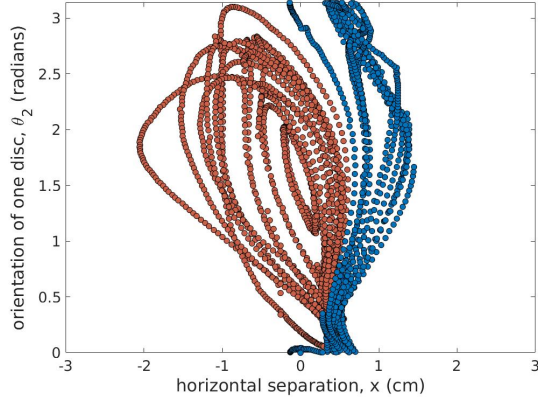


Figure 6.3: Trajectories of one of the disc for $\theta_o^- < \pi/2$ which exhibits oscillation in a range of angles (red) and $\theta_o^- > \pi/2$ showing tumbling orbits (blue).

which upon integration gives:

$$\begin{aligned} \frac{y_o - \tan \theta^+(x - x_o)}{I\sqrt{x^2 \sec^2 \theta^+ - 2I \tan \theta^+ x + I^2}} - \frac{y_o}{I\sqrt{x_o^2 + y_o^2}} \\ = \frac{\pi \cos \theta^+}{8a} (\cos \theta^- - \cos \theta_o^-) \end{aligned} \quad (6.4)$$

which can be solved for θ^- in terms of x :

$$\begin{aligned} \theta = \pm \cos^{-1} \left[\frac{8a}{I\pi \cos \theta^+} \left\{ \frac{y_o - \tan \theta^+(x - x_o)}{\sqrt{x^2 \sec^2 \theta^+ - 2I \tan \theta^+ x + I^2}} \right. \right. \\ \left. \left. - \frac{y_o}{\sqrt{x_o^2 + y_o^2}} \right\} + \cos \theta_o^- \right] \end{aligned} \quad (6.5)$$

6.4 Dissimilar disks

The far-field analysis of settling pairs is useful starting point for a much richer system of settling dissimilar orientable bodies. Briefly, for the specific situation of identical shape but different sizes, we can start from our analysis, and show by perturbation that the bound orbits are unstable in contrast with completely identical pairs.

In the pair of discs with radius a and thickness h , the gravitational force $F = \pi a^2 h \Delta \rho$, $\alpha = -(X_A^{-1} - Y_A^{-1})/12\pi\mu a$ and $\gamma = 1/8\pi\mu$. When the size of one of the disc is perturbed, the solution becomes unstable as one of the disc now rotates differently and falls a little

faster than the other. Using a as the length scale, and time scale $T = 6\pi\mu a^2/F$, the non-dimensional equations of motion for two discs with radius a and $a + \delta$, while ignoring δ^2 terms, read

$$\dot{x} = \frac{3\pi}{16} \sin \theta^- \cos \theta^+ + \frac{3\pi\delta}{32a} \sin(\theta^- + \theta^+) \quad \dot{y} = -\frac{3\pi}{16} \sin \theta^- \sin \theta^+ - \frac{3\pi\delta}{32a} \cos^2(\theta^- + \theta^+)/2 \quad (6.6)$$

$$\dot{\theta}^- = \frac{3}{2} \left(1 + \frac{\delta}{a}\right) \frac{x}{R^3} \quad \dot{\theta}^+ = \frac{3\delta}{2a} \frac{x}{R^3} \quad (6.7)$$

This breaks the conservation of θ^+ , so even if we start with a symmetric case $\theta^+ = y = 0$, the trajectories become asymmetric with time and hence non-Keplerian. Dynamics now happen in a higher dimensional $(x, y, \theta^-, \theta^+)$ space, as compared to any orbits discussed in our letter, which happens in (x, y, θ^-) . Some insight can be gained for the instability of Kepler orbits with respect to perturbation in size of one disc, by numerical integration of the above equation for symmetric initial conditions [see Fig 6.4] $\theta^+ = 0 = y$.

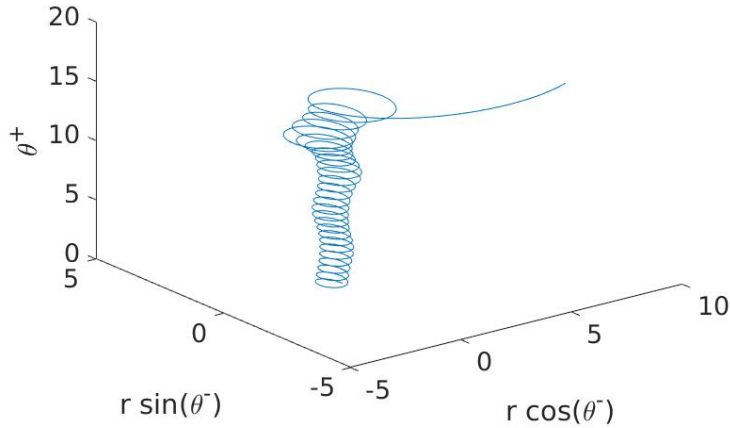


Figure 6.4: 3D Plot where x-axis is $r \cos(\theta^-)$, y-axis is $r \sin(\theta^-)$ and z-axis is θ^+ , shows instability of Kepler orbits with dissimilar discs having $\delta = 0.1a$, and initial horizontal separation $0.4a$.

6.5 Stable orientations around a force monopole

To see how our mechanism could qualitatively change the Koch & Shaqfeh's picture schematically [Figure 1 in their paper], consider a force monopole at the origin and a disk of radius a settling in its flow field at a radial distance r , with position $(x, 0, z)$. With both the symmetric and antisymmetric part of the velocity gradients, the orientation of the disk evolve, to leading far-field order in (a/r) [12], according to

$$\frac{d\theta}{dt} = \frac{x}{8\pi r^3} - \frac{3z}{8\pi r^5} (x \cos \theta + z \sin \theta) (z \cos \theta - x \sin \theta). \quad (6.8)$$

Here, the first term is the contribution due to antisymmetric part and the second due to the symmetric part of the velocity gradient of the flow field generated by a force monopole of magnitude F at the origin. Note that the above equation is non-dimensionalised using length a and time $\mu a^2/F$, where μ is the viscosity.

$$\frac{d\theta'}{dt} = \frac{\sin \phi}{8\pi r^2} \left[\cot \phi - \frac{3}{2} \sin 2(\theta' - \phi) \right] \quad (6.9)$$

Note: $\theta' = \pi/2 + \theta$ is now measured with respect to the positive x axis, like the azimuthal angle ϕ .

Now, without the antisymmetric coupling and local interparticle interaction one gets the stable orientations seen in the Koch & Shaqfeh's schematic figure and thus an inwards particle flux from all directions. In our study, for the wavelike excitations in the lateral direction, this antisymmetric rotational coupling is crucial and so is the local interparticle interaction. To find the stable orientations while incorporating antisymmetric coupling, we proceed by defining the angle

$$\beta \equiv \frac{1}{2} \sin^{-1} \left[\frac{2}{3} \cot \phi \right]. \quad (6.10)$$

From (6.9) we get the solution of $d\theta'/dt = 0$ for any given point in (r, ϕ) in terms of β as

$$\theta' = \phi + \frac{n\pi}{2} + (-1)^n \beta, \quad (6.11)$$

where n takes integer values. We can immediately see from (6.10) that solutions do not exist for all values of ϕ which is qualitatively distinct feature from Koch & Shaqfeh's picture.

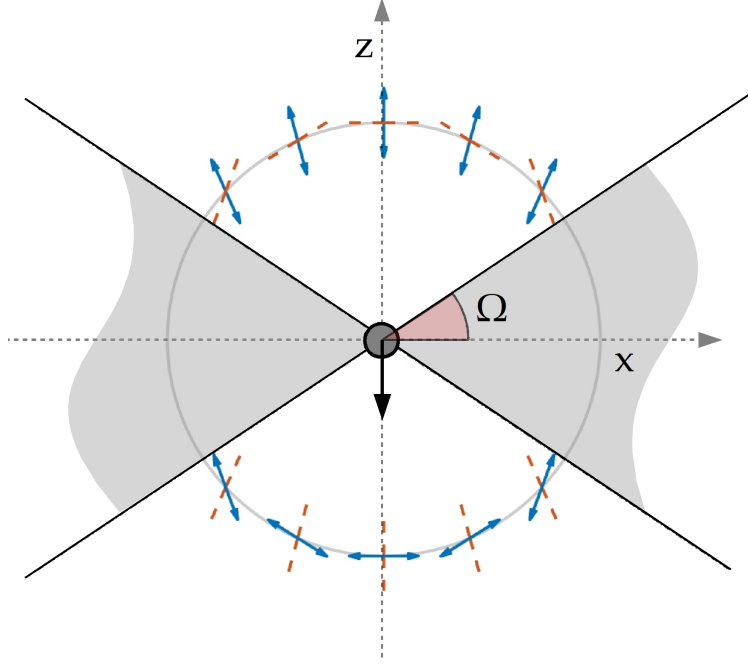


Figure 6.5: **Stable orientations with both symmetric and antisymmetric part of velocity gradient:** With force monopole at the origin. Blue double ended arrow and red dashed lines are stable and unstable orientations respectively, evaluated at the spheroid centre. The small angle between stable and unstable orientations is $\pi/2 - 2\beta$. The shaded grey region represents the range of angles ϕ where there are no stable orientations, with $\Omega = \tan^{-1}(2/3)$.

For, $\Omega \equiv \tan^{-1}(2/3)$, the solution for $d\theta'/dt = 0$ is defined only for the values of ϕ in the intervals: $(\Omega, \pi - \Omega)$ and $(\pi + \Omega, 2\pi - \Omega)$. Even where the solution exists we show below that the stable orientations are different from what one gets with just symmetric rotational coupling.

We can study the stability, by considering only two solutions: $\theta' = \phi + \beta$ and $\theta' = \phi - \beta + \pi/2$, given the apolarity of spheroids. Perturbing the first solution by small angle $\delta\theta$, substituting in (6.9) and taylor expanding about this solution gives

$$\dot{\delta\theta} = \frac{\sin \phi}{8\pi r^2} \left[\cot \phi - \frac{3}{2} \sin 2\beta - 3\delta\theta \cos 2\beta \right]. \quad (6.12)$$

Since, $\cot \phi = 3 \sin(2\beta)/2$ by definition of β (6.10), we get

$$\dot{\delta\theta} = -\frac{3 \sin \phi}{8\pi r^2} \delta\theta \cos 2\beta. \quad (6.13)$$

Thus, the solution $\theta' = \phi + \beta$ is stable in the upper half plane and unstable in the lower half. Similarly, by perturbing the second solution $\theta' = \phi - \beta + \pi/2$ by a small angle $\delta\theta$, we get

$$\dot{\delta\theta} = \frac{3 \sin \phi}{8\pi r^2} \delta\theta \cos 2\beta, \quad (6.14)$$

which is unstable in the upper half plane and stable in the lower half.

To summarize – [see Fig.6.5] in the upper half plane the spheroid is stable with its long-axis oriented along the angle $\theta' = \phi + \beta$ and in the lower half plane the stable angle for the long-axis is $\theta' = \phi - \beta + \pi/2$. While in both the half planes the solutions exist only with the azimuthal angle ϕ lying in the intervals $(\Omega, \pi - \Omega)$ and $(\pi + \Omega, 2\pi - \Omega)$, leaving out regimes shown as grey shaded region in Fig.6.5, where there are no stable orientations, and our waves lie precisely within this shaded region.

The assumption that oriented particles spend most of their times with their long dimension aligned to the extensional direction of the symmetric part of the local velocity gradient clearly does not hold true for our system of disk array. In particular, antisymmetric coupling and local interparticle interactions can have a significant role in collective behaviour. However, a detailed discussion on how exactly our mechanism manifests itself in the statistical theory of a homogenous suspension would require an independent investigation with special care on antisymmetric rotational coupling and local interparticle interactions.

6.6 Noiseless AOUP and ABP in a point vortex

AOUP

In the absence of external field ϕ , redefining a U dependent relaxation time, $\tilde{\tau}^{-1} \equiv \mathbb{I}/\tau - (\alpha \mathbb{S} + \mathbb{A})$, gives the equation

$$\frac{d\mathbf{v}}{dt} - \mathbf{v} \cdot \nabla \mathbf{U} = (\mathbf{U} - \mathbf{v}) \cdot \tilde{\tau}^{-1} \quad (6.15)$$

The velocity field generated by a point-vortex in polar coordinates is

$$\mathbf{U} = \frac{\Gamma}{2\pi r} \hat{\theta} \equiv \frac{\bar{\Gamma}}{r} \hat{\theta} \quad (6.16)$$

In polar coordinates the position derivatives are

$$\mathbf{X} = r\hat{\mathbf{r}}$$

$$\frac{d\mathbf{X}}{dt} = \frac{dr}{dt}\hat{\mathbf{r}} + r\frac{d\hat{\theta}}{dt} \quad (6.17)$$

$$\frac{d^2\mathbf{X}}{dt^2} = \frac{d^2r}{dt^2}\hat{\mathbf{r}} + 2\frac{dr}{dt}\frac{d\hat{\theta}}{dt} - r\left(\frac{d\hat{\theta}}{dt}\right)^2\hat{\mathbf{r}} + r\frac{d^2\hat{\theta}}{dt^2} \quad (6.18)$$

To see the emergence of effective centripetal and centrifugal forces due to coupling with the background flow, we neglect the potential term and the gaussian white noise in the original equation (4.2) for AOUP. For a point vortex the antisymmetric tensor \mathbb{A} is zero everywhere except at the origin. And the symmetric part is

$$\mathbb{S} = \begin{pmatrix} 0 & -\tilde{\Gamma}/r^2 \\ -\tilde{\Gamma}/r^2 & 0 \end{pmatrix} \quad (6.19)$$

Using (4.5)-(4.8) in (4.4) gives

$$\begin{aligned} \tau \left[\frac{d^2r}{dt^2}\hat{\mathbf{r}} + 2\frac{dr}{dt}\frac{d\hat{\theta}}{dt} - r\left(\frac{d\hat{\theta}}{dt}\right)^2\hat{\mathbf{r}} + r\frac{d^2\hat{\theta}}{dt^2} + \frac{\tilde{\Gamma}}{r}\frac{d\hat{\theta}}{dt}\hat{\mathbf{r}} + \frac{\tilde{\Gamma}}{r^2}\frac{dr}{dt}\hat{\theta} \right] &= \frac{\bar{\Gamma}}{r}\hat{\theta} - \frac{dr}{dt}\hat{\mathbf{r}} - r\frac{d\hat{\theta}}{dt} \\ &+ \frac{\alpha\tau\tilde{\Gamma}}{r^3}\hat{\mathbf{r}} - \frac{\tau\alpha\tilde{\Gamma}}{r}\frac{d\hat{\theta}}{dt}\hat{\mathbf{r}} - \frac{\tau\alpha\tilde{\Gamma}}{r^2}\frac{dr}{dt}\hat{\theta} \end{aligned} \quad (6.20)$$

Separating $\hat{\mathbf{r}}$ and $\hat{\theta}$ directions in (6.20) we get two coupled equations

$$\tau\frac{d^2r}{dt^2} - \tau r\left(\frac{d\hat{\theta}}{dt}\right)^2 = -\frac{dr}{dt} + \frac{\alpha\tau\tilde{\Gamma}^2}{r^3} - \frac{\tau(1+\alpha)\tilde{\Gamma}}{r}\frac{d\hat{\theta}}{dt} \quad (6.21)$$

$$2\tau\frac{dr}{dt}\frac{d\hat{\theta}}{dt} + \tau r\frac{d^2\hat{\theta}}{dt^2} = \frac{\bar{\Gamma}}{r} - r\frac{d\hat{\theta}}{dt} - \frac{\tau(1+\alpha)\tilde{\Gamma}}{r^2}\frac{dr}{dt} \quad (6.22)$$

ABP

$$\frac{d\mathbf{v}}{dt} - \mathbf{v} \cdot \nabla \mathbf{U} = (\mathbf{U} - \mathbf{v}) \cdot \tilde{\tau}^{-1} \quad (6.23)$$

where $\tilde{\tau}^{-1} \equiv \frac{\|\mathbf{V}-\mathbf{U}\|}{\beta^2} - 1) - (\alpha\mathbb{S} + \mathbb{A})$. The non-dimensional equations with $R = \sqrt{\tilde{\Gamma}}\tau$ and $T = \tau$, in cylindrical polar coordinates becomes

$$\kappa^2\frac{d^2r}{dt^2} = \kappa^2r\left(\frac{d\hat{\theta}}{dt}\right)^2 + \frac{dr}{dt}\left\{2\frac{d\hat{\theta}}{dt} - \left(\frac{dr}{dt}\right)^2 - r^2\left(\frac{d\hat{\theta}}{dt}\right)^2 + \kappa^2 - \frac{1}{r^2}\right\} + \frac{\kappa^2\alpha}{r^3} - \frac{\kappa^2(1+\alpha)}{r}\frac{d\hat{\theta}}{dt} \quad (6.24)$$

$$\kappa^2 r \frac{d^2 \theta}{dt^2} = -2\kappa^2 \frac{d\theta}{dt} \frac{d\theta}{dt} + \left(r \frac{d\theta}{dt} - \frac{1}{r} \right) \left\{ 2 \frac{d\theta}{dt} - \left(\frac{dr}{dt} \right)^2 - r^2 \left(\frac{d\theta}{dt} \right)^2 + \kappa^2 - \frac{1}{r^2} \right\} - \frac{\kappa^2(1+\alpha)}{r^2} \frac{dr}{dt} \quad (6.25)$$

where $\kappa \equiv \beta \sqrt{\tau / \tilde{\Gamma}}$ is the non-dimensional motility. The corresponding first order equations are

$$\frac{dr}{dt} = v_r \quad (6.26)$$

$$\kappa^2 \frac{dv_r}{dt} = \kappa^2 r \omega^2 + v_r \left\{ 2\omega - v_r^2 - r^2 \omega^2 + \kappa^2 - \frac{1}{r^2} \right\} + \frac{\kappa^2 \alpha}{r^3} - \frac{\kappa^2(1+\alpha)\omega}{r} \quad (6.27)$$

$$\frac{d\theta}{dt} = \omega \quad (6.28)$$

$$\kappa^2 \frac{d\omega}{dt} = -\frac{2\kappa^2 v_r \omega}{r} + \left(\omega - \frac{1}{r^2} \right) \left\{ 2\omega - v_r^2 - r^2 \omega^2 + \kappa^2 - \frac{1}{r^2} \right\} - \frac{\kappa^2(1+\alpha)v_r}{r^3} \quad (6.29)$$

Bibliography

- [1] M.A. Jones & M.J. Shelley, Falling cards. *J. Fluid Mech.* **540**, 393–425 (2005)
- [2] S.B. Feild et al., Chaotic dynamics of falling disks. *Nature* **388**, 252–254 (1997)
- [3] G.G. Stokes, On the effect of the internal friction of fluids on the motion of pendulums. *Trans. Camb. Phil. Soc.* **IX**, 8 (1851)
- [4] J.F. Brady & G. Bossis, Stokesian Dynamics. *Annu. Rev. Fluid Mech.* **20**, 111–157 (1988)
- [5] S. Ramaswamy, Issues in the statistical mechanics of steady sedimentation. *Advances in Physics* **50**, 297–341 (2001).
- [6] J. Happel & H. Brenner, *Low Reynolds number Hydrodynamics: with special applications to particulate media*, Kluwer publishers. **1**, (1983).
- [7] E.M. Purcell, Life at low Reynolds number, *American Journal of Physics* **45**, 3-11 (1977).
- [8] Eric Lauga, Life around the scallop theorem, *Soft Matter* **7**, 3060–3065 (2011).
- [9] G.I. Taylor, Film Notes for “Low-Reynolds-Number Flows”(National Committee for Fluid Mechanics Films, Encyclopaedia Britannica Educational Corporation, Chicago, 1967).
- [10] F. Gadala-Maria & A. Acrivos, Shear-Induced Structure in a Concentrated Suspension of Solid Spheres, *J. Rheol.* **24**, 799 (1980).

- [11] Élisabeth Guazzelli & Jeffrey F. Morris, A Physical Introduction to Suspension Dynamics, Cambridge University Press . , (2011).
- [12] S. Kim & S.J. Karrila, Microhydrodynamics: Principles and Selected Applications, Dover publications, (1991).
- [13] C. Pozrikidis , Boundary Integral and Singularity Methods for Linearized Viscous Flow, Cambridge University Press, (1992).
- [14] M. Smoluchowski On the mutual action of spheres which move in a viscous liquid, Bull. Inter. acad. Polonaise sci. lett. **1A**, 28-39 (1911).
- [15] M. Stimson & G.B. Jeffery, The Motion of two spheres in a viscous fluid. Proc. R. Soc. Lond. **A111**, 110 (1926)
- [16] I.M. Jánosi *et al.* , Chaotic particle dynamics in viscous flows: The three-particle Stokeslet problem. Phys. Rev. E **56-3**, 2858–2868 (1997)
- [17] M.L.E. Jeżewska *et al.*, Periodic sedimentation of three particles in periodic boundary conditions, Physics of Fluids **17**, 093102-1-9 (2005).
- [18] R.H. Davis & A. Acrivos, Sedimentation of noncolloidal particles at low Reynolds numbers. Annu. Rev. Fluid Mech. **17**, 91 – 118 (1985)
- [19] J.-Z. Xue et al., Diffusion, dispersion, and settling of hard spheres, Phys. Rev. Lett. **69**, 1715-1718 (1992).
- [20] Paul Chaikin, Thermodynamics and hydrodynamics of hard spheres: the role of gravity, Soft and Fragile Matter, Scottish Graduate Series, 315-348 (2000).
- [21] D.L. Koch & E.S.G. Shaqfeh, Screening in sedimenting suspensions, J. Fluid Mech. **224**, 275-303 (1991).
- [22] G.K. Batchelor, Sedimentation in a dilute dispersion of spheres., J. Fluid Mech. **52**, 245 – 68 (1972).

- [23] R.E. Caflisch & Jonathan H. C. Luke, Variance in the sedimentation speed of a suspension, *Phys. Fluids* **28**, 759 (1985).
- [24] H. Nicolai & Élisabeth Guazzelli, Effect of the vessel size on the hydrodynamic diffusion of sedimenting spheres. *Physics of Fluids* **7**, 3 (1995).
- [25] P. N. Segrè, E. Herbolzheimer & P.M. Chaikin, Long-Range Correlations in Sedimentation, *Phys. Rev. Lett.* **79**, 13 (1997).
- [26] Alex Levine et. al. Screened and Unscreened Phases in Sedimenting Suspensions, *Phys. Rev. Lett.* **81**, 5944-5947 (1998).
- [27] K.V. Kumar, PhD thesis, Indian Instt. of Science (2010).
- [28] É. Guazzelli & J. Hinch, Fluctuations and Instability in Sedimentation, *Annu. Rev. Fluid Mech.* **43**, 96–116 (2011).
- [29] T. Goldfriend *et al.*, Screening, Hyperuniformity, and Instability in the Sedimentation of Irregular Objects, *Phys. Rev. Lett.* **118**, 158005-1-6 (2017).
- [30] G.I. Taylor, *Low Reynolds Number Flows* (National Committee for Fluid Mechanics Films, Encyclopaedia Britannica Educational Corporation, Chicago, 1985).
- [31] J. Tillett, Axial and transverse Stokes flow past slender axisymmetric bodies., *J. Fluid Mech.* **44(3)**, 401 – 417 (1970).
- [32] A.T. Chwang & T.Y. Wu, Hydromechanics of low Reynolds number flow, Part 2. *J. Fluid Mech.* **67**, 787–815 (1975)
- [33] S. Wakiya, Mutual interaction of two spheroids sedimenting in a viscous fluid. *J. Phys. Soc. Jpn.* **20**, 1502–1514 (1965)
- [34] S. Kim, Sedimentation of two arbitrarily oriented spheroids in a viscous fluid. *Intl J. Multiphase flow* **11**, 699–712 (1985)
- [35] S. Jung, S.E. Spagnolie, K. Parikh, M. Shelley & A.K. Tornberg, Periodic sedimentation in a Stokesian fluid. *Phys. Rev. E* **74**, 035302 (2006)

- [36] T. Goldfriend *et al.*, Hydrodynamic Interactions between Two Forced Objects of Arbitrary Shape. I. Effect on Alignment. *Physics of Fluids* **27**, 123303 (2015)
- [37] T. Goldfriend *et al.*, Hydrodynamic Interactions between Two Forced Objects of Arbitrary Shape. II. Relative translation. *Phys. Rev. E* **93**, 042609 (2016)
- [38] S. Kim, Singularity solutions for ellipsoids in low-Reynolds-number flows: With applications to the calculation of hydrodynamic interactions in suspensions of ellipsoids. *Intl J. Multiphase flow* **12 (3)**, 469–491 (1986)
- [39] D.L. Koch & E.S.G. Shaqfeh, The instability of a dispersion of sedimenting spheroids, *J. Fluid Mech.* **209**, 521-542 (1989).
- [40] I.L. Claeys & J.F. Brady Suspensions of prolate spheroids in Stokes flow. Part 1. Dynamics of a finite number of particles in an unbounded fluid, *J. Fluid Mech.* **251**, 411–422 (1993).
- [41] G.B. Jeffery, The motion of ellipsoidal particles immersed in a viscous fluid. *Proc. R. Soc. Lond.* **102**, 161–179 (1922)
- [42] B. Metzger, J.E. Butler & Élisabeth Guazzelli, Experimental investigation of the instability of a sedimenting suspension of fibres, *J. Fluid Mech.* **575**, 307-332 (2007).
- [43] B. Herzhaft et al., Experimental Investigation of the Sedimentation of a Dilute Fiber Suspension, *Phys. Rev. Lett.* **77**, 290–293 (1996).
- [44] B. Metzger, Élisabeth Guazzelli & J.E. Butler, Large-Scale Streamers in the Sedimentation of a Dilute Fiber Suspension, *Phys. Rev. Lett.* **95**, 164506 (2005).
- [45] M. Mackaplow & E. Shaqfeh A numerical study of the sedimentation of fibre suspensions, *J. Fluid Mech.* **376**, 149–182 (1998).
- [46] J. Butler & E. Shaqfeh Dynamic simulations of the inhomogeneous sedimentation of rigid fibres., *J. Fluid Mech.* **648**, 205–237 (2002).
- [47] K. Gustavsson & A.-K. Tornberg, Gravity induced sedimentation of slender fibers, *Phys. Fluids* **21**, 123301 (2009).

- [48] J. Park et al., A cloud of rigid fibres sedimenting in a viscous fluid, *J. Fluid Mech.* **648**, 351 – 362 (2010).
- [49] K. Adachi, S. Kiriya & N. Yoshioka, The behavior of a swarm of particles moving in a viscous fluid, *Chemical Engineering Science* **33**, 115 – 121 (1978).
- [50] B. Metzger, J.E. Butler & Élisabeth Guazzelli, On wavelength selection by stratification in the instability of settling fibers, *Phys. Fluids* **19**, 098105 (2007).
- [51] J.M. Crowley, Viscosity-induced instability of a one-dimensional lattice of falling spheres. *J. Fluid Mech.* **45**, 151–159 (1971)
- [52] J.M. Crowley, Clumping instability of a falling horizontal lattice, *The Physics of Fluids* **19**, 1296 (1976).
- [53] R. Lahiri & S. Ramaswamy, Are Steadily Moving Crystals Unstable?, *Phys. Rev. Lett.* **79**, 1150–1153 (1997).
- [54] R. Lahiri, M. Barma & S. Ramaswamy, Strong phase separation in a model of sedimenting lattices, *Phys. Rev. E* **61**, 1648–1658 (2000).
- [55] R.A. Simha & S. Ramaswamy, Traveling Waves in a Drifting Flux Lattice, *Phys. Rev. Lett.* **88**, 3285–3288 (1999).
- [56] N. Liron & S. Mochon, Stokes flow for a stokeslet between two parallel flat plates, *10 J. Eng. Math*, 287–303 (1976).
- [57] Bianxiao Cui et al., Anomalous Hydrodynamic Interaction in a Quasi-Two-Dimensional Suspension, *Phys. Rev. Lett.* **92**, 258301 (2004).
- [58] L.D. Landau & E.M. Lifshitz, *Mechanics: Course of Theoretical Physics*. **1**.
- [59] L.F. Shatz, Singularity method for oblate and prolate spheroids in Stokes and linearized oscillatory flow. *Physics of Fluids* **16**, 664 (2004).
- [60] T.A. Witten & H. Diamant, A review of shaped colloidal particles in fluids: Anisotropy and chirality, arXiv:2003.03698 [physics.flu-dyn], (2020).

- [61] R. Chajwa , N. Menon & S. Ramaswamy, Kepler Orbits in Pairs of Disks Settling in a Viscous Fluid, *Phys. Rev. Lett.* **122**, 224501 (2019).
- [62] R. Chajwa , N. Menon, S. Ramaswamy & R. Govindarajan, Waves, algebraic growth and clumping in sedimenting disk arrays , *Phys. Rev. X* **10**, 041016 (2020).
- [63] A.J.C Ladd & R. Verberg Lattice-Boltzmann Simulations of Particle-Fluid Suspensions, *Journal of Statistical Physics* **104 (5-6)**, 1191–1251 (2001).
- [64] Shang-You Tee et. al, Nonuniversal Velocity Fluctuations of Sedimenting Particles, *Phys. Rev. Lett.* **89**, 054501-4 (2002).
- [65] A.A. Zick & G.M. Homsy, Stokes flow through periodic arrays of spheres, *J. Fluid Mech.* **115**, 13-26 (1982).
- [66] T. Beatus, T. Tlusty & R. Bar-Ziv, Phonons in a one-dimensional microfluidic crystal. *Nature Phys* **2**, 743–748 (2006).
- [67] A. Zöttl & H. Stark, Nonlinear Dynamics of a Microswimmer in Poiseuille Flow, *Phys. Rev. Lett.* **108**, 218104 (2012).
- [68] H. Stark, Swimming in external fields, *Eur. Phys. J. Special Topics* **225**, 2369–2387 (2016).
- [69] A. Bolitho, R. Singh & R. Adhikari, Periodic Orbits of Active Particles Induced by Hydrodynamic Monopoles, *Phys. Rev. Lett.* **124**, 088003 (2020).
- [70] A. Bolitho, R. Singh & R. Adhikari, Erratum: Periodic Orbits of Active Particles Induced by Hydrodynamic Monopoles [*Phys. Rev. Lett.* 124, 088003 (2020)], *Phys. Rev. Lett.* **125**, 099901 (2020).
- [71] E. Lushi & P. M. Vlahovska Periodic and Chaotic Orbits of Plane-Confined Micro-rotors in Creeping Flows, *Journal of Nonlinear Science* **25**, 1111–1123 (2015).
- [72] N. Oppenheimer, D.B. Stein & M.J. Shelley, Rotating Membrane Inclusions Crystallize Through Hydrodynamic and Steric Interactions, *Phys. Rev. Lett.* **123**, 148101 (2019).

- [73] Brian Farrell, Modal and nonmodal Baroclinic Waves , *Journal of the Atmospheric Sciences* **41**, 668-673 (1983).
- [74] Subrahmanyam Chandrasekhar, *Hydrodynamic and Hydromagnetic Stability*, Dover Publications, Inc. New York (1961).
- [75] P.J. Schmid, Nonmodal Stability Theory, *Annual Rev. Flu. Mech.* **39**, 129-162 (2007).
- [76] R.R. Kerswell, Nonlinear Nonmodal Stability Theory, *Annual Rev. Flu. Mech.* **50**, 319 – 45 (2018).
- [77] M. T. Landahl, A note on an algebraic instability of inviscid parallel shear flows, *J. Fluid Mech.* **98**, 243–251 (1980).
- [78] K.M. Case, Stability of Inviscid Plane Couette Flow, *The Physics of Fluids* **3**, 143 (1960).
- [79] Lloyd N. Trefethen et. al., Hydrodynamic Stability Without Eigenvalues, *Science* **261**, 578-584 (1993).
- [80] Lloyd N. Trefethen & Mark Embree, *Spectra and Pseudospectra: The Behavior of Nonnormal Matrices and Operators*, Princeton University Press, Princeton New Jersey (2005).
- [81] R. Bale & R. Govindarajan, Transient growth and why we should care about it, *Resonance* **15**, 441-457 (2010).
- [82] David Politzer, The plucked string: An example of non-normal dynamics, *American Journal of Physics* **83**, 395 (2015).
- [83] Matthew P. Juniper, Optimization with non-linear adjoint looping, Int’l Summer School and Workshop on Non-Normal and Nonlinear Effects in Aero- and Thermoacoustics, Munich, Germany (2010).
- [84] P.J. Schmid & L. Brandt, Analysis of Fluid Systems: Stability, Receptivity, Sensitivity, *ASME Appl. Mech. Rev.* **66**, 024803 (2014).

- [85] P.C. Martin, O. Parodi & P.S. Pershan, Unified Hydrodynamic Theory for Crystals, Liquid Crystals, and Normal Fluids, *Phys. Rev. A* **6**, 2401-20 (1972).
- [86] M.M.M. El Telbany & A.J. Reynolds, The Structure of Turbulent Plane Couette Flow, *J. Fluids Eng.* **104(3)**, 367-372 (1982).
- [87] L. Balents, M.C. Marchetti & L. Radzihovsky, Nonequilibrium steady states of driven periodic media, *Phys. Rev. B* **57**, 7705 (1998).
- [88] M.L.Ekiel-Jezewskaa & E. Wajnryb, Hydrodynamic orienting of asymmetric microobjects under gravity, *J. Phys.: Condens. Matter* **21**, 204102 (2009).
- [89] A. Conway et. al., Sedimentation of polygonal tiles. *Bulletin of the American Physical Society* **64**, (2019).
- [90] N.W. Krapf, T.A. Witten & N.C. Keim, Chiral sedimentation of extended objects in viscous media, *Phys. Rev. E* **79**, 056307 (2009).
- [91] T.A. Witten & H. Diamant A review of shaped colloidal particles in fluids: Anisotropy and chirality, *arXiv:2003.03698 [physics.flu-dyn]* (2020).
- [92] C. E. Marshall, Studies in the Degree of Dispersion of the Clays. IV. The Shapes of Clay Particles., *J. Phys. Chem.* **45(1)**, 81-93 (1941).
- [93] W.T. Hung, A.F. Collings & J. Low, Erythrocyte Sedimentation Rate Studies in Whole Human Blood, *Phys. Med. Biol.* **39 (11)**, 1855-73 (1994).
- [94] A. Kempczyński et al., Fluctuations in settling velocity of red blood cell aggregates, *Optica Applicata* **44 (3)**, 365–373 (2014).
- [95] M.B. Pinsky & A.P. Khain, Turbulence effects on droplet growth and size distribution in clouds – a review, *J. Aerosol Sci.* **28**, 1177-1214 (1997).
- [96] R.A. Shaw et al., Preferential Concentration of Cloud Droplets by Turbulence: Effects on the Early Evolution of Cumulus Cloud Droplet Spectra, *J. Atmos. Sci.* **55**, 1965 – 1976. (1998).

- [97] H.J.S. Fernando et al. Flow, turbulence, and pollutant dispersion in urban atmospheres, *Phys. Fluids* **22**, 051301 (2010).
- [98] P.W. Boyd et al. Multi-faceted particle pumps drive carbon sequestration in the ocean, *Nature* **568**, 327-335 (2019).
- [99] G. Boffetta, F. De Lillo & A. Gamba, Large scale inhomogeneity of inertial particles in turbulent flows, *Physics of Fluids* **16**, L20 (2004).
- [100] M.R. Maxey & S. Corrsin, Gravitational Settling of Aerosol Particles in Randomly Oriented Cellular Flow Fields, *J. Atmos. Sci.* **43** (**11**), 1112–1134 (1986).
- [101] S. Ravichandran & Rama Govindarajan, Caustics and clustering in the vicinity of a vortex, *Phys. Fluids* **27**, 033305 (2015).
- [102] M. Wilkinson & B. Mehlig, Caustics in turbulent aerosols, *EPL* **71**, 186 (2005).
- [103] P. Deepu, S. Ravichandran & Rama Govindarajan, Caustics-induced coalescence of small droplets near a vortex, *Phys. Rev. Fluids* **2**, 024305 (2017).
- [104] W.M. Durham et al. Turbulence drives microscale patches of motile phytoplankton, *Nature Communications* **4**, 2148 (2013).
- [105] A. Abelson & M. Denny, Settlement of marine organisms in flow, *Annu. Rev. Ecol. Syst.* **28**, 317–339 (1997).
- [106] T.J. Pedley & J.O. Kessler, Hydrodynamic phenomena in suspensions of swimming microorganisms., *Annu. Rev. Fluid Mech.* **24**, 313–358 (1992).
- [107] A. Genin Bio-physical coupling in the formation of zooplankton and fish aggregations over abrupt topographies, *Journal of Marine Systems* **50**, 3–20 (2004).
- [108] W.M. Durham, J.O. Kessler & R. Stocker, Disruption of Vertical Motility by Shear Triggers Formation of Thin Phytoplankton Layers, *Science* **323**, 1067 (2009).
- [109] C. Torney & Z. Neufeld , Transport and Aggregation of Self-Propelled Particles in Fluid Flows, *Phys. Rev. Lett.* **99**, 078101 (2007).

- [110] C. Zhan Accumulation of motile elongated micro-organisms in turbulence, *J. Fluid Mech.* **739**, 22-36 (2013).
- [111] A. Sokolov & I.S. Aranson, Rapid expulsion of microswimmers by a vortical flow, *Nature Communications* **7**, 11114 (2016).
- [112] W.M. Durham, E. Climent & R. Stocker, Gyrotaxis in a Steady Vortical Flow, *Phys. Rev. Lett.* **106**, 238102 (2011).
- [113] S. Yazdi & A.M. Ardekani, Bacterial aggregation and biofilm formation in a vortical flow, *Biomicrofluidics* **6**, 044114 (2012).
- [114] José-Agustín Arguedas-Leiva & Michael Wilczek, Microswimmers in an axisymmetric vortex flow, *New J. Phys.* **22**, 053051 (2020).
- [115] Mitsusuke Tarama Swinging motion of active deformable particles in Poiseuille flow, *Phys. Rev. E* **96**, 022602 (2017).
- [116] L.L. Bonilla Active Ornstein-Uhlenbeck particles, *Phys. Rev. E* **100**, 022601 (2019).
- [117] P. Romanczuk, M. Bär, W. Ebeling et al., Active Brownian particles, *Eur. Phys. J. Spec. Top.* **202**, 1–162 (2012).
- [118] C.M. Bender & S.A. Orszag, *Advanced Mathematical Methods for Scientists and Engineers I: Asymptotic Methods and Perturbation Theory*, Springer
- [119] V.I. Arnold, *Catastrophe Theory*, Springer-Verlag. **1**.
- [120] M. Berry & J. Nye, Fine structure in caustic junctions, *Nature* **267**, 34–36 (1977).
- [121] M. Berry Focusing and twinkling: critical exponents from catastrophes in non-Gaussian random short waves, *Journal of Physics A: Mathematical and General* **10**, 2061–2081 (1977).
- [122] J. Eggers & M.A. Fontelos, *Singularities: Formation, Structure, and Propagation*, Cambridge Texts in Applied Mathematics

- [123] J. Toner, Y. Tu & S. Ramaswamy, Hydrodynamics and phases of flocks, *Annals of Physics* **318**, 170–244 (2005).
- [124] Guido Boffetta & Robert E. Ecke, Two-Dimensional Turbulence, *Annu. Rev. Fluid Mech.* **44**, 427–451 (2012).
- [125] Jason R. Picardo et al. Preferential Sampling of Elastic Chains in Turbulent Flows, *Phys. Rev. Lett.* **121**, 244501 (2018).
- [126] J.K. Eaton & J.R. Fessler, Preferential concentration of particles by turbulence, *Int. J. Multiphase Flow* **20**, 169–209 (1994).
- [127] M. Bukowicki & M.L. Ekiel-Jeżewska, Sedimenting pairs of elastic microfilaments, *Soft Matter* **15**, 9405–9417 (2019).
- [128] M. Fruchart et al., Phase transitions in non-reciprocal matter, [arXiv:2003.13176](https://arxiv.org/abs/2003.13176) [cond-mat.soft]
- [129] W.H. Mitchell & S.E. Spagnolie, Sedimentation of spheroidal bodies near walls in viscous fluids: glancing, reversing, tumbling and sliding, *J. Fluid Mech.* **772**, 600–629 (2015).
- [130] C.J. Hernandez & T.G. Mason, Colloidal Alphabet Soup: Monodisperse Dispersions of Shape-Designed LithoParticles, *J. Phys. Chem. C* **111** (**12**), 4477–4480 (2007).
- [131] D. Saintillan & M.J. Shelley, Theory of Active Suspensions, *Complex Fluids in Biological Systems: Experiment, Theory, and Computation*, Springer New York (2015).